I would like to thank the Professor David Diaz Reigosa,
for the supervision and the guide of this work;
the Assistant Professor Cristian Blanco Charro and Daniel Fernández,
for the help, the availability and the tips given.

A special thank goes to my family, my wise parents and my fantastic siblings,
who accepted and lived my distance during these last years, I miss you always;
to my friends, in Italy and the many met during the unforgettable Erasmus experience,
for the great moments passed together, and always interested on the progress of this work;
and to Maxine for the encouragement and continuous support,
for your wonderful presence in my life.

UNIVERSITY OF PADOVA

INDUSTRIAL ENGINEERING DEPARTMENT
DEGREE IN ENGINEERING OF ELECTRIC ENERGY
MASTER THESIS

Position and speed estimation of an IPM machine by using Hall-effect sensors

Supervisior: Prof. DAVID DIAZ REIGOSA
Co-Supervisior: Prof. NICOLA BIANCHI

Student: ANDREA BENETTON

ACCADEMIC YEAR 2017/2018

Index

Abstract

Modern society is characterized by an increasingly intensive search for maximum performance in every field; the fact that goods and services are delivered in the shortest time and in the best quality possible, trying at the same time to achieve the maximum possible reduction of costs, is a fundamental requirement to be considered competitive in global markets. Nor should it be overlooked that these goods and services should be produced and delivered in a manner to be the most possible compatible with the environment; this issue, becoming increasingly topical, is pushing the authorities to issue about increasingly stringent standards.

In the last few decades there has been a drastic change of course in the global energetic context. It has been noted that the planet is running out of energy resources because of its indiscriminate exploitation and population growth. In addition the massive use of fossil fuel has resulted in a rate of pollution that has reached alarming level. Among the many energy policies that have been proposed and enacted to reverse this negative trend, certainly energy efficiency is one of the most promising. One of these policies is the "Kyoto Protocol", adopted In December 1997 in the United Nations Framework Convention on Climate Change, which was held in Kyoto, Japan. In February 2005, the protocol was enforced, and the world started to focus on greenhouse gas emission reduction, and an effective method to cut greenhouse gas is to cut power consumption.

Given the general context, even in the field of industrial electrical drives and transport is occurring a general tendency to the continuous improvement of the services offered, reducing the power consumption and, maintaining, if not improving, the quality. On the other hand, one can observe a constant effort in the search for solutions which can also improve the efficiency and the reliability. Whit this in mind, there has been an incredible increase in the use of the electric motors that are definitely more efficient than the internal combustion engine.

Among the electric motors, this commercial and environmental push has bring a wide dissemination of the Synchronous Permanent Magnet machine whose characteristics allow to have many advantages making it preferable to other types of motors. These conveniences include high performances, limited losses and high efficiency since their excitation is provided by the permanent magnets. The increase in the utilization of these motor has been also powered by the advancement of permanent magnets discovering new material with higher coercitivity, demagnetization resistance and magnetic force (ferrite magnets and rare earth magnet), the advent of electronic power components with increasingly better performance and reliability (IGBT) and the development of variable-speed controllers (like inverters and frequency converter).

However, it must be not forgot that price is a determining factor at the time of purchase, and an high price can represent a sale limit.

In this work it is meant to face the characterization and the study of an electric drive with brushless Interior Permanent Magnet (IPM) motor employing analog Hall-effect sensors. It will be analysed a speed and position detection scheme by using Hall-effect sensor that will be digital in the case of simulations and analog in practice. In this last case, the signal from the Hall-effect sensors will be digitalized and so used as input signal in a Code Composed Studio code in turn implemented in a DSP. In both cases it will be adopted a Multi-Complex Coefficient-Filter Synchronous-Reference-Frame Phase-Looked Loop to extract the speed and position from the data coming to the Hall-effect sensors. The results from the simulations and experimentations will be compared and analysed.

It has been chosen to do these estimations using Hall-effect sensors because of their really low price compared to the most used encoder, for example a typical encoder costs around 300 €, contrariwise the cost of these sensors is a matter of cents. Their utilization give the possibility to decrease the price of the entire control of a permanent magnet motor at the expense of a less accuracy in the whole speed range compared with the more précised method using the encoder.

Introduction

Energetic issues and technological development have brought the electronically assisted generation motion systems to be increasingly used in industrial as in civil applications.

With this in mind it is defines drive a mechanical system capable of producing and controlling the motion of a mechanical organ (load) acting on static (position), kinematics (speed) and dynamics (acceleration, torque) quantities. Each drive comprises a power member, said actuator, capable of producing mechanical work connected to the motion, and implements its function through a force (linear actuator) or, more commonly, through a torque (rotary actuator). This actuator can be hydraulic, pneumatic or electric.

According to the standard IEC 301-1 a Power Drive System (PDS) is defined as system that converts the electrical energy into mechanical, with the use of power electronics equipment. It therefore makes use of an electric actuator, namely an electrical machine, said servomotor if built specifically for the drives as it incorporates a sensor position feedback as in the case of this work.

The motion control is implemented through the motor supply quantities (voltage, current, frequency). In order between the motor and the electrical energy supply source it is interposed a power device able to supply the motor with the desired amplitudes of voltage, current and frequency. Such a device generally is a static converter that consists of a transformer (not always), to adjust the level of voltage and /or the number of stages, and a power electronics structure that employs diodes, thyristors, transistors etc. Another essential element is the microprocessor control device which receives in input the external command (which may be the speed or torque or position) and the measurements made by the sensors, processes and imparts commands to the other organs of the system.

Then the drive may be viewed as a complex set of all these elements interacting between them, with which, once fixed the control strategy, the desired movements of the mechanical load can be achieved automatically, accurately and effectively. An exemplification is on Figure 1.1.

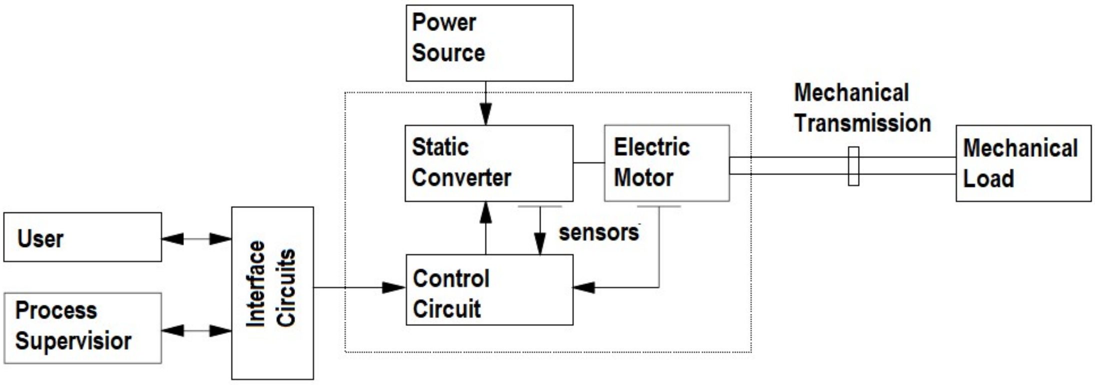

Figure 1 *- Electric drive scheme.*

The power part, or power circuit, of an electric drive is that which has to convert the electrical power coming from the power source in the form suitable to be able to feed in appropriate method the electric motor. This may be considered to be divided into three sections [1], represented on the next Figure 1.2.

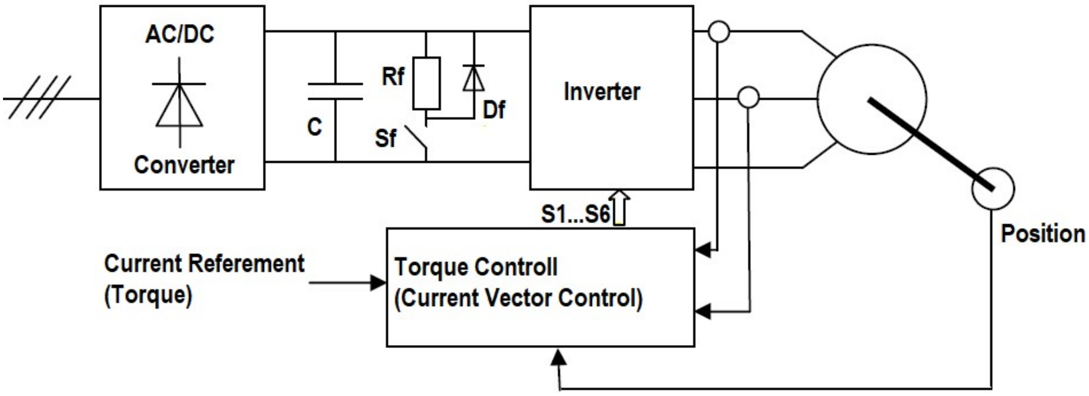

Figure 2 *- Scheme of a brushless drive.*

The first is the power supply section which depends on the power source. Its task is to make the transformation from alternating voltage to constant via an AC/DC uncontrolled converter (diode rectifier) which is not reversible, or via an AC/DC controlled converter. In the latter case, during braking of the motor, the current generated by the same may be supplied to the power source. In the case of not controlled converter, to avoid that on the DC network between rectifier and inverter (DC bus) during braking the voltage across the capacitor, which has the task of leveling the rectified voltage, exceeds high values, is introduced a braking circuit (second section). This last one consist of a braking resistance, Rf, that is connected to the DC bus via a static switch, Sf, whenever the voltage tends to exceed a maximum admissible level. Then the switch is open when the voltage get down a certain level.

Finally, the third section is the power converter that has the task of supplying the motor, and then perform a DC/AC (inverter) or DC/DC conversion and its structure depends on the electric motor itself. The commands sent to the latter come from the control device.

This control is in fact a current vector control, i.e. a space vector control of the stator current in a precise reference at system. For proper and effective control is essential to measure, in addition to the phase currents, also the absolute position of the motor. The necessity of measuring the absolute position of the rotor characterizes drives with brushless motor, like IPM motor. The torque reference often comes from a speed loop that processes the speed error between a reference speed and the speed measured (in our case will be derived from the processing of Hall signals) on the motor or load.

CHAPTER 1

THEORETICAL ASPECTS

1.1 Permanent Magnet Motor Introduction

The Permanent Magnet motors belong to the category of synchronous motors. These kind of motors are fed with an alternating voltage and the rotational speed is rigidly linked to the frequency of the supply voltage. They can be divided into two categories: synchronous motors with excitation winding and synchronous motors with permanent magnets.

The motor subjected to examination on this work is a Interior Permanent Magnet Synchronous Motor, and obviously belongs to the second category. They have the magnets inserted in the rotor structure, instead of the excitation winding. This bring to a more complex construction respect the asynchronous motors with excitation winding, and an higher price, especially for the presence of the magnets. Such motors are also known as brushless because they do not need sliding contacts (brushes-rings) on the motor shaft to furnish current to the rotor. The switching of the current circulating in the windings, in fact, does not take place more by mechanical contacts, but electronically, with the consequence of a lower mechanical resistance, elimination of the risk of spark with the increase of speed, and less maintenance requested [2].

Originally limited in power, they are now able to reach power of several hundreds of kW. They have good efficiency and high power factor, since the magnetic field is, in whole or in part, provided by the permanent magnets. Furthermore, thanks to the performance achieved by modern permanent magnetic materials as SmCo (Samarium Cobalt) or NeFeB (Neodymium Iron Boron), they have a high ratio torque/volume and power/weight [1].

They also have the possibility to be designed in the most varied forms: with a high length/diameter ratio if required high speed and low inertia (machine tools), or with a low ratio length/diameter if required low speed and high torque (traction applications). They dissipate much less heat than an equivalent AC motor as, the losses by Joule effect, are due only to the stator windings and the absence of brush lend themselves to work in explosive or polluted environments.

Other advantages are the rapidity with which it is possible to reverse the direction of travel and the extremely short time of reaction achieving high performance dynamics, a high overload capacity and maximum speed.

On the other hand they have hardware and controls that can be more complex respect other type of motor since they require the measurement, more or less precise (depending on the applications) of the position of the rotor. This accurate positioning bring the additional cost of the transducer, in addition to the one of the magnets.

This Permanent Magnet motors can be distinguished into two types: DC-brushless and AC-brushless. The substantial difference lies in the fact that in the first type the induced Electro Motive Force (EMF) and the magnetic field in the air gap have a trapezoidal trend, typical of DC machines, while in the second have a sinusoidal trend, as in alternating machines.

Constructively, they differ by the fact that while DC-brushless are characterized by having concentrated windings, necessary to produce a trapezoidal field, the AC-brushless have a sinusoidally distributed winding, in more layers and shortened pitch (to reduce the effects of harmonics), which is essential to produce a sinusoidal field.

The DC-brushless is constructively easier then the AC one and even if they do not need absolute position sensors they offer a not constant torque, that also decrease with the increase of the speed, and a lower efficiency. The AC-brushless machine, instead, has the advantages of having a constant torque independent from the rotor position e and the possibility of forcing the field weakening regime, while the disadvantages are a specific torque slightly smaller, torque ripple at low speed, and greater complexity of the converter, sensor, and control.

This work will take into consideration the control of AC-brushless Permanent Magnet Synchronous Machine (PMSM), in the variant Interior Permanent Magnet (IPM), described in the next chapter. Since they require an absolute position sensor like an encoder or resolver, in this thesis work will be studied and analysed a different solution to avoid the utilization of this expensive mechanism replacing them with Hall-effect sensors.

1.2 Structure and Working Principles

With regard to the physics of the Permanent Magnet machine [3], it is composed of a stator and a rotor both in the shape of a cylindrical crown of laminated ferromagnetic material and separated by an air gap as represented in Figure 1.1.

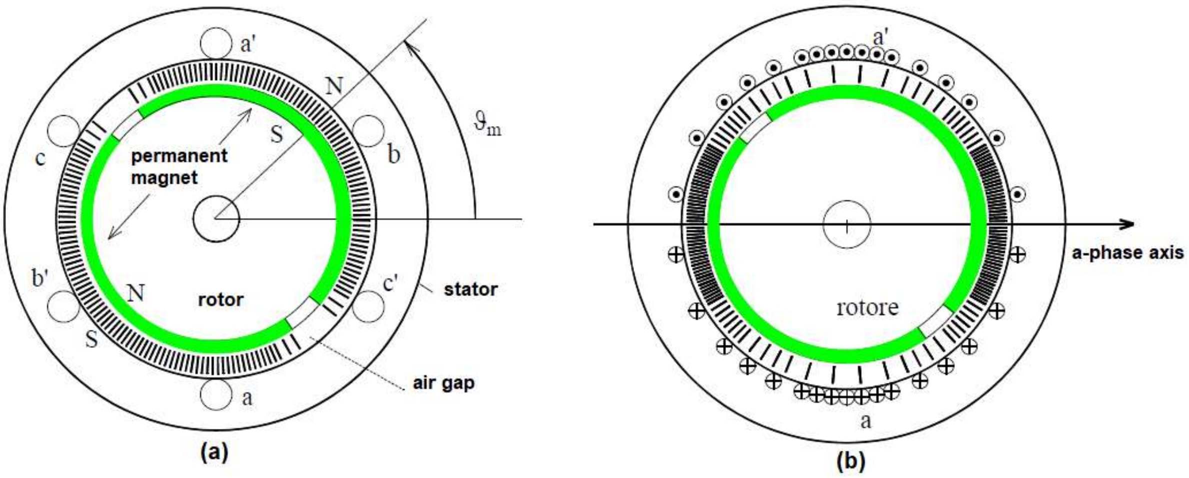

Figure 1.1 *- Schematic representation of a SPM two pole motor: (a) magnetic induction in the air gap created by the magnets; (b) magnetic induction in the air gap produced by the a-phase winding.*

On the stator is located a polyphase winding, usually three-phase with the three phases, $a' - bb' - cc'$, mutually staggered in the space of $2\pi\ /\ 3$ and each is headed by a pair of terminals through which it is possible to provide power to the machine from an external source, like on asynchronous motors. The conductors that form each phase are distributed along the stator slots formed along in the direction of the generatrices of the cylinder stator. Permanent magnets are placed on the rotor. Given their differential magnetic permeability very similar to that of the air, based on where they are positioned and the shape of the rotor may be obtained isotropic or anisotropic rotor structures, by magnetic point of view. This motors are therefore differentiated into three principal categories represented in Figure 1.2: Surface Permanent Magnet (SPM) motors and superficially Inserted (inset) magnets motors that have both two isotropic structures, and Interior Permanent Magnet (IPM) motors that have anisotropic structure [4]. Finally, there are also versions of reluctance motors with small supporting magnets.

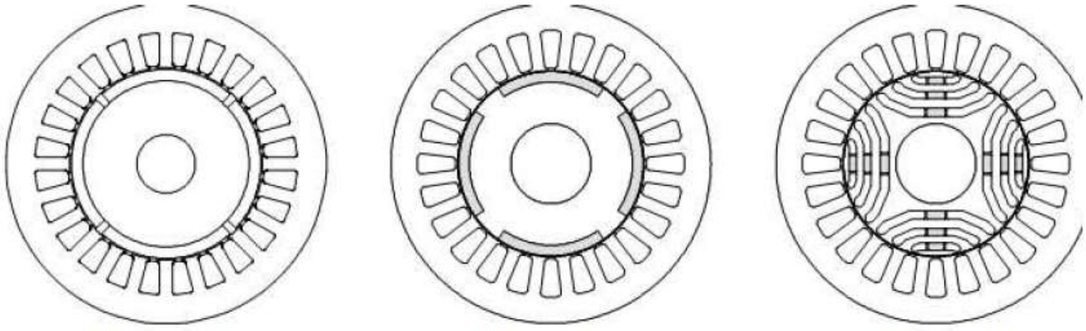

(a) Surface PM (b) inset PM (c) Interior PM

Figure 1.22 *- Different configuration of permanent magnet motors.*

In the SPM motors magnets are mounted on the surface of the rotor with alternating polarity. In the IPM motor magnets are inserted internally to the lamination rotor, presenting so, unlike the SPM, different reluctance paths. With the direct axis placed in correspondence of the polar axis, as in Figure 1.3, the magnetic reluctance for the direct axis flux is greater than that for the in quadrature axis flux.

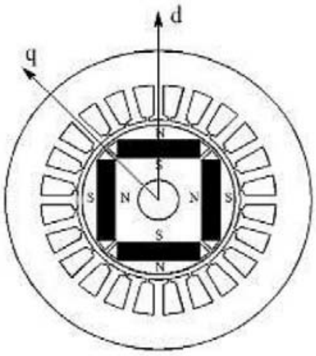

Figure 1.3 *- IPM direct and quadrature axes.*

Are thus obtained $L_d < L_q$. As a result of anisotropy rotor, the electromechanical conversion implemented by the motor does not follow more the only principle of electrodynamic systems but also that of the reluctance systems, using simultaneously both the torque due to the permanent magnet and the reluctance torque, presenting a favorable torque/volume ratio. Also, thanks to this anisotropic structure, it lends itself well to the weakening techniques, achieving high operating speed, that make it particularly suited to applications where mechanical properties at constant power are required.

Compared to isotropic structure, in IPM motors there is a $20 - 30\%$ greater inertia and a greater inductance, and they offer a slight advantage in cost due to use of standard magnetic bars, automatically assembly and the elimination of the bandage. Two representations of the possible structures of an anisotropic rotor motor, tangential and radial magnetization, are shown in the figure below.

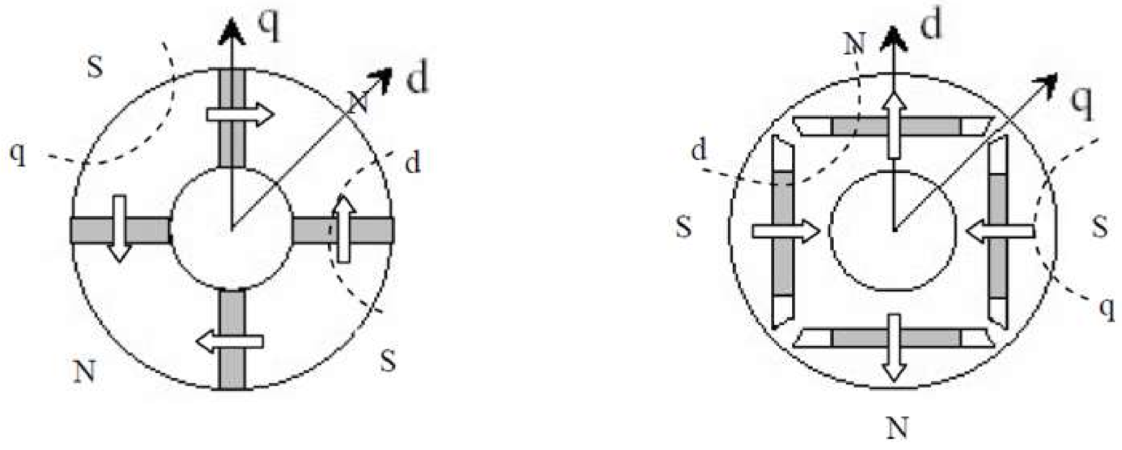

(a) (b)

Figure 1.4 *- Interior Permanent Magnet motor configurations.*

In the first case, Figure 1.4*a* the magnets are arranged radially in the rotor, the magnetization assumes a transverse trend and the flow is conveyed to the air gap through the soft ferromagnetic material sectors. In this way it is possible to build machines with a high number of poles and to obtain a concentration of flow to the air gap with higher induction values of those available in the individual magnets because the flux of each pole is given by the flux of the sum of two magnets obtaining a densification of the air gap field lines and high magnetic induction. This solution is adopted when are used magnets with low residual induction and with machine with high number of poles. Furthermore, the shaft must be non-magnetic to prevent flux recirculation.

In the second case, Figure 1.4*b*, being the area of the magnet smallest of the area of the pole, is obtained a lower induction in air gap than in the magnet, in addition, this configuration has a high permeance of q-axis and low permeance of d-axis, that is, a high rotor's anisotropy. Note that in both configurations are present magnetic bridges, indispensable to keep the compact structure, which, however, should be reduced to the minimum value allowed by mechanical considerations as they constitute possible magnetic paths, furthermore they must have a thickness such as to be able to contain the permanent magnet during the rotation, so that to avoid this splashing at the outside of the machine itself. Sometimes there are also air channels at the ends of the magnets, where the combination of the magnets more the air channel is defined as flux barrier.

In recent years, advancement of the computation ability and control technology of microcomputers push the development of the IPM motor, which thanks to the embedded permanent magnets has also a reluctance torque besides magnetic torque. This type of motor is highly efficient and provides variable-speed operation for a wide range.

As it has been described, the rotor structure of an IPM motor can be flexible, and various characteristics can be exhibited by adjusting the control method. IPM motors can be used for various applications where high-speed and high-efficiency operation is required in a wide range such as a compressor motor for an air conditioner, and where robust low-speed ripples are required at low-speed operation such as the main shaft of a machine tool.

These motors are used more and more both in the industrial field, especially in small and middle power servomotor, and in civil field (household appliances, medical equipment) either in the field of light traction. They are principally used in high-performance drives, in which the particular specifications justify the cost, higher than the classic Induction Motor.

In the future, IPM motors will be employed in a wider range of diversified applications due to improvements in materials such as permanent magnets and electromagnetic steel sheets, advancement of work technology such as stamping technology, development of new power elements, and advancement of variable-speed controllers with improved control technology.

1.3 Electrical Stator Equations

It is now briefly described the electrical equations of the permanent magnet motor isotropic and on the next §1.5 it is considered the anisotropic motor since the latter will be used in this study.

The description of the operation of the sinusoidal brushless motor can start from the general balance equations of the voltages u_a , u_b , u_c, of the phases a, b, c, that with the sign convention of the users are:

$$u_a(t) = Ri_a(t) + \frac{d\lambda_a(t)}{dt} \tag{1.1}$$

$$u_b(t) = Ri_b(t) + \frac{d\lambda_b(t)}{dt} \tag{1.2}$$

$$u_c(t) = Ri_c(t) + \frac{d\lambda_c(t)}{dt} \tag{1.3}$$

where i_a, i_b, i_c are the current that flow on the phases, λ_a, λ_b, λ_c , are the magnetic flux concatenated with each phase, while R is the phase resistance, which is assumed equal for the three phases [3]. In the case of absence of saturation of the magnetic circuits, the flux concatenated by each phase is the sum of the flux concatenated produced by the permanent magnet and the one due to the phase currents.

It is now supposed to do not send current in the stator winding. The combination of a suitable shaping of the magnet and of the distribution of the conductors of each phase allow to obtain nearly sinusoidal concatenated fluxes due to the permanent magnet. Choosing arbitrarily as reference coordinate the electrical angle θ_{me} between the axis of the phase and that of the field produced by the permanent magnet, also defined mechanical-electric position, one can write:

$$\lambda_{a,mg} = \Lambda_{mg} * \cos(\theta_{\mathrm{me}}) \tag{1.4}$$

$$\lambda_{b,mg} = \Lambda_{mg} * \cos\left(\theta_{\mathrm{me}} - \frac{2\pi}{3}\right) \tag{1.5}$$

$$\lambda_{b,mg} = \Lambda_{mg} * \cos\left(\theta_{\mathrm{me}} - \frac{4\pi}{3}\right) \tag{1.6}$$

where Λ_{mg} represents the maximum flux concatenated with each phase for effect of the permanent magnet. The electrical angle θ_{me} is related to the mechanical position θ_m by the relation $\theta_{me} = p * \theta_m$, with p represents the number of pole pairs of the motor. To this set of three variables one can associate uniquely a spatial vector:

$$\bar{\lambda}^s{}_{mg} = \Lambda_{mg} e^{j\theta_{me}} \tag{1.7}$$

where the superscript s indicates that it refers to a stationary reference system, that is integral with the stator. A representation of the spatial vector of the magnet flux is on Figure 1.5.

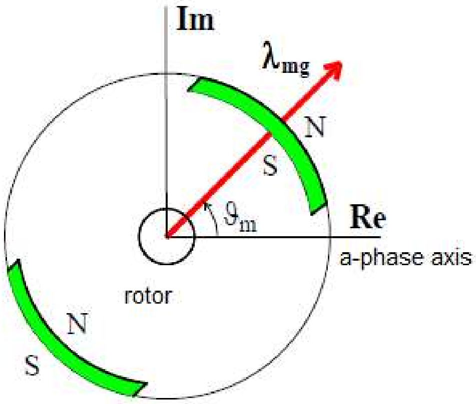

Figure 1.5 *- Spatial vector of the magnet flux.*

It is then analyzed the concatenated flux produced in the windings by the phase currents. With the assumption of isotropy of the structure and symmetry of the phase windings, can be said that the phase self-inductance are all equal to each other, as well as the mutual inductances between each of the windings and the other two, that is will not be true for anisotropic machine. In particular, it is easy to realize that the mutually coupled flux have opposite sign to those who are self-concatenate in each winding. One can then write:

$$L_a = L_b = L_c = L_{ss} \tag{1.8}$$

$$M_{ab} = M_{ac} = M_{bc} = -M_{ss} \tag{1.9}$$

The total concatenated flux are then expressed as:

$$\lambda_a = L_a\, i_a + M_{ab}\, i_b + M_{ac}\, i_c + \lambda_{a,mg} = L_{ss}\, i_a + M_{ss}(i_b + i_c) + \lambda_{a,mg} \tag{1.10}$$

$$\lambda_b = L_b\, i_b + M_{ab}\, i_a + M_{bc}\, i_c + \lambda_{b,mg} = L_{ss}\, i_b + M_{ss}(i_a + i_c) + \lambda_{b,mg} \tag{1.11}$$

$$\lambda_a = L_c\, i_c + M_{cb}\, i_b + M_{ac}\, i_a + \lambda_{c,mg} = L_{ss}\, i_c + M_{ss}(i_b + i_a) + \lambda_{c,mg} \tag{1.12}$$

Generally synchronous permanent magnet motors have stator windings without neutral wire; then the sum of the currents at any instant is:

$$i_a + i_b + i_c = 0 \tag{1.13}$$

Obtaining at the end:

$$\lambda_a = Li_a + \Lambda_{mg} \cos(\theta_{me}) \tag{1.14}$$

$$\lambda_b = Li_b + \Lambda_{mg} \cos(\theta_{me} - 2\pi/3) \tag{1.15}$$

$$\lambda_a = Li_a + \Lambda_{mg} \cos(\theta_{me} - 4\pi/3) \tag{1.16}$$

Where is defined the synchronous inductance $L = L_{ss} + M_{ss}$.

The balance equations of the voltages can be generalized as:

$$u_a(t) = Ri_a(t) + L\frac{di_a(t)}{dt} + e_a) \tag{1.17}$$

$$u_b(t) = Ri_b(t) + L\frac{di_b(t)}{dt} + e_b) \tag{1.18}$$

$$u_c(t) = Ri_c(t) + L\frac{di_c(t)}{dt} + e_c) \tag{1.19}$$

where are defined the electromotive force e_a, e_b, e_c due to movement of the permanent magnet respect to the stator windings:

$$e_a(t) = \frac{d\lambda_{a,mg}(t)}{dt} = -\Lambda_{mg}\omega_{me} \sin(\theta_{me}) = \Lambda_{mg}\omega_{me} \cos\left(\theta_{me} + \frac{\pi}{2}\right) \tag{1.20}$$

$$e_b(t) = \frac{d\lambda_{b,mg}(t)}{dt} = \Lambda_{mg}\omega_{me} \cos(\theta_{me} + \pi/2 - 2\pi/3) \tag{1.21}$$

$$e_c(t) = \frac{d\lambda_{c,mg}(t)}{dt} = \Lambda_{mg}\omega_{me}\cos(\theta_{me} + \pi/2 - 4\pi/3) \tag{1.22}$$

Where the ω_{me} $(rad.el./s)$ is the electromechanical speed. Although the voltages have zero-sum because they are a tern of sine waves shifted between them of $2\pi/3$ electrical radiant. Being all sizes without zero-sequence component is possible to obtain a more compact expression using the notations according spatial vectors. To the electromotive force is associated the spatial vector $\bar{e}$ given by:

$$\bar{e}^s = \frac{d\bar{\lambda}^s_{a,mg}(t)}{dt} = j\omega_{me}\bar{\lambda}^s_{mg}) \tag{1.23}$$

and the balance equations of the voltages are expressed by:

$$\bar{u}^s = R\bar{\imath}^s + L\frac{d\bar{\imath}^s}{dt} + j\omega_{me}\bar{\lambda}^s_{mg} \tag{1.24}$$

That expressed in its real and imaginary components become:

$$u_\alpha = Ri_\alpha + L\frac{di_\alpha}{dt} - \omega_{me}\lambda_{\beta,mg} \tag{1.25}$$

$$u_\beta = Ri_\beta + L\frac{di_\beta}{dt} + \omega_{me}\lambda_{\alpha,mg} \tag{1.26}$$

1.4 Electrical Equations in the Synchronous Reference System

An even more compact expression is obtained by expressing the vectors of (1.24) according to a synchronous reference system with the rotor, that is rotating with the electromechanical speed θ_{me}, with the real axis coinciding with the axis of the rotor flux. The spatial vector turns out to have only real component and this simplifies further the balance equations of the stator voltages. The general spatial vector g^s expressed in the synchronous reference frame (apex r) is:

$$g^r = g^s e^{-j\omega_{me}t} = g^s e^{-j\theta_{me}} \tag{1.27}$$

Therefore, by applying the (1.27) to (1.24), and remembering that $\lambda^r_{mg} = \Lambda_{mg} + j0$, is obtained

$$\bar{u}^r = R\bar{\imath}^r + L\frac{d\bar{\imath}^r}{dt} + j\omega_{me}\bar{\lambda}^r_{mg} \tag{1.28}$$

Which can be written by separating the real and imaginary parts:

$$u_d = Ri_d + L\frac{di_d}{dt} - \omega_{me}Li_q \tag{1.29}$$

$$u_q = Ri_q + L\frac{di_q}{dt} + \omega_{me}Li_q + \omega_{me}\Lambda_{mg} \tag{1.30}$$

From these equations it is possible to perform an energy balance in the synchronous reference system, to derive an expression of the mechanical torque developed by the motor. Multiplying both sides respectively for $i_d dt$ and $i_q dt$ and adding member to member the two equations one gets:

$$\left(u_d i_d + u_q i_q\right) dt = (R i_d^2 + R i_q^2) dt + L i_d - L i_q dt + \omega_{me} \Lambda_{mg} i_q dt \tag{1.31}$$

The first member is the electric power supplied to the motor in the time dt. It is matched by the energy resulting after the electro-magnetic conversion process, the components of which are represented by the terms in the second member. The first term is the energy dissipated into heat on the winding resistance; the second and third constitute the energy stored in the magnetic field, connected to the synchronous inductances L; the last term is the developed mechanical energy, because the machine is supposed to operate as motor. The transformation adopted for the transition from the stationary reference system to the synchronous is not invariant for the power, which is decreased by a factor of $2/3$. Recalling that the mechanical power can also be expressed as the product of the torque T for mechanical speed ω_m, it leads at the end:

$$T = \frac{3}{2} p \Lambda_{mg} i_q \tag{1.32}$$

The formula (2.32) confirms that the torque only depends on the q component of the current, that is the component in quadrature with the concatenated flux due to the permanent magnets. That is, also, the component in phase with the electromotive forces. This is the principle followed to defined the currents to send to the stator of a synchronous permanent-magnet motor with isotropic rotor, inserted in an electric drive. An anisotropic motor have been used for the study of this thesis, and the chapter proceeds now to define the equations for this type of machine.

1.5 Extension to the Anisotropic SPM Motor

As mentioned above, the anisotropic permanent magnet synchronous motors have a rotor structure (or an arrangement of the magnets) such to have a marked magnetic anisotropy. The relationship (1.4 ÷ 1.7) are still valid, but they are not the subsequent considerations of the preceding paragraph. In particular, the self- and mutual-inductances of the stator phases are now rotor position functions. Taking into account this fact the machine equations in the rotating reference system synchronous with the rotor become:

$$u_d = Ri_d + L_d \frac{di_d}{dt} - \omega_{me} L_q i_q \tag{1.33}$$

$$u_q = Ri_q + L_q \frac{di_q}{dt} + \omega_{me} L_d i_d + \omega_{me} \Lambda_{mg} \tag{1.34}$$

where L_d is the direct synchronous inductance, since it is traversed by direct current i_d and L_q is the quadrature synchronous inductance, since it is traversed by quadrature current i_q. The direct current i_d produces a magnetic field whose axis of action is the direct axis or the polar axis as shows Figure 1.6a. The quadrature current i_q produces instead a magnetic field whose axis of action is the axis of quadrature or interpolate axis, as shows Figure 1.6b. The magnetic circuit excited by the latter does not therefore include the permanent magnets, but it develops along the type "q" lines. Hence, the two inductances, albeit constant, are different because different are the reluctance of the magnetic circuits of direct axis and quadrature axis. In particular, $L_d < L_q$.

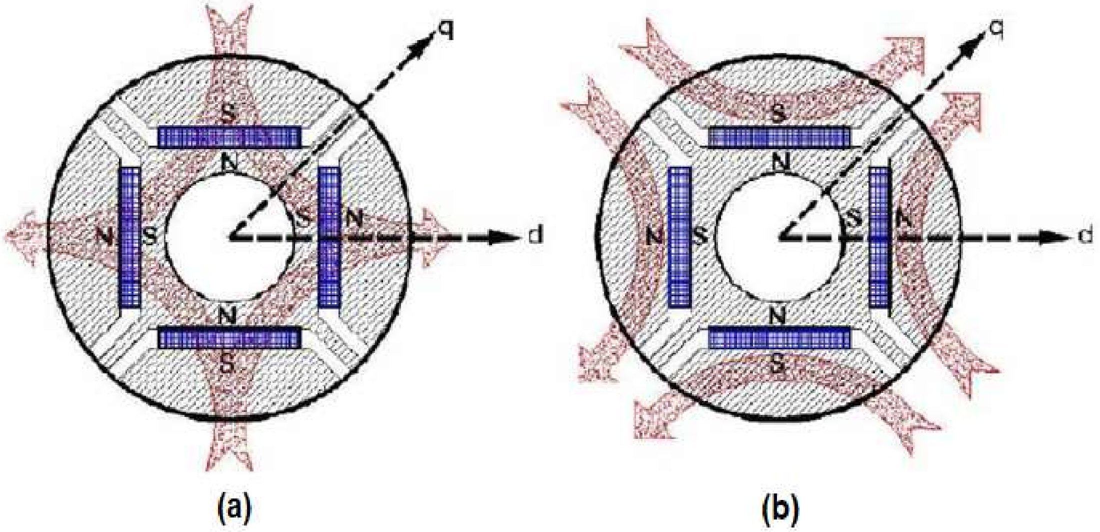

Figure 1.6 *- Magnet flux path in a IPM motor: (a) direct flux, (b) quadrature flux.*

The expressions (1.33) e (1.34) allow to trace the energy balance in the synchronous reference system, to derive an expression for the mechanical torque developed by the motor. Even in this case, one multiplies both sides of the (1.33) and (1.34) respectively for $i_d dt$ and $i_q dt$. By adding member to member the three equations is obtained:

$$\begin{aligned}(u_d i_d + u_q i_q)dt \\ &= (Ri_d^2 + Ri_q^2)dt + L_d i_d dt - L_q i_q dt + \omega_{me}\left[\Lambda_{mg} i_q + (L_d - L_q) i_d i_q\right]dt\end{aligned} \tag{1.35}$$

Considerations entirely similar to those performed in the §1.4 lead to write the following equation for the torque generated by the anisotropic synchronous motor:

$$T = \frac{3}{2} p \Lambda_{mg} i_q + \frac{3}{2} p \left(L_d - L_q \right) i_d i_q \tag{1.36}$$

Compared to the expression (1.32) obtained in the case of isotropic rotor occurs, as mentioned at the beginning, the presence of a further term, said reluctance torque.

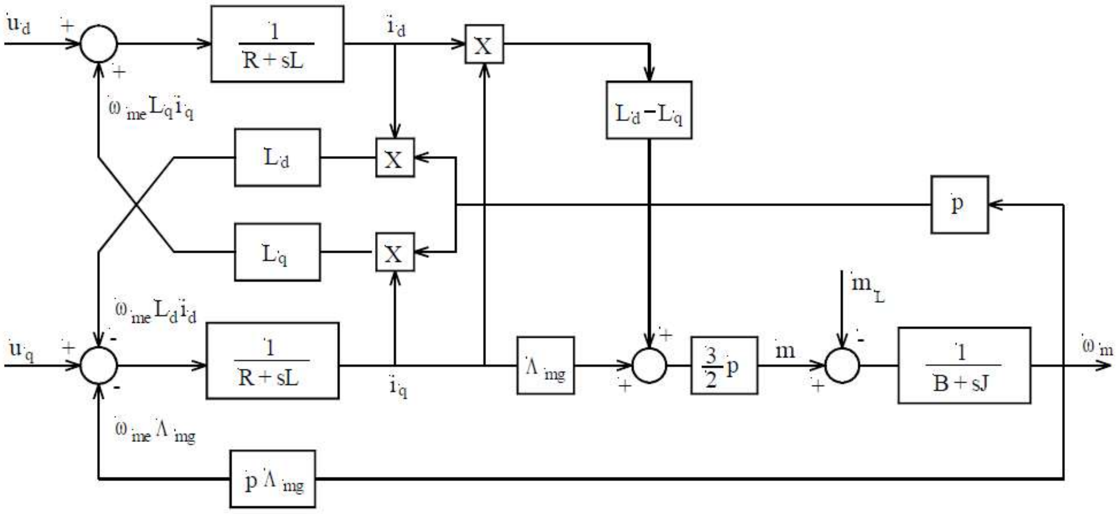

Figure 1.7 *- Block scheme of the IPM motor.*

CHAPTRER 2

ROTOR POSITION DETECTION

2.1 Introduction

For the functioning of a permanent magnet motor is essential the use of a power electronic converter and of a control system. To implement the wanted laws of motion and speed, and then for its proper control, must be provided to the current regulation system the angular position of the stator and rotor magnetic fields. The instantaneous position of the magnetomotive force of the stator is formed by means of current sensors on phases of the motor itself, usually they measure two of them deriving the third by the principle of Kirchoff as being often the stator windings without neutral wire the sum of the three phase currents is zero. The instantaneous angular position of the rotor may instead be formed in various ways.

The schemes to estimate the rotor angle can be classified into two types: one is named sensorless control, and uses the measures on electrical terminals and the dynamic model of the machine; the second is named sensored control, where the angle is acquired by suitable transducers mounted on the shaft of the machine (encoder, resolver, Hall sensors).

The knowledge of the position and speed of the rotor are necessary because the first is needed to realize the PID controllers operating with constant or slowly variable magnitudes (converted into sinusoidal magnitudes by means of transformation matrices operating with the measured angle), and also represents the position of direct axis of the reference system in which are defined the currents to be imposed to the stator to obtain the desired torque. The second one, is necessary to achieve the decoupling of the axes and the speed control.

The current trend is to be able to remove the sensor to replace it with an estimator; the main advantages of this choice are:

- The reduction of costs: an encoder also not overly performance is however expensive, and its removal would render the final product more economic. Also is not possible to reduce excessively the encoder performance as this is discrete, and a change in step by step too large of the angle measured can be a problem. It might be used a resolver (which is analogic), but also this would has its drawbacks.
- The reliability of the system: a sensor is always subject to possible breakage, and in this context a break would imply the drive unusable, with consequent losses (in terms of time and especially of money) for the end user.
- Practicality: to prevent breakage, periodic maintenance is required. Additionally it can sometimes be uncomfortable the application of a sensor of a certain size in a much larger or much smaller system.

On the other hand, the problems that can be obtained with the use of the estimators are firstly that the estimate of a quantity will never be as precise as its measurement via sensor, making everything more complicated in terms of performance and stability: in fact, for applications that require a high degree of accuracy the use of the sensor is essential, and also in general a position control can not be executed as the estimated position will not be mechanical but the electric one. The other not negligible problem is the absence of an excellently functioning estimation algorithm at low and at high speeds, indeed it is necessary to use two different methodologies and switch them in course of work. Moreover sensorless controls have higher requirements for control algorithms and more complicated electronics.

In the following paragraphs is given a brief description of some of the rotor position detection techniques , and is then described the use of Hall-effect sensors and the MCCF functioning.

2.2 Sensorless Techniques

Position sensors can be completely eliminated in those applications in which only variable speed control (i.e., no positioning) is required and system dynamics is not particularly demanding. Various sensorless control methods can be classified into two main groups:

saliency-tracking-based methods and fundamental-model-based method. The saliency-tracking-based methods are normally used at standstill and low speed. Since the spatial distribution of inductance is determined by the rotor position, it can be estimated by injecting signal to the machine and analyzing its response. However, additional signal injection brings about problems such as audible noise, reduced voltage margin of inverter output, vibration of drive system, and losses. For these reasons, in middle or high speed range where, the back electromotive force (back-EMF) is sufficiently large, the fundamental-model-based methods which do not require the signal injection are normally used. In the fundamental model-based methods, the rotor position can be estimated based on the mathematical model of the machine with stator voltages and currents.

2.2.1 Fundamental-Model-based Methods

There are many categories of sensorless control strategies and the most popular is based on back electromotive forces or back-EMF [5], Figure shows a general block diagram for this kind of methods.

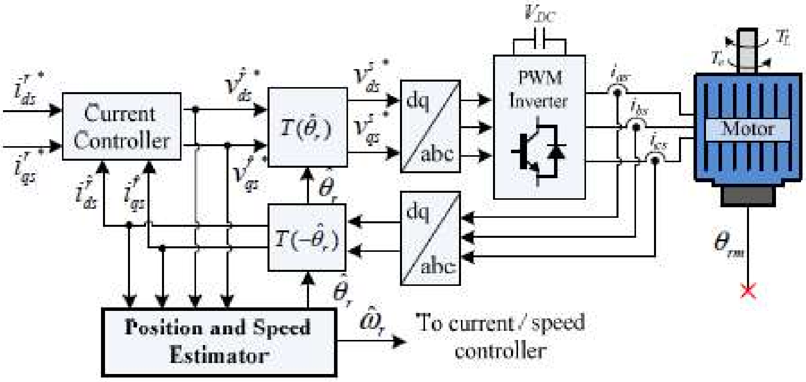

__Figure 2.1__ - Block diagram of a general sensorless drive system.

This type of control uses electromotive force as information that indicates when to switch the phases, since the EMF is present only in some phases at each instant, depending on the position of the rotor, then this EMF can be used to give information on the position of the rotor poles and their magnetic polarity. The angular speed and position of the polar axis of the rotor are obtained from the back-EMF induced in the stator windings, using fundamental model of the machine. To get this information the stator currents and voltages are needed. The stator current can be easily measured, while the stator voltages are not normally measured but can be estimated from the voltage commands to the inverters. The estimator uses a model of the motor that contains the rotor position together with the measured stator current and voltage and solve it getting, at the end, the rotor position as a function of measured quantities. Figure 2.2 shows the classical procedure for rotor position and speed estimation.

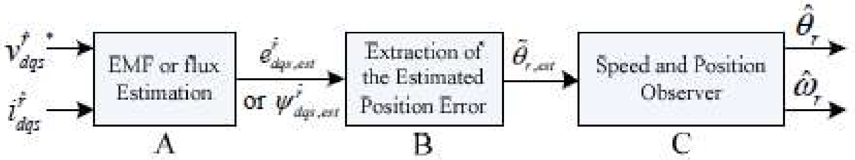

Figure 2.2 *– Position and speed estimation procedure.*

Part *A* estimates the EMF or flux linkage based on the fundamental models. This part can be implemented by either closed-loop estimators or direct calculation methods [6]. And the estimation in Part *A* can be done on the stationary reference frame or on the estimated rotor reference frame. Part *B* calculates estimated position error denoted as $\tilde{\theta}_{r,est}$ which is the estimated value of actual position error denoted as $\tilde{\theta}_r$. $\tilde{\theta}_{r,est}$ can be calculated from the estimated EMF or flux linkage by simple arithmetic operations or trigonometric functions. For last, part *C* estimates rotor position and speed from $\tilde{\theta}_{r,est}$. Part *C* can be implemented by PI (Proportional Integral) type observer or PID (Proportional Integral Derivative) type observer. Part *C* is not specialized for a specific algorithm but can be used in general.

Conventional and recent advancement of back-EMF sensing methods for the PM motors and generators are split in two categories, direct and indirect back-EMF detection [5]:

- Direct back-EMF detection methods: the back-EMF of floating phase is sensed and its zero crossing is detected by comparing it with neutral point voltage. This scheme suffers from high common mode voltage and high frequency noise due to the PWM drive that superimpose his signal on the neutral voltage, so it requires low pass filters, and voltage dividers. The methods can be classified as: back-EMF Zero Crossing Detection (ZCD) or Terminal Voltage Sensing; PWM strategies.
- Indirect back-EMF detection methods: because filtering introduces commutation delay at high speeds and attenuation causes reduction in signal sensitivity at low speeds, the speed range is narrowed in direct back-EMF detection methods. In order to reduce switching noise, the indirect back-EMF detection methods were introduced. However, these methods still have an accuracy problem at low speed These methods are the

following: back-EMF Integration; Third Harmonic Voltage Integration; Free-Wheeling Diode Conduction in unexcited phase or Terminal Current Sensing.

The back-EMF zero-crossing detection (terminal voltage sensing) method, which does not require the motor neutral voltage, permits the extraction of the true back-EMF directly from terminal voltage by properly choosing the PWM and sensing strategy. As a result, this sensorless driver can provide a much wider speed range from start-up to full speed than the conventional direct detection approaches, even if at low speeds, the detection of the phase voltage become difficult for this method due to the lower signal levels.

The third harmonic based method is one of most relevant back-EMF sensing schemes. It has a wider speed range and smaller phase delay than the terminal voltage sensing method. However, at low speed, the integration process can cause a serious position error, as noise and offset error from sensing can be accumulated for a relatively long period of time.

In comparison, the conventional back-EMF control scheme is able to drive the motor from $6000\ rpm$ to about $1000\ rpm$, but the third harmonic control scheme is capable to operate the motor from rated speed $(6000\ rpm)$ down to about $100\ rpm$ [5]. This does not introduce as much phase delay as the zero-crossing method and requires less filtering. Then, the efficiency drop is more accentuated for the terminal voltage sensing scheme, because the delay introduced by the low pass filter decreases with the motor speed. This phase delay introduced by the filter is responsible for the loss of field orientation and loss of the quadrature condition between rotor flux and stator current. The immediate consequence is the reduction of the torque per current ratio of the motor, which implies in larger copper losses. Furthermore, the third harmonic back-EMF method is applicable for the operation in flux weakening mode, while the methods based on zero-crossing of the back-EMF are only applicable under normal operating conditions. Since back-EMF is zero at standstill and proportional to speed, the measured terminal voltage that has large signal-to-noise ratio cannot detect zero crossing at low speeds. That is the reason why in all back-EMF-based sensorless methods the low-speed performance is limited, and an open-loop starting strategy is required.

However, other control schemes such as the PWM method eliminating the virtual neutral point can provide a much wider speed range from start-up to full speed than the conventional schemes. Besides, this method has high sensitivity; it is good at high-speed operation due to a lack of unwanted delays in the zero-crossing detection. It can be easily used in both high-voltage or low-voltage systems, and it has a faster motor start-up because of the precise back-EMF zero-crossing detection without attenuation. Moreover, it is simple and easy to implement. There are also other scheme for sensorless control that do not depend on the back-EMF, but are more complex.

2.2.2 High-Frequency Injection Techniques

Such estimation algorithms are saliency-tracking-based methods and are employed for the detection of the absolute position of the rotor at low speeds of rotation. This strategy is based on the recognition of the anisotropy of the rotor by injecting the appropriate high-frequency voltages in the stator windings, is thus only suitable for IPM motors since it is necessary that the difference between direct inductances L_d and quadrature inductance L_q (said differential inductance) is different from zero. A principle diagram is shown in Figure 2.3 .As can be seen in the output of the PI are present some summing nodes for the injection of the sinusoidal voltages, with amplitude U_{hi} suitably calculated and frequency $\omega_h$chosen so as to be $\omega_h <$ PWM (at least approximately a decade lower) and $\omega_h > \omega_{me}$ (about a top decade). However, since $\omega_{me} \approx 0$ the second condition can be neglected. The estimated position is marked with $\tilde{\theta}_{me}$ while the estimated speed with $\tilde{\omega}_{me}$.

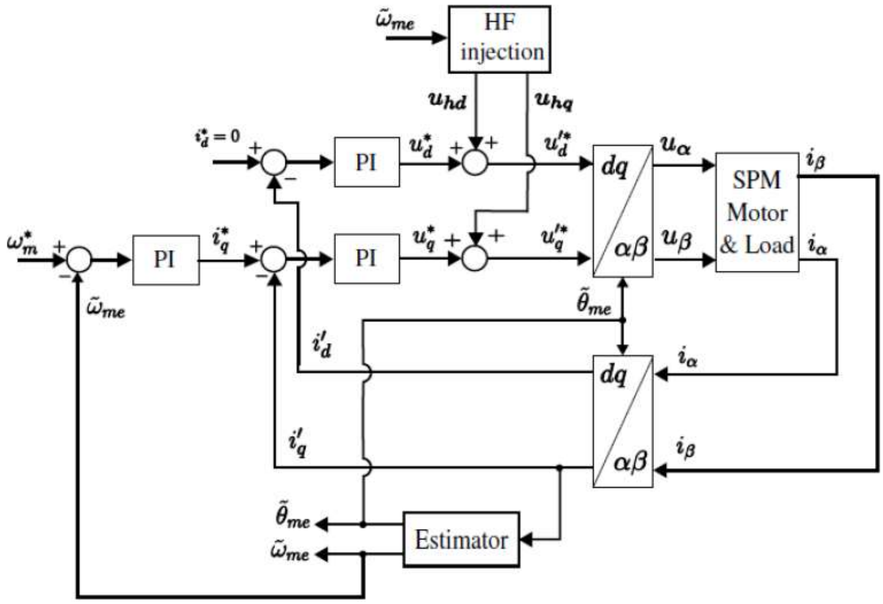

Figure 2.4 *- Block diagram of an HF injection sensorless drive.*

Such methods have the capability of proving accurate, high bandwidth, position, speed, disturbance torque estimates, and/or flux estimates in the low-speed range, including zero speed and frequency. These techniques measure the response of the machine when high frequency excitation, distinct from the fundamental excitation used for the torque production, is applied via the inverter, and it measures the response of particular states of the inverter to track the rotor position. Like pros [7] it has the reduction of the parameter sensitivity, and the fact that they can work at very low and zero speed. On the other hand, to efficiently implement these method, the design of the machine have to be very precise and sometimes additional sensors are requires and for this reason the cost of the drive could increase. Furthermore the injection of high frequency signals or modification of the PWM pattern can results in unwanted effects such as vibration, noise and additional losses. At high speed the additional voltage needed for signal injection becomes a restriction and the correlated high-frequency currents generate unnecessary losses in the motor.

The main high-frequency injection sensorless control methods can be divided depending on the type of high-frequency signal excitation and the signals which are measured. In particular, considering the type of excitation, it can be continuous, discontinuous, periodic and PWM. If continuous excitation is used, a high-frequency signal is always present and superimposed to the fundamental excitation. On the contrary a discontinuous excitation injects the high-frequency signal periodically and so the result is that it does not provide a continuous rotor position estimation. On the other hand, the excitation is considered periodic when it injects a periodic high-frequency carrier signal superimposed on the fundamental excitation while a PWM excitation uses modified forms of PWM.

The HFIST is effective for position and speed estimation in ultra-low speed region including zero stator frequency. However, due to torque ripple and acoustic noise, the method has shortcoming in the practical use in industrial application. On the contrary, the back-EMF based method is able to estimate position and speed without acoustic noise due to additional torque ripple, but the decreasing signal-to-noise ratio and the increasing effect of the parameter-estimation errors and inverter nonlinearities in the model at low speed impede its use in the whole speed range. To perform a smooth transition between both strategies, a hybrid system is needed.

2.2.3 Model Reference Adaptive System

As regards high speeds is possible to estimate the rotor angle, θ_{me}, exploiting the equations describing the electric motor. This solution can be developed in various configurations in "open-chain" mentioned in the previous paragraphs, which use a model of the electric motor that contains the rotor position and therefore is obtainable starting from the quantities that are measured. Another solution very used instead in estimating at high revolution is called "closed loop", where is used a feedback of a certain dimension in order to improve the dynamic of the whole system.

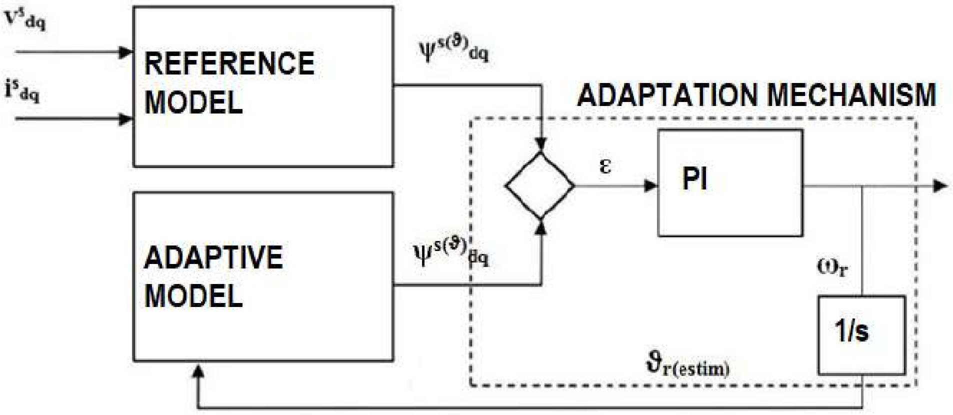

Figure 2.4 *- Block diagram for an MRAS estimator.*

More precisely is the technique MRAS (Model Reference Adaptive System) which allows to estimate the rotor position by comparing, through an appropriate adjustment mechanism, a variable x of the motor, starting from the measured variables to the electrical terminals, obtained by means of two different models [8]. The first model named reference model returns the variable x independent of the rotor position, the second model called adaptive model still provides the value of x, but dependent on the position θ_{me}. The difference between the output of the two models indicate that the rotor position is not correct. Only when the results obtained with the two models are equal, the estimated position coincides with the real one. The reference model and the adaptive model can be implemented starting from the spatial vector of the total concatenated flux or from the permanent magnet flux, or again from the electromotive force vector. The target of the MRAS is to produce an estimated position $\theta_{r(estim)}$ that run after the θ_r which is given by the flux of the permanent magnet obtained with the reference model. The phase lag between the space vector of the flux obtained ψ_{pm}^{s} with the reference model and the one $\psi_{pm}^{s(\theta)}$ obtained with the adaptive model is used as estimation error ε. Also this method uses the fundamental equations of the machine, and obtain the rotor position from the back-EMF induced by the variation of the flux produced by the permanent magnet. Therefore it can not operate at low and zero speed, since the value of the key variable which is needed for the estimation is proportional to the operative speed and so below a certain minimum speed is not possible to relay on it, due to the parametric sensitivity.

2.3 Sensored System

For permanent magnet AC motors, a constant supply of position information is necessary; thus a position sensor with high resolution, such as a shaft encoder or a resolver, is typically used. For less performance application low-cost Hall-effect sensors are usually used. Also, electromagnetic Variable Reluctance (VR) sensors or accelerometers have been extensively applied to measure motor position and speed. The reality is that angular motion sensors based on magnetic field sensing principles stand out because of their many inherent advantages and sensing benefits. Is given below an overview among the most utilized position sensors.

2.3.1 Encoders - Resolver

Many motor control systems for servo applications operate with closed control loops, where the output signal (i.e. position, torque, speed) is sensed and processed to derive the best possible motor inputs. The precise feedback signal is usually achieved by employing resolvers or encoders.

The encoders belong to the category of the transducers of angular position of the digital type, which are devices in which the angular position is quantized, that is, the angle rotation of the mobile shaft ($0 \div 360$ °) is divided into a discrete number of parts to each of which is made to correspond to a digital signal [9]. They deliver not just two switching events over one revolution like the Hall switches, but can have a much higher angular resolution. There are primarily two types of angular transducers with digital output: the absolute encoder and incremental encoder.

In the absolute encoder the output is represented by a combination of logic levels (0 and 1) as the number of bits which form the output signal. Figure 2.5 shows the schematic of an absolute encoder.

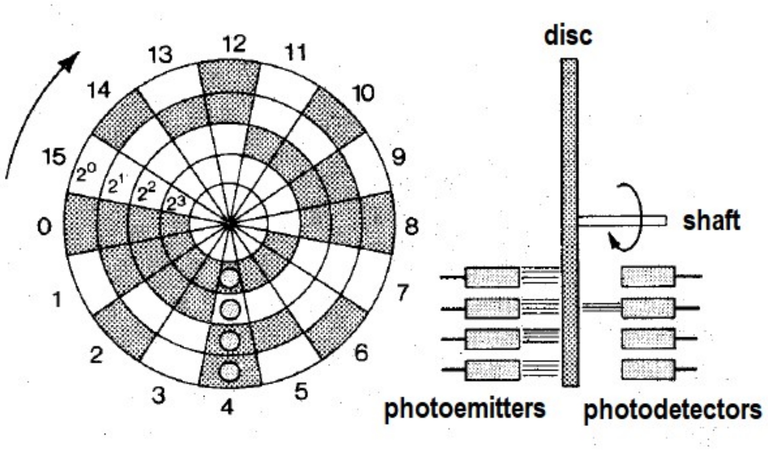

Figure 2.5 *- Absolute encoder.*

It is composed of three main parts: a stationary disc, a rotating code wheel configured in the same way as the stationary disc, and a light source. As the shaft rotates, a photo detector becomes blocked and unblocked from the light source creating an impulse each time the detector is unblocked. These impulses can be used to determine shaft position and speed.

The mobile part of the device consists of a disc which can rotate around an axis keyed on the machine of which is needed to detect the angular position. The disk is divided into a number of sectors equal to 2^n where n is the number of bits of the output signal (in the example of the figure above the output bits are $n = 4$, so the sector are $2^n = 16$). Evidently the greater the number of sectors, the greater the resolution in the angle measurement. The disc is further divided into n circular crowns. In the pattern determined by the intersections of radial lines and concentric circles are appropriately diversified areas (dark and light in Figure 2.5), that allow the angle binary encoding. The reading can be carried out with optical means, in such a case the dark areas are made opaque and the ones clear are made transparent. The fixed part of the reading device consists of n light sources, each of which projects a light beam on the disc, and of a system of n detectors aligned with the light sources and in the opposite position to the disc. At each circular crown it is matched a power of 2, increasing from the outer edge towards the center. Between the terminals of each photodetector is taken the logic level 0 if the device does not receive light and the level 1 if it receives. Therefore, there is a unique correspondence between the sector of the disk, which is interposed between the light sources and the detector system, and the configuration of the output logic levels. The optical reading allows therefore to encode the angular position in pure binary code. In practice, however, the pure binary code is not used in precision encoders since it can lead to read errors, since in passing from one number to the one immediately following it may present simultaneous variations of more bits. The code that is used to avoid this type of error, and on the basis of which then is performed the configuration of the opaque and transparent areas of the disc, is typically the Gray code. The latter is characterized by the fact that in the transition between two consecutive decimal numbers there is always the change of a single bit. It is also possible to realize an electric reading system instead of an optical one. This type of reading can be obtained by realizing the gray portions of the disc with insulating material, the white ones with conductive material. Putting in tension the conductive parts of the disc, a system constituted by as many brushes are the annuli can pick up the voltage along the crowns themselves.

The incremental encoder is a rotary encoder that generates one or two pulse trains, sinusoidal or square, characterized by a number of pulses for each revolution of the shaft (encoder resolution).

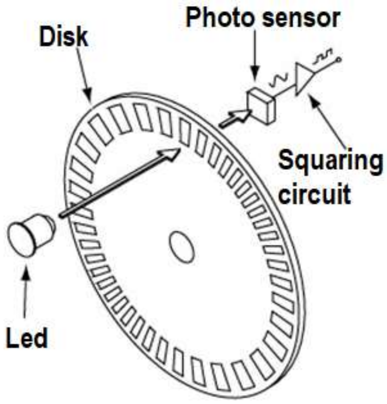

Figure 2.6 *- Incremental encoder.*

In addition it can generate for each revolution an additional pulse, said zero or reference [9]. In particular, for coupling with converters for synchronous servomotors, the sinusoidal encoders provide a further two sine-cosine signals (said switching signals and characterized by a period per revolution) for the absolute detection of the rotor position of the motor upon insertion power. After insertion, the processing involves the incremental signals, treating them with interpolation techniques to achieve resolutions of up to several tens of millions of steps per revolution. At the encoder shaft is firmly fixed a disc of transparent material on which are photoengraves opaque areas. The principle of operation is similar to that of the absolute encoder, but now the opaque areas are alternated with transparent ones without any coding. The surface of the disk is illuminated by photodiodes, so that the opaque areas in motion are able to intercept the luminous traits of the source beam. On the opposite side to the photodiodes are placed phototransistors detection; these transform the modulated light signal into an electric signal with square or sinusoidal waveform. The coupling of the encoder on the shaft takes place by means of an elastic coupling in the axial and radial direction, stiff in the torsional sense.

At last, the resolver is a rotary transducer with two stator windings $(S1 - S2, S3 - S4)$, phase-shifted between them of 0° electrical, and one rotor winding $(R1 - R3)$ as shown in Figure 2.7.

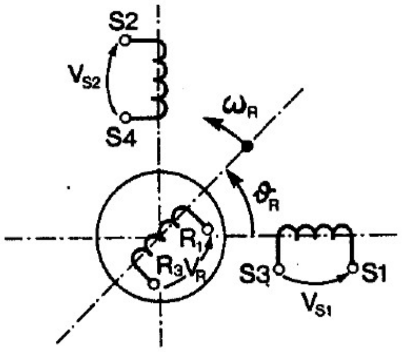

***Figure 2.7** – Resolver scheme.*

By exciting the rotor winding with an alternating voltage, in one stator winding is induced a voltage amplitude proportional to the sine and on the other proportional to the cosine of the angle of rotation of the rotor relative to the stator. The electronic processing of sine and cosine allows to obtain the angle rotor moment by moment, and consequently also the angular speed of the motor. An error in the determination of these two quantities, resulting from the disconnection of one or more wires of the resolver, would result in an error on the commutation of the motor phases: the power converter therefore incorporates a protection circuit that stops the operation immediately in case the disconnection happens.

While the encoder is a proven tested transducer, it has several practical drawbacks, in particular, cost, susceptibility to contamination, size and durability, susceptiblility to mechanical shock and vibration, it needs special arrangement for mounting and could cost until the 30% of the cost of the full drive. The encoder or resolver can increase the cost of the drive by $300\ \$$ to

3000 \$ depending on the application. This cost is further increased by the fact that an added frame is needed to house the encoder/resolver and the installation cost can be 100 \$ to 1000 \$. However, the cost of calibration is small (< 10 \$) since it can usually by accomplished in software.

2.3.2 Variable Reluctance Wheel Speed Sensors

This kind of sensor is used to measure position and speed, and is often referred as a passive magnetic sensor because it does not need to be powered. It consists of a permanent magnet, a ferromagnetic pole piece, a pickup coil, and a rotating toothed wheel.

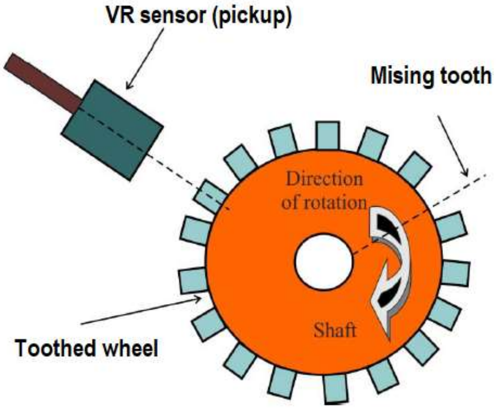

Figure 2.8 *- Variable Reluctance wheel speed sensor.*

It is basically a permanent magnet with wire wrapped around it, as Figure 2.8 illustrates. It is usually a simple circuit of only two wires where in most cases polarity is not important, and the physics behind its operation include magnetic induction [5]. As the teeth pass through the sensor magnetic field, the amount of magnetic flux passing through the permanent magnet varies. When the tooth gear is close to the sensor, the flux is at maximum. When the tooth is further away, the flux drops off. The moving target results in a time-varying flux that induces a voltage in the coil, producing an electrical analogic wave. The frequency and voltage of the analog signal is proportional to velocity of the rotating toothed wheel. Each passing discontinuity in the target causes the Variable Reluctance (VR) sensor to generate a pulse. The cyclical pulse train or a digital waveform created can be interpreted by the brushless motor controller. The advantages of the VR sensor can be summarized as follows: low cost, robust proven speed and position sensing technology (it can operate at temperatures in excess of $300°C$), self-generating electrical signal which requires no external power supply, fewer wiring connections which contribute to excellent reliability, and a wide range of output, resistance, and inductance requirements so that the device can be tailored to meet specific control requirements. Due to the fact that these sensors are very small, they can be embedded in places where other sensors may not fit. For instance, when sealed in protective cases they can be resistant to high temperatures and high pressures, as well as chemical attacks. Through the monitoring of the health of running motors, severe and unexpected motor failures can be avoided and control system reliability and maintainability can be improved. If the VR was integrated inside a motor case for an application in a harsh environment, sensor cables could be easily damaged in that environment. Then, a wireless and powerless sensing solution should be applied using electromagnetic pulses for passing through the motor casing to deliver the sensor signal to the motor controller.

2.3.3 Hall-effect Sensors

A Hall-effect sensor is a transducer that varies its output voltage in response to a magnetic field. The Hall-effect is named after Edwin Hall, who in 1879 discovered that a voltage potential develops across a current-carrying conductive plate when a magnetic field passes through the plate in a direction perpendicular to the plane of the plate, as illustrated in the Figure 2.9.

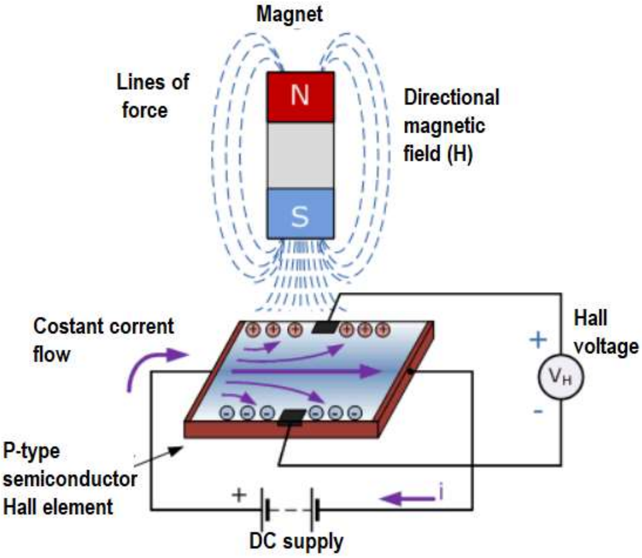

Figure 2.9 *- The Hall-effect sensors functioning.*

The fundamental physical principle behind the Hall-effect is the Lorentz force, which is:

$$\vec{F} = q\vec{v} \times \vec{B} \tag{2.1}$$

When an electron moves along a direction, v, perpendicular to the applied magnetic field, B, it experiences a force, F, the Lorentz force, that is normal to both the applied field and the current flow. In response to this force, the electrons move in a curved path along the conductor (this force tends to push them to one side of the conductor) and a build-up of charge at the sides of the conductors balance this magnetic influence producing a measurable voltage between the two sides of the conductor so a net charge, and therefore a voltage, develops across the plate. This Hall voltage, V_H, obeys the formula below, which shows that V_H is proportional to the applied field strength, and that the polarity of V_H is determined by the direction, either north or south, of the applied magnetic field. By this property, the Hall-effect is employed as a magnetic sensor.

$$V_H = \frac{I\ B_{\perp}}{\rho_n q t} \tag{2.2}$$

Where:

- V_H is the Hall voltage across the conductive plate;
- $B_{\perp}$ is the magnetic field perpendicular to the plate;
- I is the current passing through the plate;
- q is the magnitude of the charge of the charge carriers;
- $\rho_n$is the number of charge carriers per unit volume;
- t is the thickness of the plate.

Hall-effect sensors of low-cost and low resolution are wildly used in detecting the rotor position.

Whenever the rotor magnetic poles pass near the Hall sensors they give a high or low signal indicating the N or S pole is passing near the sensors, for this reason they are usually used only to detect the polarity of the machine while is running. Based on the combination of these three Hall-effect sensor signals, the exact sequence of commutation can be determined.

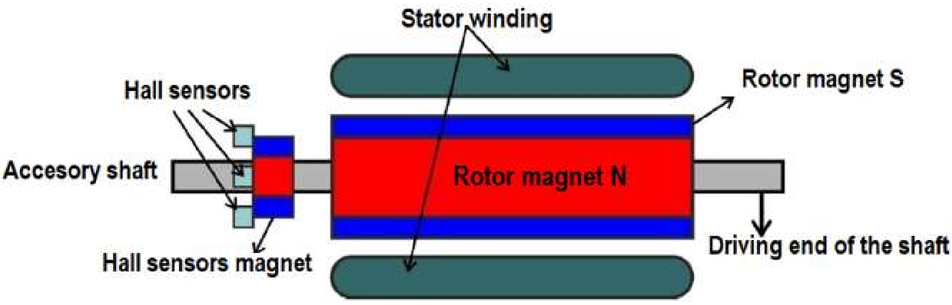

Figure 2.10 *– BCLDC motor traverse section.*

Figure 2.10 shows a transverse section of a brushless motor with a rotor that has alternate N and S permanent magnets. Hall-effect sensors are embedded into the stationary part of the motor. To embed the sensors into the stator is a complex process because any misalignment in these sensors with respect to the rotor magnets will generate an error in determination of the rotor position. To simplify the process of mounting the Hall-effect sensors onto the stator some motors may have the Hall sensor magnets on the rotor, in addition to the main rotor magnets [5]. Therefore, whenever the rotor rotates the Hall sensor magnets give the same effect as the main magnets. The Hall sensors are normally mounted on a printed circuit board and fixed to the enclosure cap on the non-driving end, they are distributed uniformly at 120^{el° to each other. They produce a new digital state every 60^{el° electrical degrees as shown in Figure 2.11, where electrical and normal degree do not differ [10].

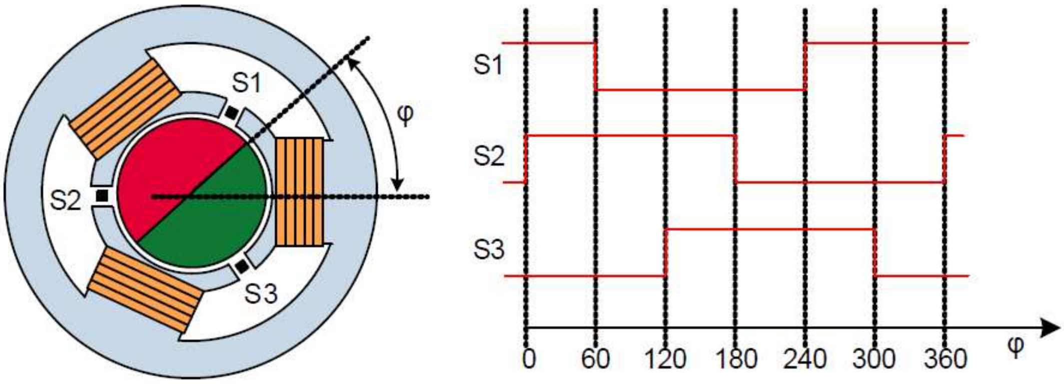

Figure 2.11 *– Switching pattern of the Hall-effect sensor S1 to S3 over one rotor revolution for a BLDC motor with three phase and one magnet pole pair.*

The rotor position can be measured at the beginning of each new digital state, therefore, some estimation algorithms should be conducted to achieve the angle of the rotor among the states. As will be described later, for the experimentations of this thesis it will be used this kind of structure. This enables users to adjust the complete assembly of Hall-effect sensors to align with the rotor magnets in order to achieve the best performance.

After this overview of the different methodologies to obtain rotor position and speed, can be concluded that there is no technique or technology that prevails completely over the other, but each application must evaluate the most cost-effective weighing both the economic and performance point of view. In regard to this thesis, it will be used a rotor position detection system based on the use of Hall-effect sensors as will be hereinafter described. In fact, while the encoder is a proven tested transducer, it has several practical drawbacks as cost, susceptibility to contaminations, size and durability [11]. These Hall-effect sensors cost about 1.50 \$. The installation cost is < 100 \$ since the Hall-effect sensors can be built into the stator. Calibration can usually be accomplished in software and is thus a small cost (< 100 \$).

2.4 Position Estimation with Hall-effect Sensors

High-resolution rotor position estimation is obtained through digital signal processing of the sensors outputs. The sensors detect when the rotor magnetic axis enters a new 60° sector. The electric angular position is generally expressed as

$$\theta(t) = \int_{t_k}^{t} \omega(t)dt + \theta_k \tag{2.3}$$

where $\omega(t)$ is the instantaneous electric angular velocity, t_k is the instant in which the magnetic axis enters sector $k(k = 1,2,\dots,6)$ and θ_k is the initial angle of sector k, measured from a fixed reference axis. Some different position estimation algorithms are briefly mentioned below [12].

2.4.1 Zeroth-Order Algorithm

The estimation is obtained by taking into account only the zeroth-order term of an approximated Taylor series expansion. This algorithm considers the speed inside each sector to be constant and equal to the average velocity in the previous sector. Rotor speed can then be approximated as

$$\omega(t) \cong \widehat{\omega}_{0k} = \frac{\frac{\pi}{3}}{\Delta t_{k-1}} \tag{2.4}$$

Where Δt_{k-1} is the time interval taken by the rotor magnetic axis to cross the previous sector $k-1$. The electric angular position can be obtained by numerical integration of (3.3.1), applying the constraint that the resulting angular position value has to be within sector k limits. The angular position is, thus, calculated as

$$\hat{\theta}_0(t) = \theta_k + \widehat{\omega}_{0k}(t - t_k) \tag{2.5}$$

$$\theta_k \leq \hat{\theta}_0(t) \leq \theta_k + \frac{\pi}{3} \tag{2.6}$$

2.4.2 First-Order Algorithm

The rotor speed can be approximated to a better degree by taking into account higher order terms of the Taylor series expansion. The first-order estimation algorithm is given as

$$\omega(t) \cong \widehat{\omega}_{1k} + \widehat{\omega}_{1k}^{(1)}(t - t_k) \tag{2.7}$$

Where the first derivative is approximated as

$$\widehat{\omega}_{1k}^{(1)} \cong \frac{\widehat{\omega}_{0k} + \widehat{\omega}_{0(k-1)}}{\Delta t_{k-1}} \tag{2.8}$$

The electric angular position comes out to be

$$\hat{\theta}(t) \cong \hat{\theta}_1(t) = \theta_k + \widehat{\omega}_{0k}(t - t_k) + \frac{\widehat{\omega}_{1k}^{(1)}}{2}(t - t_k)^2 \tag{2.9}$$

$$\theta_k \leq \hat{\theta}_1(t) \leq \theta_k + \frac{\pi}{3} \tag{2.10}$$

Only the first-order approximation has been considered because of increasing computational times, even if it is possible to use higher order approximations.

2.4.3 Vector-Tracking Observer

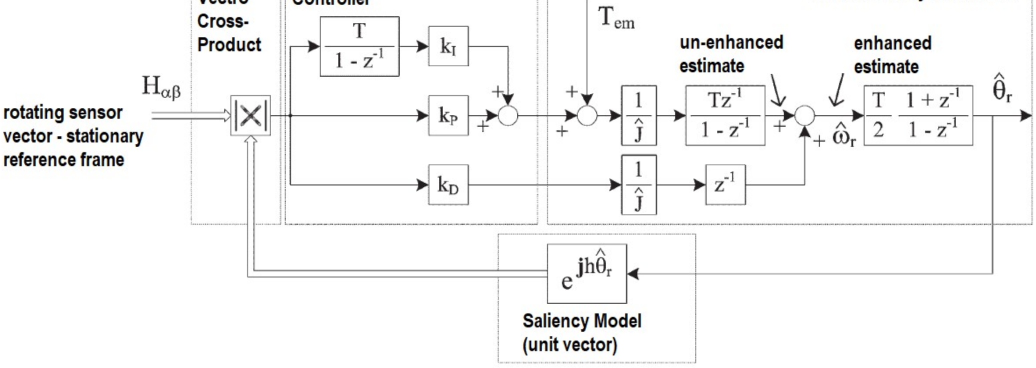

***Figure 2.11** – Vector Tracking Observer.*

As one can see in the figure above, the vector-tracking observer structure has two inputs: 1) a rotating vector containing position information and 2) a torque feedforward input to the mechanical model that provides position tracking above the observer bandwidth. The PID controller is used to force convergence. A rotating unit-vector based on the observed position is used as feedback to the phase detector. The estimated position is calculated using a latched-torque model of a simple rotational system. The rotating vector is obtained by processing the sensors signals. The six possible combinations of the sensors states can be interpreted as the vertices of a hexagon locus in the stationary reference frame, as shown in Figure 2.11.

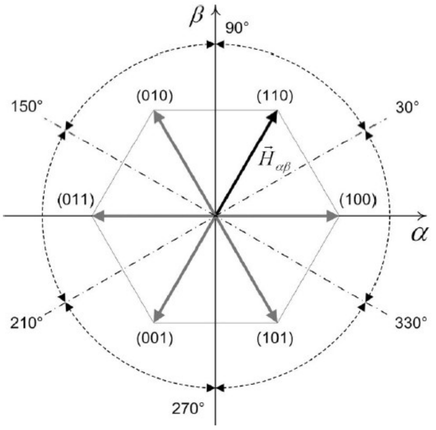

Figure 2.11 *– Quantized position vectors with Hαβ set at 60°.*

Here the rotating vector $H\alpha\beta$ is in the 60° position; this means that the rotor magnetic axis is somewhere between 60° and 120°. While the rotor axis crosses a 60° sector, the rotating vector remains in a fixed position, since there are only six possible states.

A consideration on tuning the vector-tracking observer given the quantized nature of the Hall-effect sensors is that the sample rate of the motor position depends on the motor speed. Between transitions of the Hall-effect sensor signal output, the observer relies on the feedforward torque command to estimate the rotor position. If the observer bandwidth is set too high, the resulting position estimate will be quantized. To solve this problem, the observer bandwidth should be speed dependent until a desired bandwidth is attained like the one proposed in [13] where are also investigate various harmonics decoupling strategies (to avoid position estimation errors) and is presented the tuning of the observer varying the observer gains linearly with the speed. Another improved vector-tracking observer is the one presented in [14] that consist of a position error detector, based on the vector cross product of the unit back-electromotive-force vectors obtained from a stator electrical model, and a proportional–integral-typed controller to make the position error rapidly converge to zero. This structure, that is similar to a phase-locked loop structure, does not only compensate the misalignment effect of Hall sensors but also enhance their transient operating capability.

2.4.4 Hybrid Observer

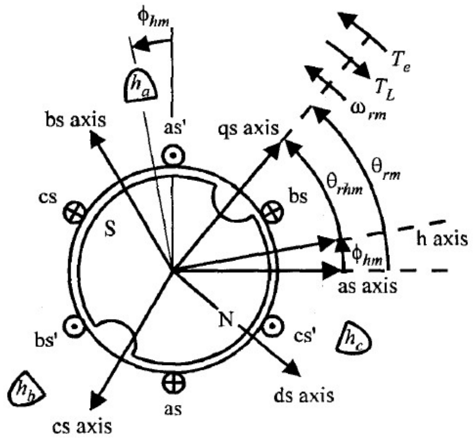

***Figure 2.12** – Permanent Magnet machine.*

The observer makes no use of any of the machine or drive parameters. Thus it can be used with any type of control strategy on any type of machine in which it is desirable to know the rotor position. The hybrid observer set forth in this section is based on the differential equation

$$\frac{d}{dt}\begin{bmatrix}\cos\theta_{rh}\\ \sin\theta_{rh}\end{bmatrix} = \begin{bmatrix}0 & -\omega_r\\ \omega_r & 0\end{bmatrix}\begin{bmatrix}\cos\theta_{rh}\\ \sin\theta_{rh}\end{bmatrix} \tag{2.11}$$

Where θ_{rh} is the electrical rotor position relative to the Hall-effect sensors, and ω_r is the electrical rotor speed.

If (2.11) could be solved numerically with no errors, the initial rotor position and the exact electrical rotor speed are both known the sine and cosine of the electrical rotor position relative to the Hall-effect sensors, $\sin\theta_{rh}$ and $\cos\theta_{rh}$, could be determined. Therefore the electrical rotor position θ_r could be determined from $\sin\theta_r$ and $\cos\theta_r$, using trigonometric. Unfortunately, there are no means to determine either the initial rotor position or the exact electrical rotor speed. Nevertheless, (2.11) can still be used to accurately determine $\sin\theta_{rh}$ and $\cos\theta_{rh}$, provided that it is augmented with information available from the Hall-effect sensors. Specifically [15], the information from the Hall-effect sensors can be used to:

- determine limits on $\sin\theta_h$ and $\cos\theta_h$, bounding in this way the error in the estimation of these quantities (where θ_h is the angle corresponding to the state of the Hall-effect sensors);
- determine the exact value of $\sin\theta_{rh}$ and $\cos\theta_{rh}$ whenever there is a transition of one of the outputs of the Hall-effect sensors;
- estimate electrical rotor speed based on the length of time which pass between Hall-effect sensors transitions.

On each occurrence of a Hall-effect transition, the rotor speed can be estimated based on the time elapsed since the previous Hall-effect transition. In particular

$$\widehat{\omega}_r = \frac{\Delta\theta_{rh}}{\Delta \mathrm{t}} \qquad (2.12)$$

Where $\Delta\theta_{rh}$ is calculated based upon the rotor position corresponding to the measured current and previous Hall-effect transitions. Prior to the first Hall-effect sensors transition, the estimated electrical rotor speed is taken to be zero. At the first Hall-effect transition the previous rotor position (since there is no a previous transition) is taken to be the midpoint value of $\Delta\theta_{rh}$ corresponding to the initial Hall-effect transition. The combination of the information that can be deduced from the Hall-effect states with (2.11) yields the hybrid observer depicted in Figure 2.13.

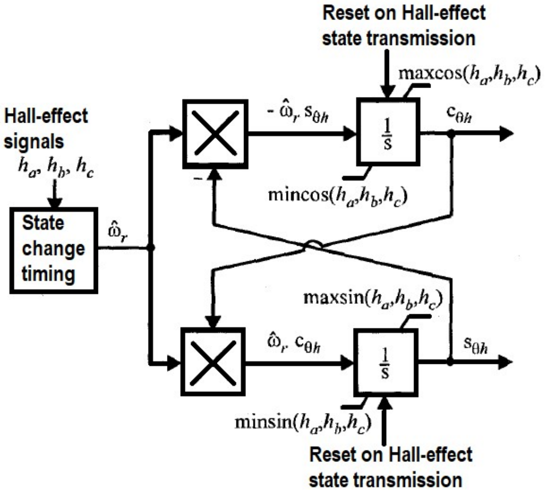

Figure 2.13 *- Hybrid Observer block diagram.*

Therein, $s_{\theta h}$ and $c_{\theta h}$ are, respectively, the estimated values of $\sin\theta_{rh}$ and $\cos\theta_{rh}$ and ω_r denotes the estimated electrical rotor speed. As can be seen, the structure of the control is based on (2.11), however, each of the integrators is subjectred to a variable limit which is a function of the Hall-effect state (h_a, h_b, h_c) as described in Table 2.1. These integrators are furthermore reset to the value specified in Table 2.2 every time a transition in Hall-effect state occurs.

Table 2.1 *- Bounding function vs. Hall state.*

Hall state			**Bounding function**			
h_a	h_b	h_c	$(maxsin\theta_h)$	$minsin\theta_h$	$maxcos\theta_h$	$mincos\theta_h$
0	0	1	$-1/2$	-1	0	$-\sqrt{3/2}$
0	1	0	1	$1/2$	0	$-\sqrt{3/2}$
0	1	1	$1/2$	$-1/2$	$-\sqrt{3/2}$	-1
1	0	0	$1/2$	$-1/2$	1	$\sqrt{3/2}$
1	0	1	$-1/2$	-1	$\sqrt{3/2}$	0
1	1	0	1	$1/2$	$\sqrt{3/2}$	0

Table 2.2 *- State transition points.*

Sensor transition	h_a	h_b	h_c	$\sin(\theta_{rh})$	$\cos(\theta_{rh})$
h_a	x	0	1	-1	0
h_a	x	1	0	1	0
h_b	0	x	1	$-1/2$	$-\sqrt{3/2}$
h_b	1	x	0	$1/2$	$\sqrt{3/2}$
h_c	0	1	x	$1/2$	$-\sqrt{3/2}$
h_c	1	0	x	$-1/2$	$\sqrt{3/2}$
x = irrilevant					

One final calculation is necessary to implement this Hybrid Observer. In particular, a method is set forth to determine the sine and cosine of electrical rotor position relative to the as-axis, which is required to make the reference frame transformation, instead of the electrical rotor position relative to the Hall-effect sensors. Since

$$\theta_r = \theta_{rh} + \phi_h \tag{2.13}$$

Where ϕ_h is the electrical displacement between the h-axis and a-phase-axis. It follows that

$$\sin(\theta_r) = \sin(\theta_{rh})\cos(\phi_h) + \cos(\theta_{rh})\sin(\phi_h) \tag{2.14}$$

$$\cos(\theta_r) = \cos(\theta_{rh})\sin(\phi_h) - \sin(\theta_{rh})\cos(\phi_h) \tag{2.15}$$

Thus, it terms of the estimated value for $\sin(\theta_{rh})$ and $\cos(\theta_{rh})$

$$\sin(\theta_r) = s_{\theta h}\cos(\phi_h) + c_{\theta h}\sin(\phi_h) \tag{2.16}$$

$$\cos(\theta_r) = c_{\theta h}\cos(\phi_h) - s_{\theta h}\sin(\phi_h) \tag{2.17}$$

At first, the electrical rotor speed is assumed to be zero. The initial conditions for $s_{\theta h}$ and $c_{\theta h}$ are determined from the initial Hall-effect sensor readings. In particular, the initial conditions are chosen to be in the centre of the interval over which the current Hall-effect state is constant, as listed in Table 2.3. In this way the maximum possible error in the initial rotor position estimate is $\pi/6$.

Table 2.3 *– Initial conditions.*

Initial Hall state			**Initial conditions**		
h_a	h_b	h_c	θ_h	$s_{\theta h}$	$c_{\theta h}$
0	0	1	$4\pi/3$	$-\sqrt{3/2}$	$-1/2$
0	1	0	$2\pi/3$	$\sqrt{3/2}$	$-1/2$
0	1	1	π	0	-1
1	0	0	0	0	1
1	0	1	$5\pi/3$	$-\sqrt{3/2}$	$1/2$
1	1	0	$\pi/3$	$\sqrt{3/2}$	$1/2$

In this thesis work, a different detection method has been developed. As it will be described on the following paragraph, this is based on the utilization of the back-EMF information that are obtained from the Hall-effect sensors and then elaborated with a Multi-Complex Coefficient-Filter Phase-Looked Loop.

2.5 Multiple-Complex Coefficient-Filter-based Phase-Looked Loop Synchronization Technique

The aim of this thesis work is develop a sensored control system based on the use of Hall-effect sensors. It this work, there will be use digital Hall-effect sensors in the Simulink simulations, and analogic Hall-effect sensors in the experimentations. These last ones will be digitalized since the majority of the commercial machine are equipped with digital sensors and not analogic. This because they are usually used only to detect the polarity of the machine while is running. They require less post processing and less electronics since they give a signal that can be used directly on a microcontroller in a simpler way. Furthermore they are less sensible to the temperature variations and are way less affected by noise.

In both, Simulink simulations and experimentations, is used the same position detection scheme that, as it will be better described in the following, extracts the real and imaginary part of the back-EMF, U_α and U_β, from the three Hall-effect sensor signal and thus uses the multiple-complex coefficient-filter(MCCF)-based phase-looked loop synchronization technique.

2.5.1 SFR-PLL

A Synchronous Reference Frame Phase-Locked Loop (SRF-PLL) is a commonly used synchronization technique due to the advantages it offers such as ease of implementation and robust performance.

A Phase-Looked Loop, is a nonlinear closed-loop feedback control system which synchronizes its output signal in frequency, as well as in phase, with an input signal. A basic PLL consists of three building blocks: a Phase Detector (PD), a Loop Filter (LF), and a Voltage-Controlled Oscillator (VCO). Figure 2.14 illustrates the basic scheme of a conventional Synchronous Reference Frame PLL. In this type of PLL, the three-phase input voltages are transformed into the *DQZ* synchronous reference frame by applying a combination of Clark and Park transformations. Using a feedback loop, the angular position of the *DQZ* reference frame is regulated in such a way that either the *d*- or *q*-axis component (depending on the transformation) becomes zero.

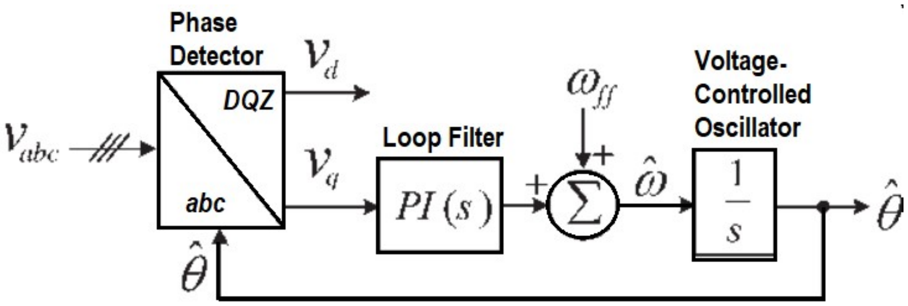

Figure 2.14 *- Synchronous Reference Frame Phase-Looked Loop.*

Under ideal conditions, without any harmonic distortion, it would be sufficient the SFR PLL alone, that with a high bandwidth yields a satisfactory performance both in terms of the phase/frequency tracking capability and the dynamic response. In case the signals are distorted with high order harmonics, the SRF PLL can still work if its bandwidth is reduced to reject and cancel out the effect of the harmonics at the cost of the PLL response speed reduction [16]. Even if in greed application, several advanced PLLs have been proposed in recent years, as alternatives to the conventional SRF-PLL to overcome this drawback. Typically, their common idea is to employ the specific "filtering" techniques to extract the fundamental-frequency positive-sequence component which is then fed to a conventional SRF-PLL.

For example Yuan *et al.* presented a positive sequence filter to extract the fundamental positive sequence component from the distorted unbalanced PCC (Point of Common Coupling of the power electronic converter) voltage [17]. After this were presented for similar purpose the sinusoidal signal integrator[17], double second-order generalized integrator[17], and the fast PLL[17] based on software PLL. On the other hand, Ghartemani and Iravani presented an Enhanced PLL (EPLL) [17], whose core is an adaptive filter. Unlike the abovementioned mechanism, it first filters the harmonics and keeps frequency adaptive in a nonlinear way for each unit in the three-phase system, and then, the fundamental positive sequence component can be directly obtained by the symmetrical component method [17]. Similar to EPLL, a powerful nonlinear approach was presented by Yazani *et al.* [17], which is based on an adaptive notch filter (ANF) and has a fast dynamic response compared to EPLL. Another interesting approach presented by Rodriguez *et al.* is a Decoupled Double Synchronous Reference-Frame (DDSRF) PLL [17] to prevent the double-frequency detection errors, caused by the fundamental-frequency negative-sequence component The positive and negative sequence component can be accurately extracted by the double synchronous frame transformations and an innovative decoupling network. Another approach presented by Xiao *et al.* [16] is a multiple reference frame based PLL (MRF-PLL). The MRF-PLL utilizes the same idea of the DDSRF-PLL, except that it has a more straightforward implementation. Alternative approach reported by Rodriguez *et al.* [16] is a dual second-order generalized integrator based PLL (DSOGI-PLL), which works based on the Instantaneous Symmetrical Components (ISC) theory in the stationary ($\alpha\beta$) reference frame. However, for an accurate estimation, all the mentioned approaches should reduce the bandwidth under highly distorted conditions to attenuate the harmonics, which will slow the transient response.

That is not an acceptable solution and inasmuch the back-EMF has several harmonic components the real and imaginary part of the back-EMF are then filtered using a MCC filter since for the position estimation is needed only the fundamental component.

2.5.2 MCCF-PLL

The Multi-Complex Coefficient-Filter is utilized for harmonic extraction and has the unique feature that the fundamental-frequency information and other harmonics components can be accurately and rapidly estimated with no need of symmetrical component method or so many complicated rotating frame transformation (typical of the modified PLLs proposed to this aim, as the ones listed above).

Can be though to use a classic bandpass filter in order to extract the fundamental components from the back-EMF with immunity to the other harmonics. However, these conventional Real-Coefficient Filters (RCFs) have only the frequency-selective property, but not polarity-selective property and this means that these filters can not make the distinction between the positive and negative polarities for the same frequency. This concept is illustrated in Figure 2.15 which shows the bode diagram of a typical real-coefficient second-order bandpass filter. It can be observed that both positive and negative sequences will pass the bandpass filter without attenuation since the attenuation ratio at both the fundamental positive and negative sequences frequencies is 1. Thus, the positive and negative sequences can not be extracted directly by these types of filters [17]. Moreover, the cut-off frequency of these filters should be reduced to achieve better performance at the expense of the dynamic response in the case of highly distorted environments.

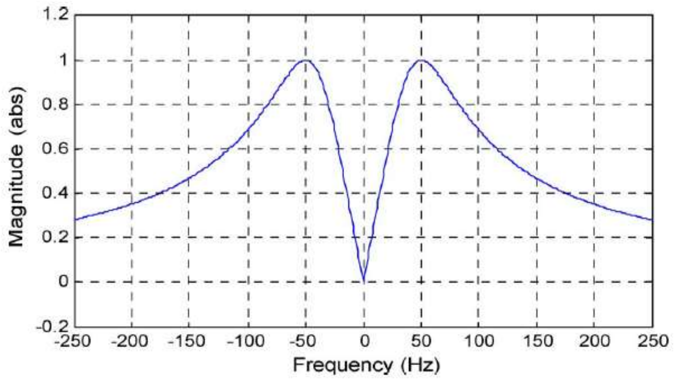

Figure 2.15 *- Bode diagram of a second-order bandpass filter.*

The MCCF structure is illustrated in Figure 2.16. It is composed of many Complex-Coefficient Filters (CCF), working in a collaborative way, each of which is responsible for extracting a selected sequential component from the input voltage.

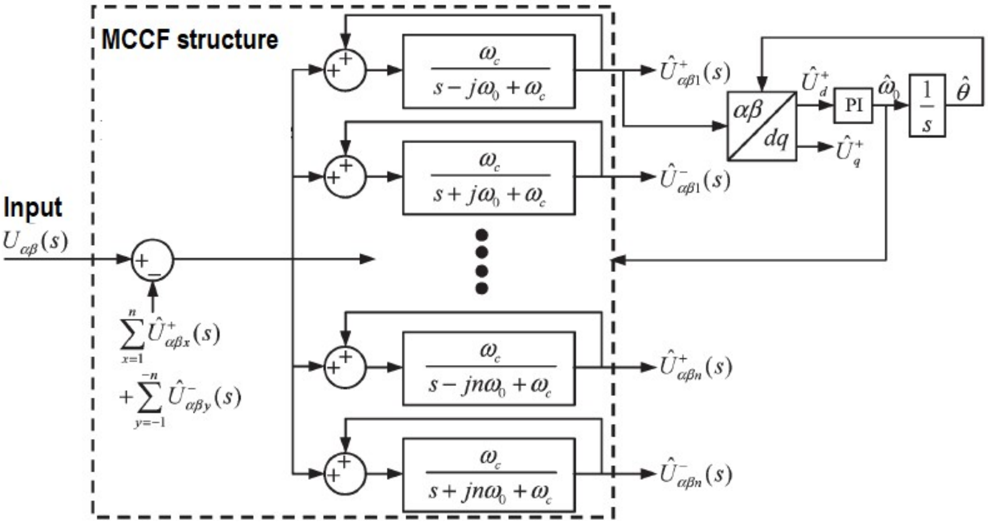

Figure 2.16 *– MCCF-based PLL.*

The main advantage of this filter is that it has both frequency and polarity-selective property. An ideal CCF should provide fast response for the real-time signal extraction, keep unity gain and zero phase shift at the selected frequency and deep attenuation at the other frequencies. The first order CCF can be expressed with the equation:

$$CCF(s) = \frac{\omega_c}{s - j\widehat{\omega}_0 + \omega_c} \tag{2.18}$$

And the corresponding bode diagram is shown in Figure 2.18, where ω_c , cut-off frequency, and ω_0 , extracted frequency, are set to $314\ rad/s$.

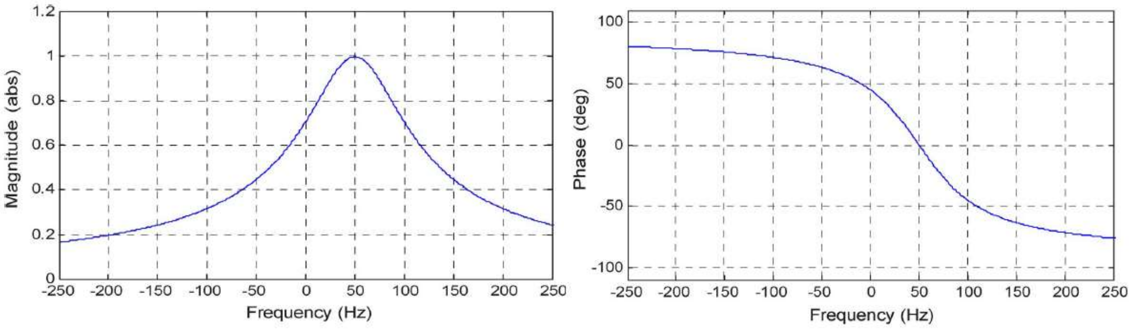

Figure 2.18 *- Bode diagram of a Complex-Coefficient Filter.*

From the previous equation it can be observed that this filter can extract the specified frequency (ω_0) component with unity gain and zero phase shift. Meanwhile at the other frequencies, the amplitude attenuation ratio and the phase shift are respectively

$$\frac{\omega_c}{\sqrt{(\omega - \widehat{\omega}_0)^2 + \omega_c^2}} \tag{2.19}$$

$$tan^{-1}\frac{(\omega_c - \omega)}{\omega_c} \tag{2.20}$$

Regarding the MCCF shown in Figure 2.16 the $U_{\alpha\beta}$ is in the input and on output there are the estimated fundamental and harmonic components: $\widehat{U}^{+}_{\alpha\beta1}$, $\widehat{U}^{-}_{\alpha\beta1}$,…, $\widehat{U}^{+}_{\alpha\beta n}$, $\widehat{U}^{-}_{\alpha\beta n}$. Since the speed of the motor can vary in a wide range, also the back-EMF does it, so it is needed a frequency-adaptive MCCF, like the one represented. After have transformed the signal in the synchronous reference frame and have selected the q component, the SRF PLL is used to estimate the fundamental frequency positive component, to extract the rotor speed and feed it back to MCCF. In the SRF PLL is also obtained the rotor position after the integrator block.

Based on Figure 2.16 can be derived the equations for the estimated fundamental positive-sequence component as (2.21) and (2.22).

$$\hat{v}^{+}_{\alpha,1}(s) = \frac{\omega_c}{s - j\widehat{\omega}_0 + \omega_c} \times \left(v_\alpha(s) - \sum_{h=1}^{n}\left[\hat{v}^{+}_{\alpha,h}(s) + \hat{v}^{-}_{\alpha,h}(s)\right] + \hat{v}^{+}_{\alpha,1}(s) \right) \tag{2.21}$$

$$\hat{v}^{+}_{\beta,1}(s) = \frac{\omega_c}{s - j\widehat{\omega}_0 + \omega_c} \times \left(v_\beta(s) - \sum_{h=1}^{n}\left[\hat{v}^{+}_{\beta,h}(s) + \hat{v}^{-}_{\beta,h}(s)\right] + \hat{v}^{+}_{\beta,1}(s) \right) \tag{2.22}$$

There are several methods for implement the submodules of MCCF, in this thesis is used the one corresponding to the block diagram in Figure 2.19.

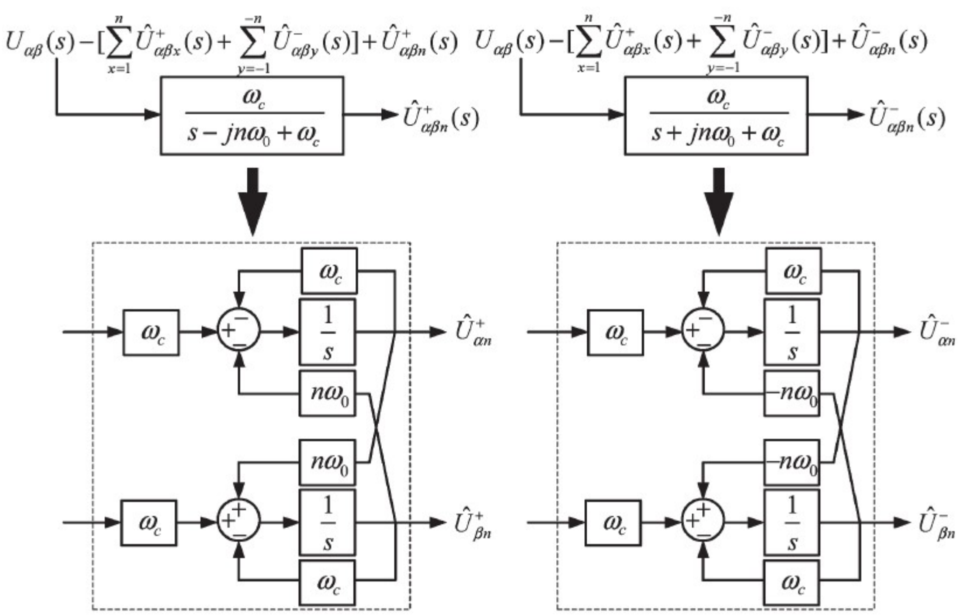

Figure 2.19 *– Submodule structure of a MCCF.*

Based on the last figure, and performing some mathematical manipulations, we can rewrite (2.21) and (2.22) as (2.23) and (2.24), respectively.

$$\hat{v}^{+}_{\alpha,1}(s)=\frac{\omega_c}{s+\omega_c}\times\left(v_\alpha(s)-\sum_{h=2}^{n}\hat{v}^{+}_{\alpha,h}(s)-\sum_{h=1}^{n}\hat{v}^{-}_{\alpha,h}(s)\right)-\frac{\widehat{\omega}_0}{s+\omega_c}\hat{v}^{+}_{\beta,1}(s) \tag{2.23}$$

$$\hat{v}^{+}_{\beta,1}(s)=\frac{\omega_c}{s+\omega_c}\times\left(v_\beta(s)-\sum_{h=2}^{n}\hat{v}^{+}_{\beta,h}(s)-\sum_{h=1}^{n}\hat{v}^{-}_{\beta,h}(s)\right)-\frac{\widehat{\omega}_0}{s+\omega_c}\hat{v}^{+}_{\alpha,1}(s) \tag{2.24}$$

Substituting (2.23) into (2.24), and (2.24) into (2.23), and rearranging the results into matrix form, gives (2.25) [16]. Following a similar procedure, we can also derive (2.26).

$$\begin{bmatrix}\hat{v}^{+}_{\alpha,1}(s)\\ \hat{v}^{+}_{\beta,1}(s)\end{bmatrix}=\frac{\omega_c}{(s+\omega_c)^2+\widehat{\omega}_0{}^2}\begin{bmatrix}s+\omega_c & -\widehat{\omega}_0\\ \widehat{\omega}_0 & s+c\end{bmatrix}\times\begin{bmatrix}v_\alpha(s)-\sum_{h=2}^{n}\hat{v}^{+}_{\alpha,h}(s)-\sum_{h=1}^{n}\hat{v}^{-}_{\alpha,h}(s)\\ v_\beta(s)-\sum_{h=2}^{n}\hat{v}^{+}_{\beta,h}(s)-\sum_{h=1}^{n}\hat{v}^{-}_{\beta,h}(s)\end{bmatrix} \tag{2.25}$$

$$\begin{bmatrix}\hat{v}^{-}_{\alpha,1}(s)\\ \hat{v}^{-}_{\beta,1}(s)\end{bmatrix}=\frac{\omega_c}{(s+\omega_c)^2+\widehat{\omega}_0{}^2}\begin{bmatrix}s+\omega_c & \widehat{\omega}_0\\ -\widehat{\omega}_0 & s+\omega_c\end{bmatrix}\times\begin{bmatrix}v_\alpha(s)-\sum_{h=1}^{n}\hat{v}^{+}_{\alpha,h}(s)-\sum_{h=2}^{n}\hat{v}^{-}_{\alpha,h}(s)\\ v_\beta(s)-\sum_{h=1}^{n}\hat{v}^{+}_{\beta,h}(s)-\sum_{h=2}^{n}\hat{v}^{-}_{\beta,h}(s)\end{bmatrix} \tag{2.26}$$

As mentioned above, this filter has the further advantage respect a classical bandpass filters of the polarity-selective property to extract the positive or negative sequence in a straightforward manner, but has the same features as real coefficient filter that a tradeoff between the extraction accuracy and response speed should be made if the signal in input is contaminated with unbalance and distortions.

In the end, in order to tune the SFR PLL to obtain the desired performance, its linear model is shown in Figure 2.20, and the closed-loop transfer function is the following

$$H(s) = \frac{\hat{\theta}(s)}{\hat{\theta}^{*}(s)} = \frac{2\xi\omega_n s + \omega_n^2}{s^2 + 2\xi\omega_n s + \omega_n^2} \tag{2.27}$$

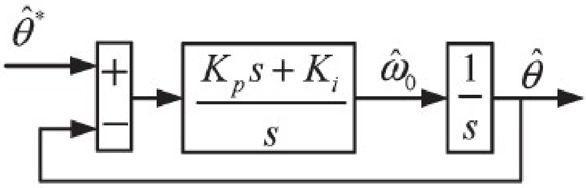

Figure 2.20 *– SRF lineal model.*

It has to take in consideration that an interaction will appear when SFR PLL is cascades to the MCCF structure for frequency adaptivity, and a practical way to mitigate the interaction between the MCCF structure and the SFR PLL is to make the estimator (MCCF) faster than the control (SFR PLL).

CHAPTER 3

SIMULINK SIMULATIONS

In this chapter will be shown and described the speed and position estimation of a Permanent Magnet motor, implemented with MATLAB Simulink using the Sim-PowerSystem Toolbox. It will show the results of simulations to test the proper functioning of the control.

3.1 Overall Electric Drive

The drive control is responsible of the system dynamic performance, namely provides a torque value that allows the tracking of a given speed reference by the load. The implementation of the control law is the result of a compromise between specifications that aim to satisfy opposing requirements, such as the response rate and the absence of oscillations in the output variable or the obtaining of an adequate margin of stability. The diagram of the speed drive control adopted is based on synchronous controllers of current, and an illustration is in the Figure 3.1.

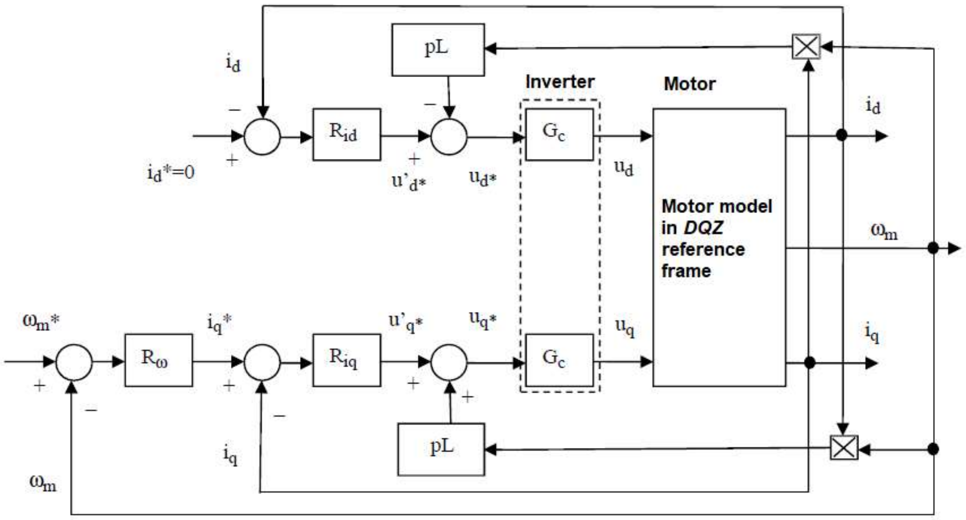

***Figure 3.1** – Speed drive control diagram.*

In this figure above is represented the general scheme of a speed control that is on the base of several speed controls developed so far, and it will not be analyzed. The overall view of the control developed in this work is on the following Figure 3.2.

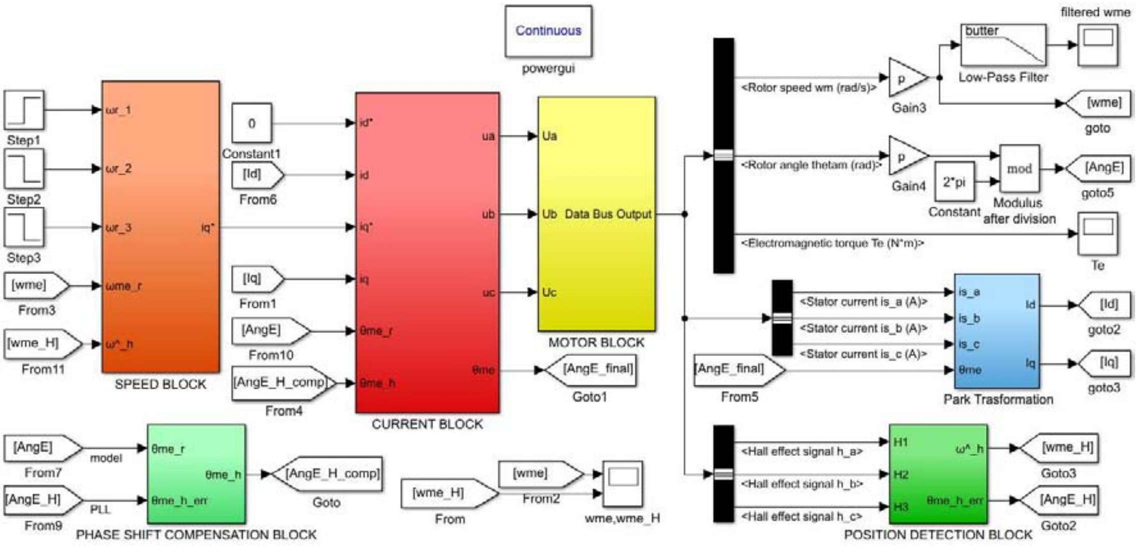

***Figure 3.2** - Simulink speed/position detection overall scheme.*

The aim of the control here developed is the frequency and position estimation of an IPM motor. To this end is used, for the whole drive, a synchronous reference system with the rotor, that is a reference system (*DQZ*) in rotation relative to the stator with angular speed

$$\omega_{me} = \frac{d\theta_{me}}{dt} \tag{3.1}$$

Where ω_{me} is the electric-mechanical speed, or rather the mechanical speed of the machine, ω_m, multiply by its number of pole pairs that is $p = 3$, and θ_{me} is the electric-mechanical angle, that is the angle position of the machine, θ_m, multiply by its number of pole pairs as shown by the equations:

$$\omega_{me} = p\omega_m \tag{3.2}$$

$$\theta_{me} = p\theta_m \tag{3.3}$$

Subsequently, all the blocks represented in Figure 3.2 will be described. Here, is just clarified the function of the *powergui* block. It allows to choose one of these methods to solve your circuit:

- Continuous, which uses a variable-step solver from Simulink.
- Discretization of the electrical system for a solution at fixed time steps.
- Phasor solution.

As can be seen, in this case is used the Continuous method with a simulation time of 7.5 s.

Due to font restrictions, the names of the variables used in the model could not be the same of the ones used below to describe the functioning of the system, but the input and output names of the different blocks correspond to the correct name. Furthermore, the images of the different signals present in this chapter, that will show the simulation results, are taken with the Simulink Scope block. This is placed at the signals, and displays time domain signals generated during simulation, with respect of the simulation time.

3.2 Speed Block

The *SPEED BLOCK* is shown in the Figure 3.3 below.

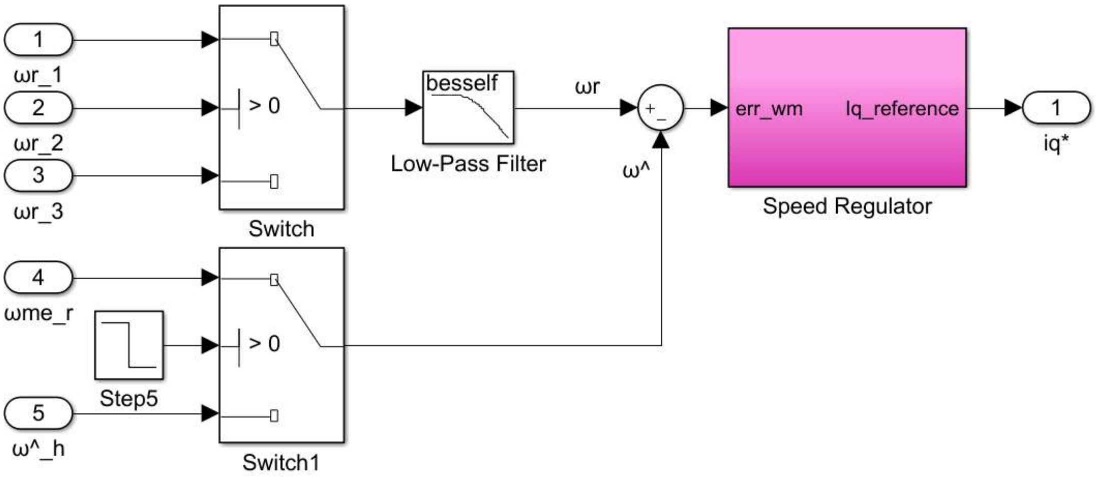

***Figure 3.3** – SPEED BLOCK diagram.*

The speed reference ω_r is compared with the speed derived from the measured quantities of the Hall-effect sensors, that is the estimated frequency of the machine $\widehat{\omega}$, and through the *Speed Regulator* (that will be described in §3.7) produces the reference quadrature current i_q^* which, as known, is proportional to the torque. The reference of direct current i_d^*, used to generate the magnetic flux in the machine, is instead maintained at zero in the course of the simulations as can be seen in Figure 3.2. Operation with speeds higher than the base speed is not of interest in this work.

As can be noticed, the given speed reference is not a constant speed but a speed profile consisting on three speed steps, as shown in Figure 3.4: ω_{r_1}, ω_{r_2}, ω_{r_3}.

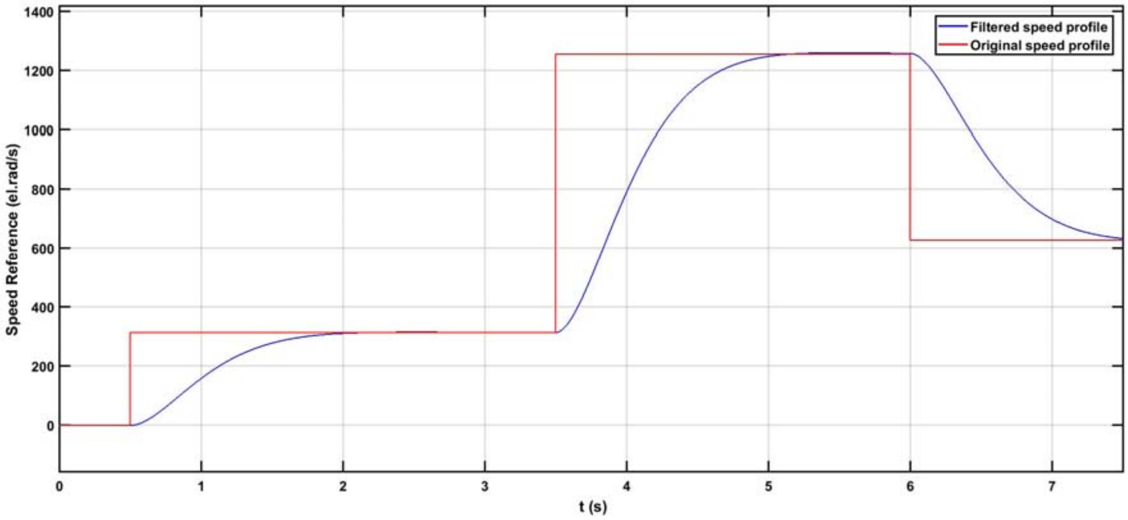

Figure 3.4 *– Speed reference profile.*

In this case the speed follows the values given by the steps, starting from the zero value:
$0\,rad/sec - 314.159\,rad/sec - 942.477\,rad/sec - 628.318\,rad/sec.$

This solution has been adopted to better simulate the real behaviour of an electric motor on his usual operating mode during which a speed change is required, and it has been chosen a speed profile that covers all the speed range of the IPM model provided by Simulink. Anyway, the same results can be obtained with a constant speed reference. Moreover, as shown in the figure 3.4 with the blue line, the speed steps are filtered with a Bessel second order *Low-Pass Filter* with bandpass edge frequency of $0.5\,Hz$. This is done to prevent the PLL of the frequency/position estimation from loosing the reference in correspondence of an abrupt speed change that can destabilize the phase engagement.

Must be noted that the estimated speed, $\widehat{\omega}_h$, is not immediately compared with the reference ω_r. The comparison take place after *0.9s* from the beginning of the simulation. Before this time, is used the electric speed, ω_{me}^{r}, given from the Simulink model of the machine. The *Switch1* is the component in charge of this exchange of values. This is due to the fact that at zero speed the rotor position is not known. Besides, at low speed, like the ones within the speed range between *0s* and *0.9s*, the back-EMF obtained from the Hall-effect signals is not correctly estimated because these sensors provide discrete absolute-position information with electrically ±*30°* resolution with a low resolution rotor angle feedback which affects the estimation mainly at the start and at low speed.

3.3 Current Block

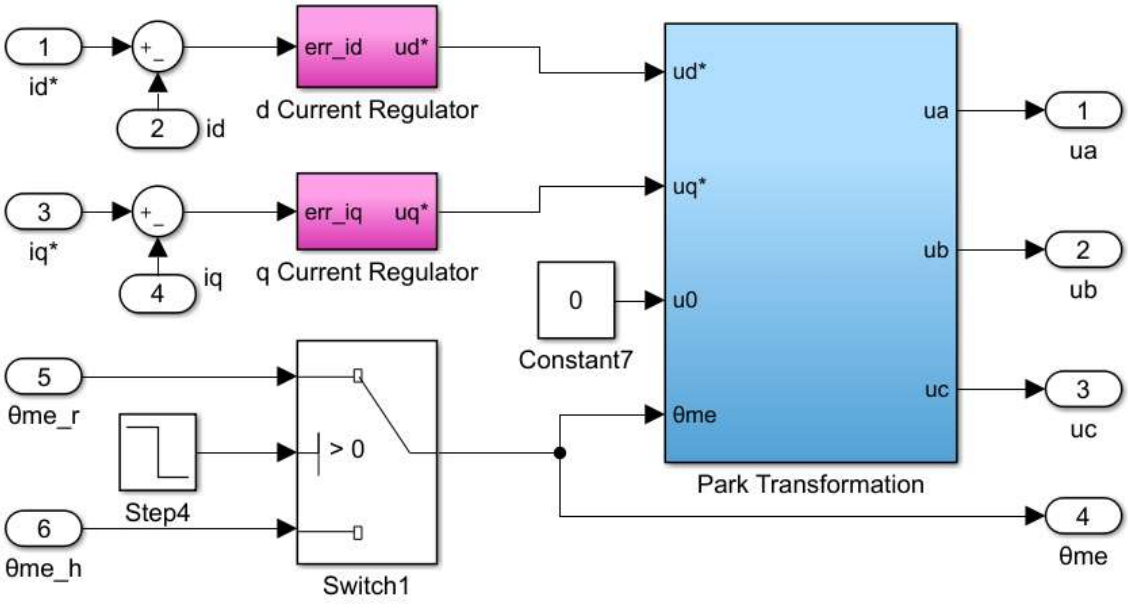

Figure 3.5 *- CURRENT BLOCK diagram.*

In the *CURRENT BLOCK* represented in the Figure 3.5, the two current references i_d^*, $i_q^*$are compared with the respective measures i_d, i_q (given in synchronous reference system) and the resulting errors are processed by the *d/q Current Regulator* (that will be described in §3.6) to produce the voltage references u_d^* and u_q^*. The current measures come from the three stator currents $i_{s\_a}, i_{s\_b}, i_{s\_c}$, and are then transformed in the i_d and i_q used for the comparison. These stator currents are extracted from the Simulink model of the machine, as shown in Figure 3.2. The voltage references obtained are then converted into the corresponding references u_a, u_b, u_c, which, through a PWM control, control the inverter that feeds the motor which in turn returns the resulting stator current.

The transformation, adopted in the currents and voltages conversions, is the *Park Transformation* that converts vectors in the *ABC* stationary reference frame to the *DQZ* reference frame, and vice versa. The *DQZ* reference frame is a reference frame rotating at the electric speed of the machine rotor, so the angle used on the transformation is the electric angle of the rotor of the motor. The Park transformation matrices are the following:

$$T_{abc\rightarrow dq0} = \frac{2}{3}\begin{bmatrix} \cos(\theta_{me}) & \cos\left(\theta_{me}-\frac{2\pi}{3}\right) & \cos\left(\theta_{me}-\frac{4\pi}{3}\right) \\ -\sin(\theta_{me}) & -\sin\left(\theta_{me}-\frac{2\pi}{3}\right) & -\sin\left(\theta_{me}-\frac{4\pi}{3}\right) \\ \frac{1}{2} & \frac{1}{2} & \frac{1}{2} \end{bmatrix} \tag{3.4}$$

$$T_{dq0\rightarrow abc} = \begin{bmatrix} \cos(\theta_{me}) & -\sin(\theta_{me}) & \frac{1}{2} \\ \cos\left(\theta_{me}-\frac{2\pi}{3}\right) & -\sin\left(\theta_{me}-\frac{2\pi}{3}\right) & \frac{1}{2} \\ \cos\left(\theta_{me}-\frac{4\pi}{3}\right) & -\sin\left(\theta_{me}-\frac{4\pi}{3}\right) & \frac{1}{2} \end{bmatrix} \tag{3.5}$$

In this case the output vector $[u_a, u_b, u_c]$ is obtained from a matrix product between the Park transformation matrices (3.5) and the input vector $[u_d^*, u_q^*, u_0^*]$.

In reality, as it happens for the speed comparison, the angle used, θ_{me} , is a combination of the one given from the Simulink model of the machine, θ_{me}^r , for the first 0.9s, and the angle estimated from the MCCF-PLL, θ_{me}^h. The following Figure 3.6 shows as the fluctuations of the two angles, θ_{me}^r and θ_{me}^h, differ from each other for almost the first nine seconds, after that they are nearly coincident. The central part of the image is cut off for lack of space on the page and because the two angles overlap.

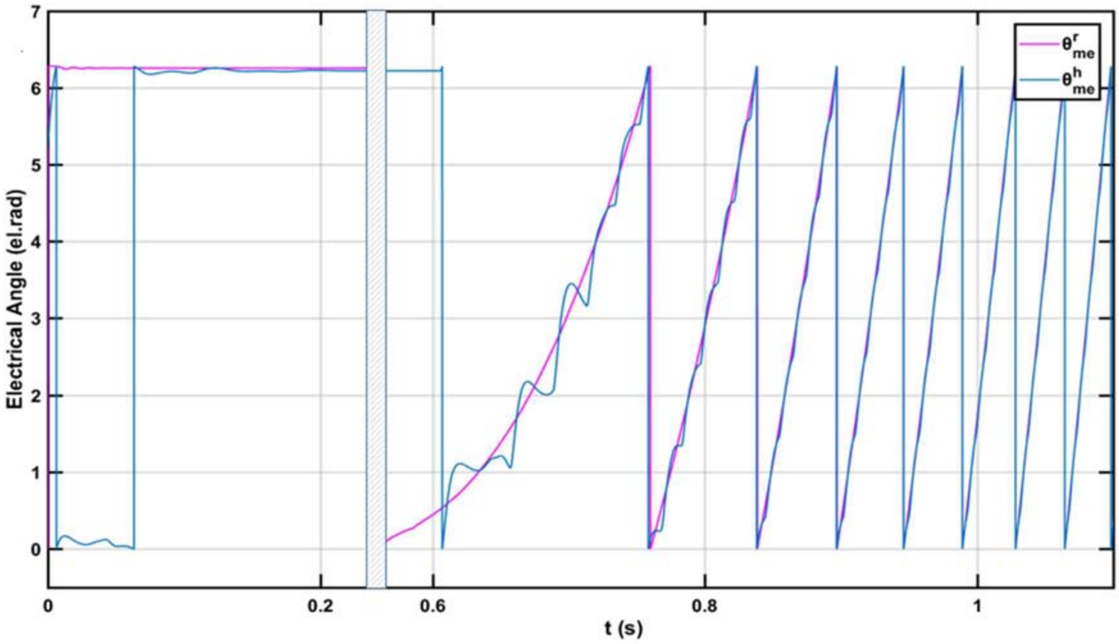

Figure 3.6 *- Real and estimated electrical angle comparison.*

3.4 Motor block

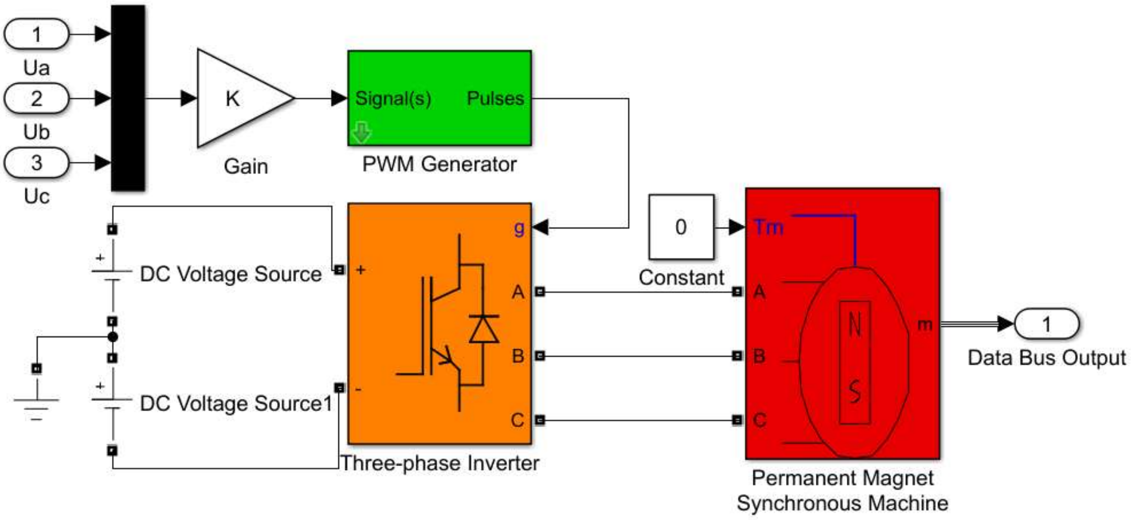

Figure 3.7 *- MOTOR BLOCK diagram.*

For the kind of motor used, is necessary to have a three-phase voltage supply with controllable amplitude and frequency. For this purpose is used a three-phase voltage source inverter controlled with a PWM (Pulse Width Commutation) signal. The DC bus of the inverter is set to $V_{DCbus} = 560\,V$, according to the value required by the machine model. The carrier frequency of the PWM generator and so the commutation frequency of the inverter is set to

$f_c = 10000\ Hz$, according to the one of the inverter used for the experimentations. The two *DC Voltage Source* are set to half of the V_{DCbus} value. A general representation of the inverter is shown in Figure 3.8.

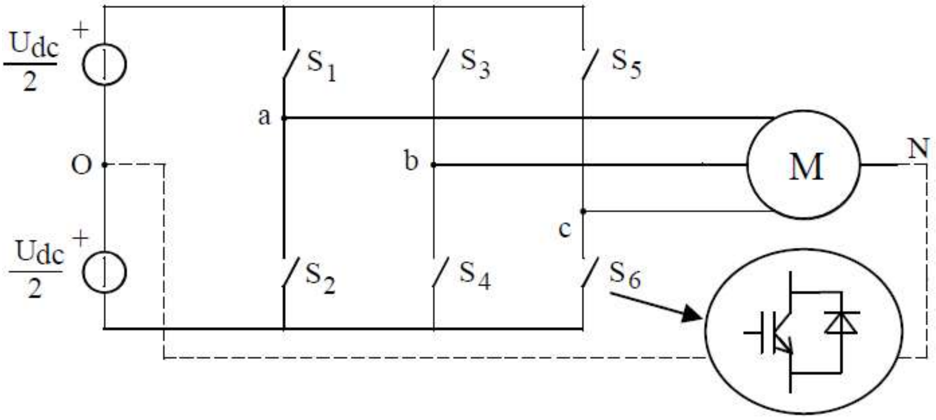

Figure 3.8 *- Inverter description scheme.*

It essentially consists of six electronic power switches connected to form three inverter legs, one for each phase of the motor. In practice, each of the switches consists of the parallel between a power electronic component, in this case are IGBT(Insulated Gate Bipolar Transistor), controlled on ignition and shutdown, capable of conducting the current from the top to bottom of the figure, and a diode (not controlled) arranged to conduct current from the bottom to top. The diodes are necessary due to the inductive nature of the load to provide a reclosing of the currents at each opening of the switches. In addition, series RC snubber circuits are connected in parallel with each switch device. Command to close the top switch of a branch connects the motor phase to the positive DC rail; of course, in order to avoid the destructive short-trought foult of the DC bus, the pair of switches of the same branch must always be alternately controlled, so that the two swithces are never allowed to conduct simultanously. It result in eight possible combination, or inverter active states, which can be represented by a three-bit binary word, one for each phase, adopting the convention to indicate with 1 the shutdown of the top switch of the leg and with 0 the shutdown of the lower one.

The *PWM Generator* block present on this scheme generates this kind of binary word, in the form of six pulses, for the three-phase currier-based PWM self-commanded inverter. This one receive the pulses on the "*g*" input that command the commutation of the switch of the inverter. Finally, these last ones create the output three-phase voltage necessary to feed the electric motor. The *K* gain is necessary to obtain the three input voltages normalized, as requested for the proper operation of the *PWM Generator* block.

The pulses are generated by comparing a triangular carrier waveform to a reference modulating signal as shown in Figure 3.9.

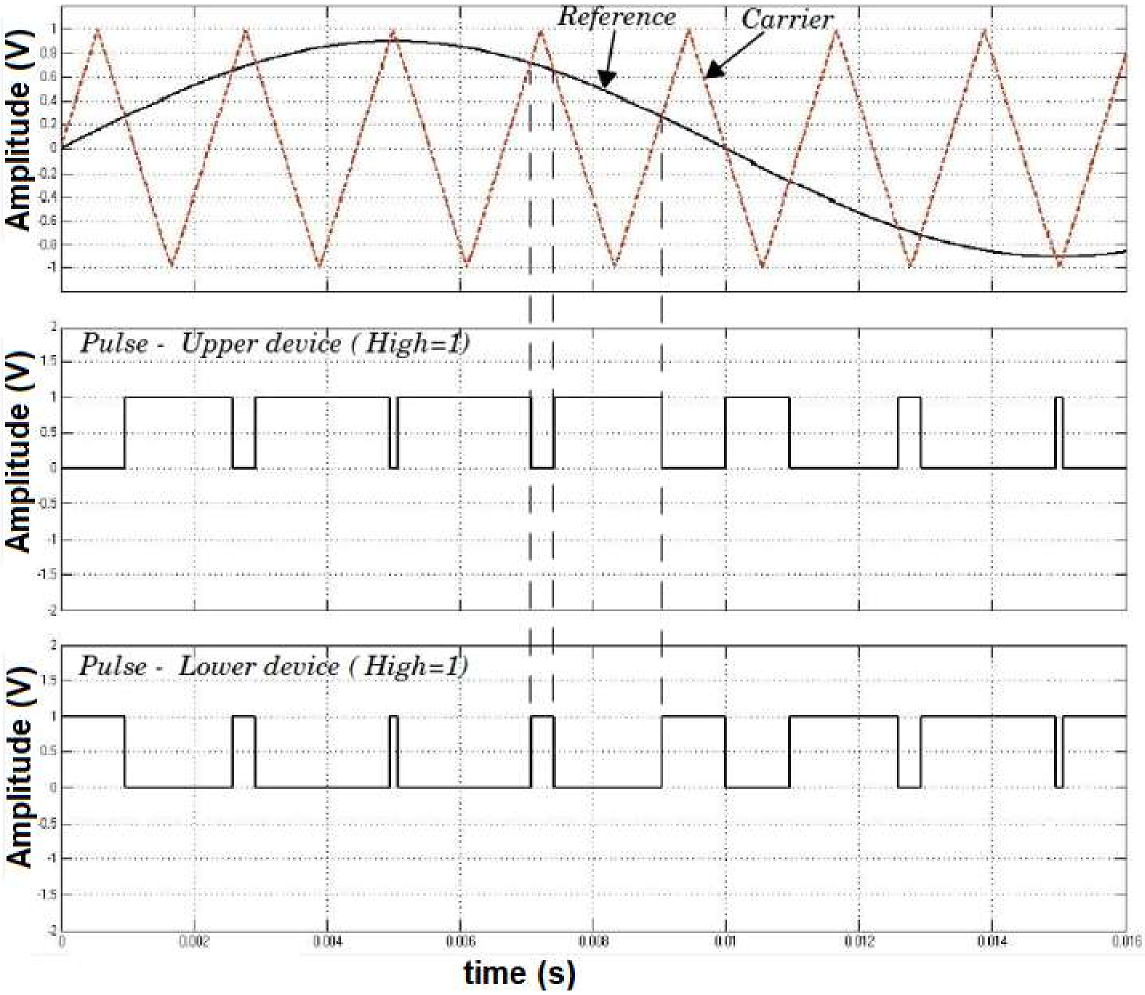

Figure 3.9 - PWM signals generation example.

When the modulating signal is greater than the carrier, the pulse for the upper device (for exemple the S1 of Figure 3.8) is high (1), that means swithch close, and the pulse for the lower one (for exemple S2) is low (0), that means switch open. Three reference signals are required to generate the pulses for a three-phase bridge. Obviously, the two pulses firing the two forced-commutated devices of a given arm bridge are complementary.

For this simulation is used a *Permanent Magnet Synchronous Machine* model, with in input the three-phase voltage form the inverter and the Mechanical Torque reference that is kept on the 0 Nm value. The outputs from the model are grouped in the *Data Bus Output*, and are: the three stator currents necessary for the current loop; the three Hall signals necessary for the frequency and position estimation; the electromagnetic torque; the mechanics frequency and position of the rotor. The last two parameters are necessary for the comparison and verification of the results obtained from the estimation, they are so converted in the electrical value by multiplications by the number of pole pairs.

Even if the model adopted does not represent the real machine used for the experimentations, it is used to verify the functioning of the whole detection scheme and the applicability of the MCCF-PLL. Another difference from the experimentations is that in the Simulink scheme is used a speed control when in fact is used only a current control, and the speed and the position estimated are not feedforward on the loop.

In the following, the position detection and the different controls are investigated.

3.5 Position Detection Block

In Figure 3.10 below is represented the POSITION DETECTION BLOCK of Figure 3.2.

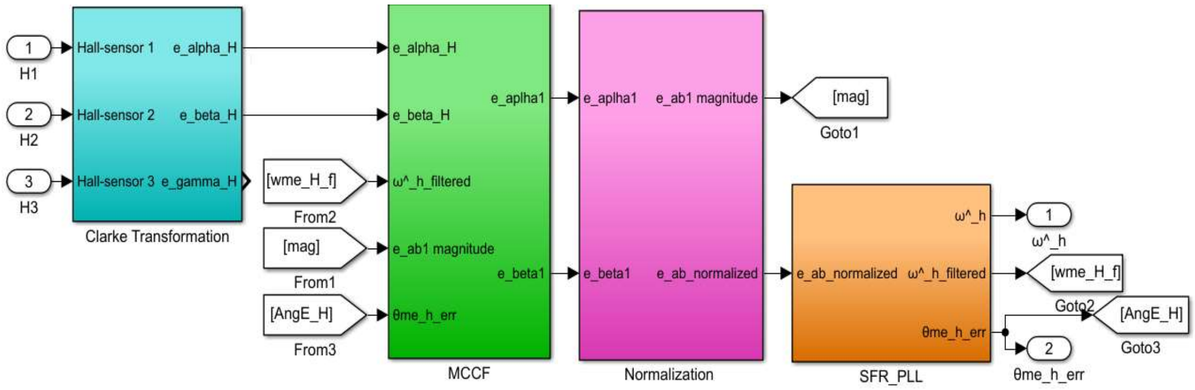

Figure 3.10 *- POSITION DETECTION BLOCK.*

To implement the current and speed controls the system needs some means of determining the rotor orientation/position/speed (relative to the stator coils), that are used on the controls feedback signal and on the various reference transformations. To obtain these information are used three Hall-effect sensors distributed uniformly each $120^{el.\circ}$. Each sector has a range of $60^{el.\circ}$ so the three sensors have a $60^{el.\circ}$ relative offset from each other. This divides a rotation into six phases. They output a high level for $180^{el.\circ}$ of an electrical rotation, and a low level for the other $180^{el.\circ}$. An example of the Hall-effect sensor signals is given in Figure 3.11.

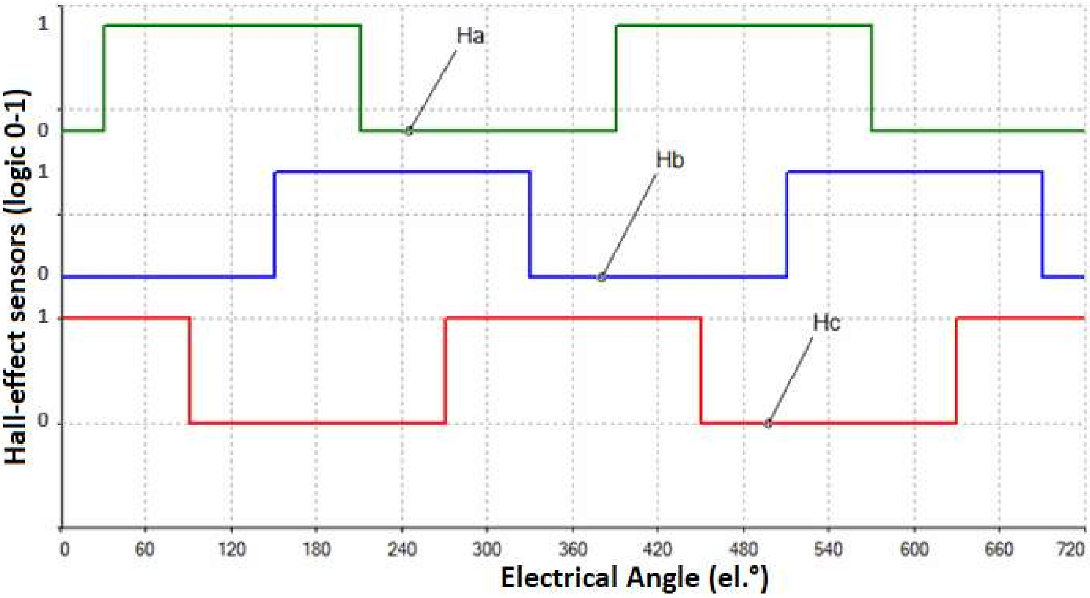

Figure 3.11 *- Hall-effect signals typical trend.*

The Hall-effect sensor combination change every $60^{el.\circ}$ of rotation. Given this, it takes six steps to complete an electrical cycle. However, one electrical cycle may not correspond to a complete mechanical revolution of the rotor, as in this case. The number of electrical cycles repeated to complete a mechanical rotation is determined by the rotor pole pairs, that are three. For each rotor pole pair, one electrical cycle is completed so, the number of electrical cycles/rotations equals the rotor pole pairs. This sequence of conducting pairs is essential to the production of a constant output torque.

The process of switching the current to flow through only two phases of the motor for every $60^{el.\circ}$ rotation of the rotor is called electronic commutation. As has been said, the motor is supplied with a three-phase inverter, and the switching actions are triggered by the use of signals from position sensors (the Hall-effect sensors) that are mounted at appropriate points around the stator, as will be shown in the next chapter with real images from the motor shell. Once the Hall switches are mounted at $120^{el.\circ}$intervals and aligned properly with the stator phase windings, they deliver digital pulses that can be decoded into the desired three-phase switching sequence called switching patterns.

The position and speed of the rotor from the Hall-effect sensors can be obtained in many different ways, as described in the §2.4, such as using position estimation algorithms like Zeroth-Order or First-Order Algorithm, using Vector Tracking Observers, or using an Hybrid Observer. As previously said, for this thesis work it has been chosen to use a Multiple-Complex Coefficient-Filter(MCCF)-based synchronization technique for an accurate phase/frequency estimation under unbalanced and/or distorted conditions. These are exactly the conditions that occur when trying to get the back-EMF from real Hall signals.

In order to get the desired information, firstly, the alpha and beta back-EMF components *e_alpha_H, e_beta_H* are extracted from the three Hall signals *H1,H2,H3* by means of the *Clarke Transformation* block. This block transforms the three-phase signal (abc for the formulas below) to a stationary reference frame signals (αβγ), or the inverse. The matrices used to this purpose are:

$$T_{abc\to\alpha\beta\gamma} = \frac{2}{3}\begin{bmatrix} 1 & -\frac{1}{2} & -\frac{1}{2} \\ 0 & \frac{\sqrt{3}}{2} & -\frac{\sqrt{3}}{2} \\ \frac{1}{2} & \frac{1}{2} & \frac{1}{2} \end{bmatrix} \tag{3.6}$$

$$T_{\alpha\beta\gamma\to abc} = \begin{bmatrix} 1 & 0 & 1 \\ -\frac{1}{2} & \frac{\sqrt{3}}{2} & 1 \\ -\frac{1}{2} & -\frac{\sqrt{3}}{2} & 1 \end{bmatrix} \tag{3.7}$$

The alpha and beta components are then utilized to extract the frequency and position of the machine by means of a modified SFR-PLL. The representation of the three Hall-effect signals and the two back-EMF components coming from the simulation is on the following figures.

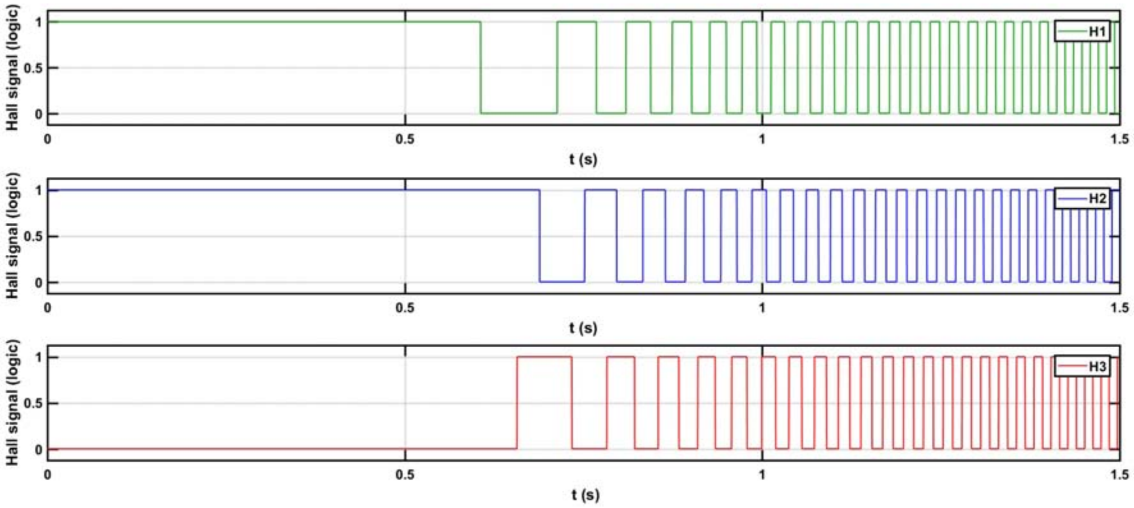

Figure 3.12 *- Hall-effect sensors signals.*

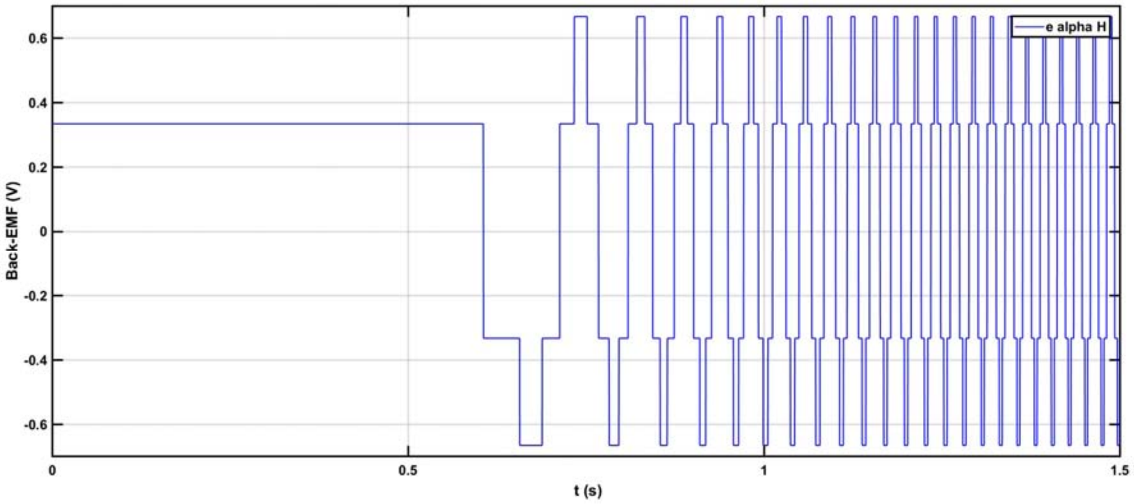

Figure 3.13 *- Alpha Back-EMF component.*

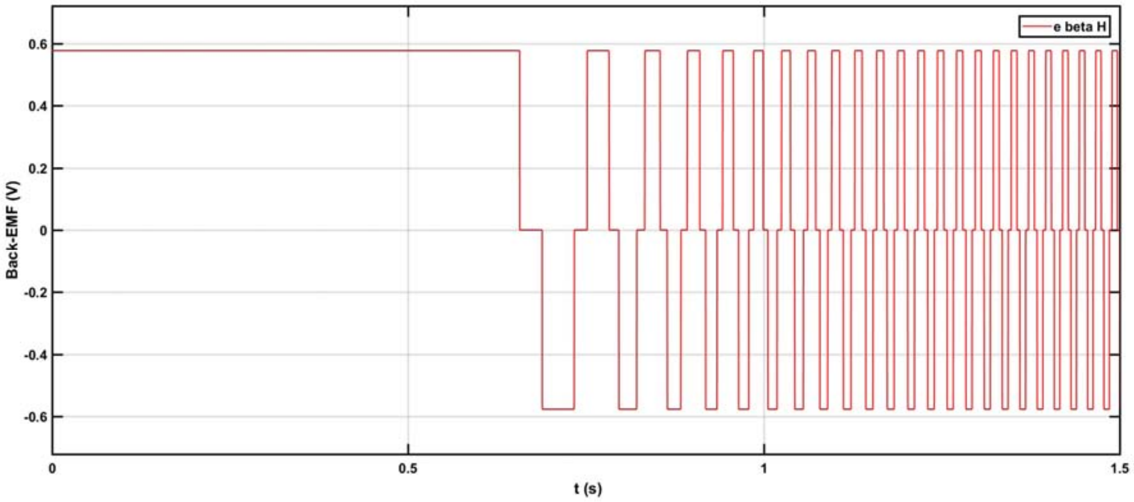

Figure 3.14 *- Beta Back-EMF component.*

The peak values of e_alpha_H and e_beta_H are respectively $0.6667\ V$ and $0.5774\ V$ Due to space problems the signals are represented only until $1.5\ s$. Can be observe that, as the speed increases, the signals period become thicker. On the next image the two signals are represented together.

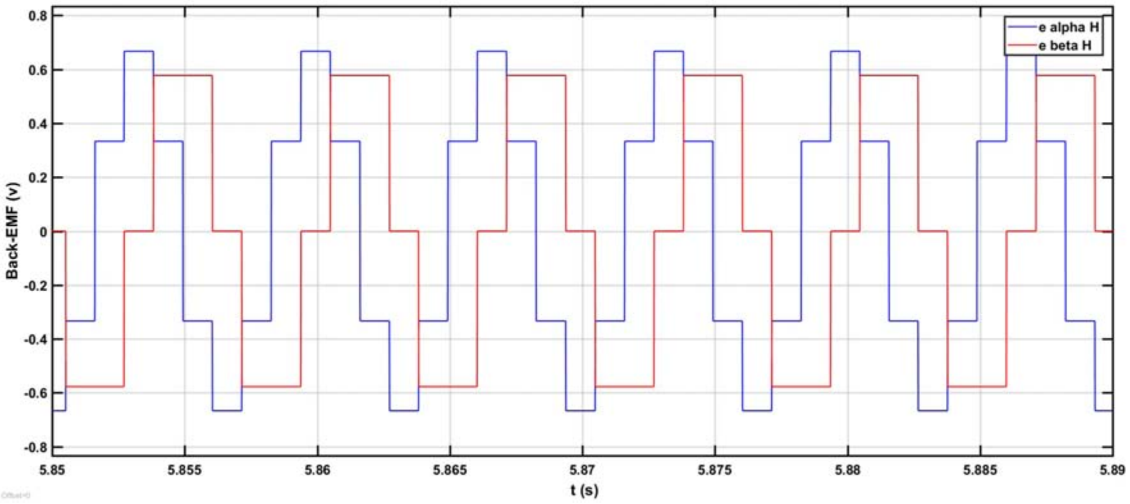

Figure 3.15 *- Alpha and beta Back-EMF components zoomed in.*

At this point, under ideal conditions, the classic SRF-PLL yield a fast and precise detection of the rotor speed and position. However, under adverse conditions, i.e., when the signal is unbalanced and/or harmonically distorted, it presents a degraded performance: high amplitude steady-state oscillations in the estimated phase/frequency arise. This problem can be mitigated by reducing the SRF-PLL bandwidth at the expense of the dynamic response, in fact a careful choice of the tuning parameters of the PI regulator has to be done, so that a good disturbance rejection is obtained. However, this may not be an acceptable solution in some applications like the electric motor drive, which need a good dynamic response. Different modified and advanced PLL has been found and investigated and the most of these, as the one here proposed, filter the harmonics and extract the fundamental positive sequence which is sent to the SFR-PLL.

Consequently, the stationary (*αβ*) coordinate voltages are sent to the *MCCF* block inputs. This block put in place the Multi-Complex Coefficient Filter described in the §2.5.2.

Besides the *αβ* inputs, are sent to the block also the estimated filtered speed from the SFR-PLL, *ω^_h_filtered*, that is necessary for the working of the filter, and two "check" inputs :*e_ab1 magnitude*, *θme_h_err* that will be considered on the last paragraph of this chapter, the Simulation Results paragraph.

This Multi-Complex Coefficient-Filter is designed to filter the alpha and beta back-EMF components, removing the -5th, 7th, -11th, 13th harmonics and so extracting the fundamental positive components *e_alpha1* and *e_beta1*. Third and its multiple harmonics are not selected for compensation, because the model does not emit triple order harmonics. However, the proposed compensation structure is capable of reducing 3^{rd} harmonics. In this simulation the rejection of the already cited harmonics is enough to obtain a sinusoidal fundamental positive sequence almost clear from noises. The block consists of five filters, like the number of harmonics that are taken in consideration. The fundamental filter is represented in Figure 3.16, and is the one that extracts and outputs the fundamental component *e_alpha1*, *e_beta1* used for the position and frequency estimation. The other four filters, shown in Figure 3.17, are the bandpass filters, these ones are necessary to eliminate the harmonics that affect the inputs of the block and so to obtain the clean fundamentals components. These last ones work in the same way of the fundamental filter, and they have the same design. As example, the Figure 3.18 takes a look inside the fifth harmonic filter.

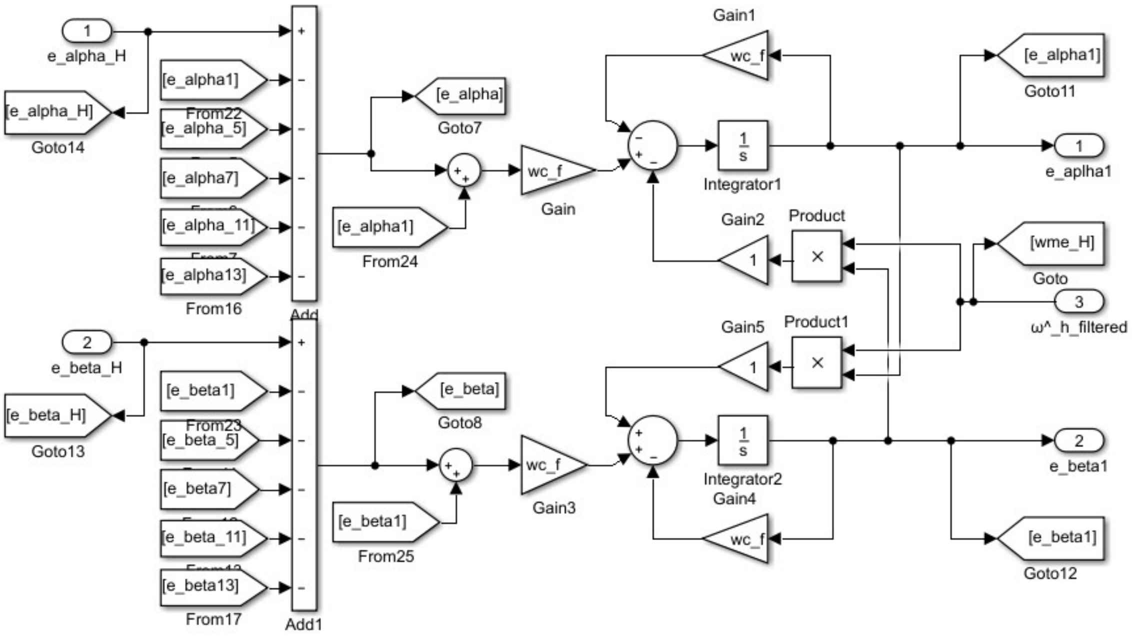

Figure 3.16 - *MCCF fundamental filter scheme.*

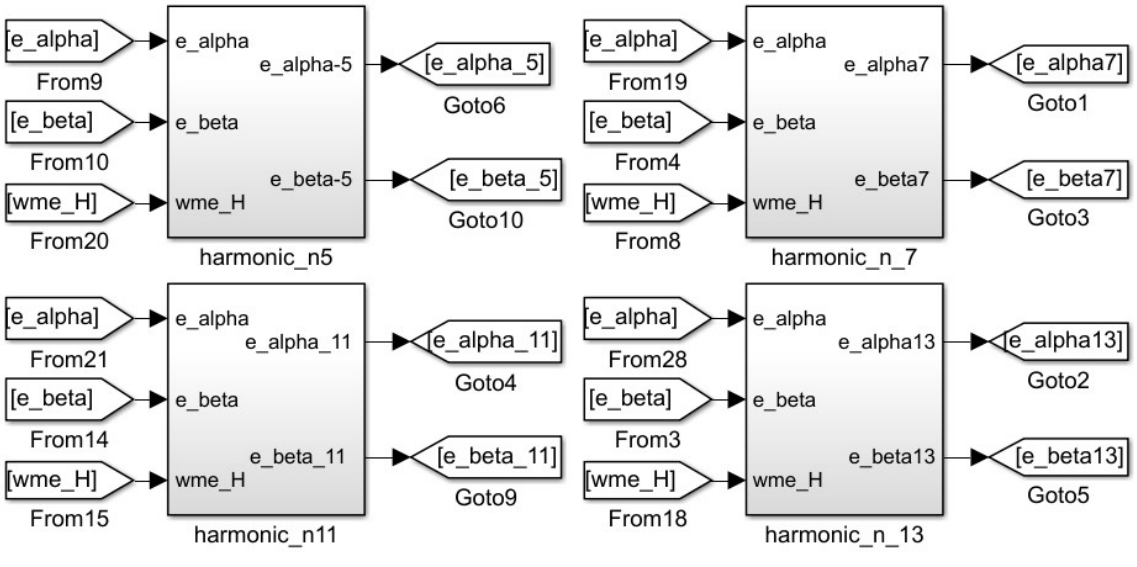

Figure 3.17 - *MCCF bandpass filter blocks.*

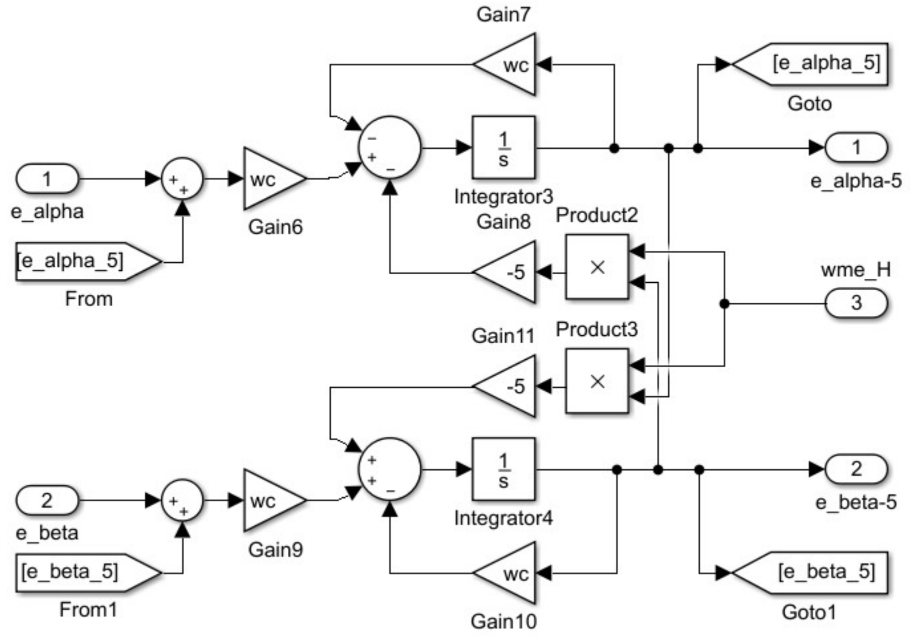

Figure 3.18 *- Harmonic bandpass filter representation.*

The cut-off frequency value used for fundamental filter block is:

$$\omega_{c\_f} = 100 * 2\pi\, rad/s \tag{3.8}$$

and the cut-off frequency for the bandpass filters is:

$$\omega_c = 2.5 * 2\pi\, rad/s \tag{3.9}$$

After the filtering process, the newly obtained signal *e_aplha1, e_beta1* are normalized so that the speed extracted by the SFR-PLL does not depends on the amplitude of these signals. The *Normalization* block is shown in Figure 3.19, and consists on dividing the two signals by the magnitude of the complex signal that they form.

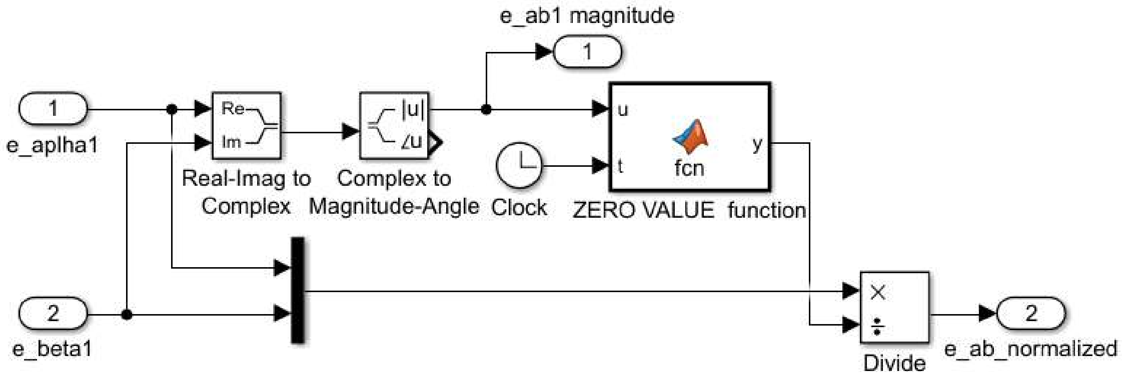

Figure 3.19 ***-*** *Normalization block scheme.*

The *ZERO VALUE* function is a function that avoid the division zero by zero at the starting time of the simulation. It use the floating-point relative accuracy (eps) MATLAB function, allocating the value *2.2204e-16* to the *e_ab1 magnitude* signal at the zero time of the simulation, when the back-EMF has null value. This is the lowest value greater than zero for the program. In this process is extracted the magnitude of the fundamental component of the back-EMF signal coming form the Hall signals and so filtered in the *MCCF* block. This data is used, with the angle information extracted on the SFR-PLL, to verify the correctness of the MCC filtering process as will be shown later on §3.9

The last inner block of the *POSITION DETECTION* block is the SFR-PLL one, represented in the Figure 3.20 below.

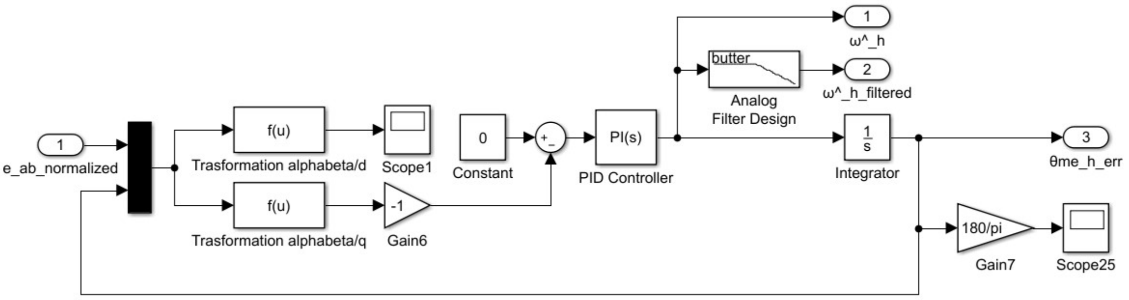

Figure 3.20 *- SFR-PLL scheme.*

In the PLL arrive the normalized fundamental components of the back-EMF, and the next transform matrix is used to pass from the stationary reference frame to the rotor speed rotating reference frame.

$$T_{\alpha\beta\gamma\rightarrow dq0} = \begin{bmatrix} \cos\left(\theta_{me\_err}^{h}\right) & \sin\left(\theta_{me\_err}^{h}\right) & 0 \\ -\sin\left(\theta_{me\_err}^{h}\right) & \cos\left(\theta_{me\_err}^{h}\right) & 0 \\ 0 & 0 & 1 \end{bmatrix} \tag{3.10}$$

This matrix is given by the multiplication of the Clarke $T_{\alpha\beta\gamma\rightarrow abc}$ matrix and the Park $T_{abc\rightarrow dq0}$ matrix and it is implemented on the two *f(u)* blocks. Must be noticed that in this case is used the pure estimated electrical angle of the machine $\theta_{me\_err}^{h}$, and not the combination of θ_{me}^{h} and θ_{me}^{r}, as with the previous transformations in the *SPEED* and *CURRETN BLOCK*.

Anyway, only the q component of the filtered signals is taken in consideration. Using a feedback loop, the angular position of the DQZ reference frame, that is the electrical angle of the machine $\theta_{me\_err}^{h}$ researched, is regulated in such a way that the q-axis component becomes zero. The gain -1 present on scheme is necessary to adjust the references. The proportional-integral (PI) controller is used as the loop filter (LF) and on is output is obtained the motor speed $\widehat{\omega}_h$. Afterword, the speed is integrated with an integrator to get the angular position of the rotor, that is named $\theta_{me\_err}^{h}$ because , as will be explained in the §3.8, is the angle of the machine affected by an phase shift error. The speed, before to be sent back to the *MCCF* block, is filtered by an eighth order Butterworth *Low-Pass Filter* with passband edge frequency of *125.6 rad/sec* to avoid all the undesired oscillation due to the high frequency noise generate by the control.

Firstly the PI of the SRF PLL was tuned with SISOTOOL of MATLAB, trying to obtain a bandwidth of $100\ Hz$ (between the bandwidth of the speed and current control) and then it was adjusted manually to have the most clean position estimation possible. This PI is set in a parallel configuration $Kp + Ki/s$.

The values of the PI controller in the PLL are:

$K_p = 300$ and $K_i = 30000.$

On the following paragraphs, are described the Current and Speed regulators that are on the *SPPED* ad *CURRENT BLOCK*, and the *PHASE SHIFT COMPENSATION BLOCK* present on Figure 3.2.

3.6 Current Regulators

The *d/q Current Regulator*s blocks, present on the *SPEED BLOCK*, are the ones that give as output the voltages references necessary to control the machine. They are designed before the *Speed Control* even if they are schematically consequent to it. Their representation is on the Figure 3.21.

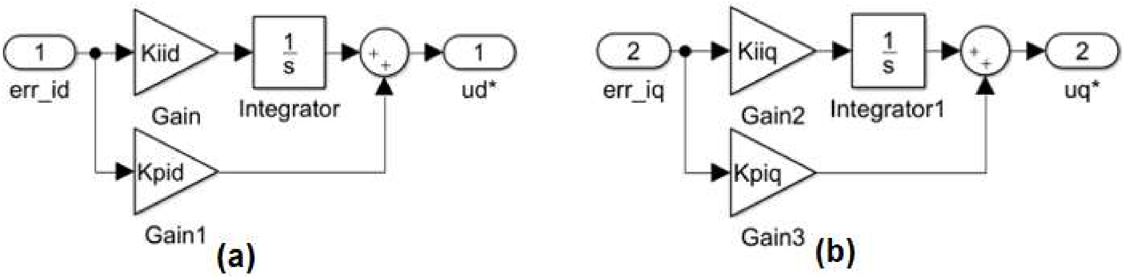

Figure 3.21 *- (a) d Current Regulator scheme, (b) q Current Regulator scheme.*

The design of the controllers is complicated by the fact that the two current rings are not independent of each other, but they influence each other due to cross coupling present between the *d*- and *q*-axes of the motor. If the time constant of the inverter, $\tau_G = \frac{T_S}{2}$ where $T_S = \frac{1}{fc}$, is small compared to other time constants in the system (as usually happens, and as it is assumed in this case), is possible to eliminate the mutual coupling between the *d*- and *q*-axes inserting on the output of the current regulators a cross coupling equal and opposite. In the case of these simulations such interference between the axes is not perceptible, therefore the decoupling could be omitted.

The i_q current (torque current) controller calculates voltage u_q to feed the same amount of torque current as the torque current command i_q^*, which is obtained by the speed controller. The i_d current (excitation current) controller calculates voltage u_d^* to feed the same amount of excitation current as the excitation current command i_d^*, that in this case it is set equal to 0. For these current controls are used two PI controllers (one for the d-axis and one for the q-axis). The general block diagram used for the calculation of the gains K_{Pi} and K_{Ii} of the controllers is the following in Figure 3.22, that comes from the scheme of the drive in Figure 3.1 remembering that the inverter block G_C, between the current regulator block and the electric system block, has been neglected.

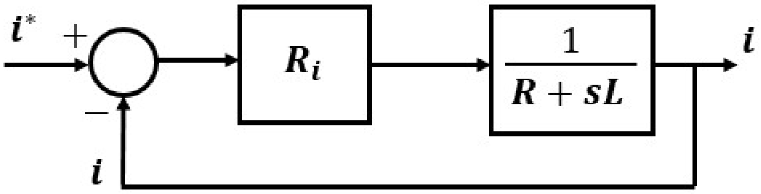

Figure 3.22 *- Current control block diagram.*

The first block is the PI regulator, and the second one is the representation of the electric system of the motor obtained from the electrical equations of the machine in the chapter 1. The bandwidth of the PI regulator is set at $f_{b\omega i} = 500\ Hz$, and from this the K_{Pi} and K_{Ii} have been calculated with the following equations.

$$R_i = K_{Pi} + \frac{K_{Ii}}{s} = K_{Ii}\frac{1 + s\tau_{Ri}}{s} \tag{3.11}$$

Where R_i is the transfer function of the PI current regulator and $\tau_{Ri} = \frac{K_{Pi}}{K_{Ii}}$ is its time constant.

$$G_E = \frac{1}{sL_s + R_s} = \frac{1}{R_s(1 + s\tau_E)} \tag{3.12}$$

Where G_E is the transfer function of the electric system, $\tau_E = \frac{L_s}{R_s}$ is its time constant and L_s is the armature inductance and R_s the stator phase resistance. This data are obtained from the Simulink model of the PMSM. L_s should be differentiated among L_d and L_q, that are respectively the d- and q-axis inductance of the machine , but in this study they are considered equal even if in practice is used an IPM motor and not a SPM motor.

The multiplication between the two transfer function gives the overall transfer function

$$G_{TOTi} = \frac{K_{Ii}(1 + s\tau_{Ri})}{R_s(1 + s\tau_E)s} \tag{3.13}$$

To calculate the current regulator parameters one way is to pass to the frequency domain and to impose that at the desired crossing frequency the amplitude of the overall transfer function gain is equal to the unity (corresponding to the null value in dB):

$$1 = \frac{K_{Ii}\sqrt{1 + (\nu_{\omega i}\tau_{Ri})^2}}{R_s \nu_{\omega i}\sqrt{1 + (\nu_{\omega i}\tau_E)^2}} \tag{3.14}$$

Where $\nu_{\omega i} = 2\pi f_{b\omega i} = 3141.6\, rad/s$.

Now, imposing the zero-pole cancellation between the current regulator and the electrical system, or rather, equating the time constant of the PI regulator with the time constant of the electrical system, the equation (3.14) is simplified by the cancellation of the two term under the square root. So, is possible to obtain the parameters as following:

$$K_{Ii} = 2\pi f_{b\omega i} R_s \tag{3.15}$$

$$K_{Pi} = 2\pi f_{b\omega i} R_s \tau_{Ri} \tag{3.16}$$

Since L_d and L_q are assumed equal, the proportional and integrator gains assume the same values for both the *d*- and *q*-axes, these values are:

$K_{Pi} = 1.2409$ and $K_{Ii} = 152.3672$.

This values are obtained assuming $R_s = 0.0485\, Ohm$, and $L_s = 0.000395\, H$, data coming from the Simulink model of the adopted machine, and giving as electric system time constant:

$$\tau_E = \frac{L_s}{R_s} = 0.008144 > 0.00005 = \frac{1}{2fc} = \frac{T_s}{2} = \tau_G \tag{3.17}$$

Corroborating the hypothesis above.

The Figures 3.23 and 3.24 represented the Bode Diagram and the Root Locus of this controller.

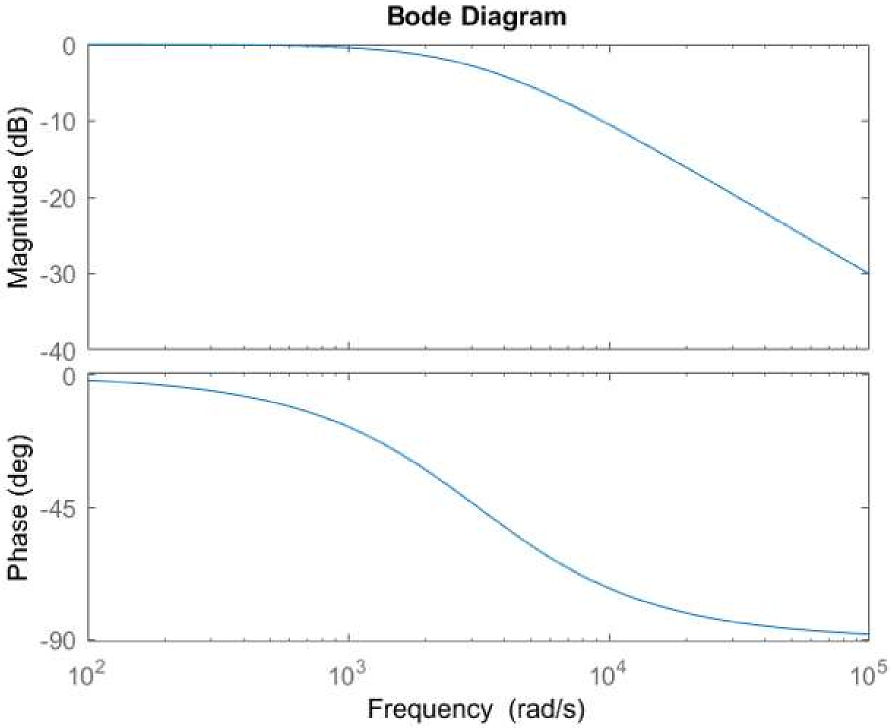

Figure 3.23 *- Current Regulator Bode diagram.*

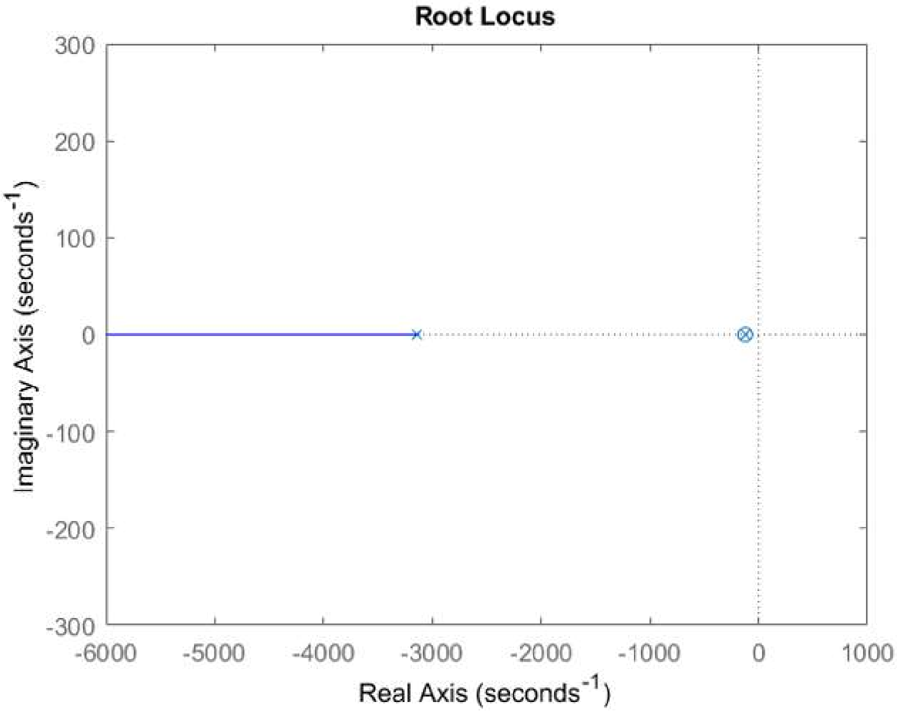

Figure 3.24 *- Current Regulator Root Locus diagram.*

3.7 Speed Regulator

This controller operates to diminish the difference between the speed command ω_r and the estimated speed $\widehat{\omega}$ from the Hall-effect sensors. In other words, it operates to match the speed command to the motor speed. In order to match the speeds, the motor load at a particular timing is calculated from the difference between the speed command and the estimated speed, and the required torque for the timing (torque current command i_q^*) is transmitted to the i_q current (torque current) controller. Its scheme is shown on Figure 3.25.

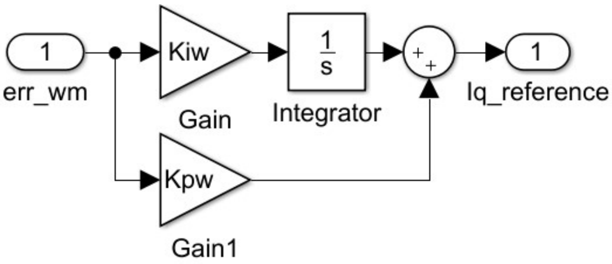

Figure 3.25 *- Speed Regulator scheme.*

The parameters $K_{P\omega}$ and $K_{I\omega}$ have been chosen in order to provide to the PI speed regulator a slower dynamic then the PI current control. Since this two control blocks are placed consecutively, a too fast speed control can afflict the dynamic of the current control that must been seen in a steady state, so it is chosen a bandwidth of:

$$f_{b\omega\omega} = \frac{f\_b\omega i}{10} - 20 = 30Hz \tag{3.18}$$

The block diagram that should be used to calculate these two parameters is represented in Figure 3.26, but is used a simplification illustrated in Figure 3.27, this because of the fast response of the current control and the small value of the inverter time constant, that it is not considered also on the scheme in Figure 3.22 in the §3.6.

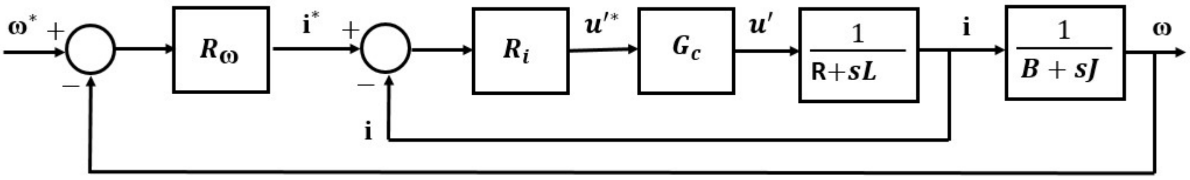

Figure 3.26 *- Speed control complete block diagram.*

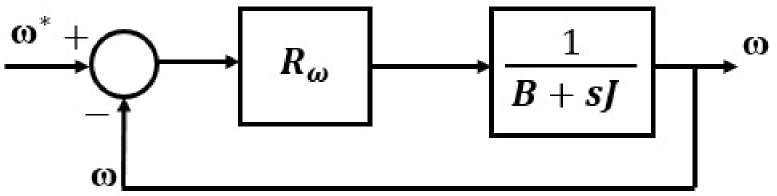

Figure 3.27 *- Speed control simplified block diagram.*

To calculate the values $K_{P\omega}$ and $K_{I\omega}$ is used the same procedure used for the current controller.

$$R_\omega = K_{P\omega} + \frac{K_{I\omega}}{s} = K_{I\omega}\frac{1+s\tau_{R\omega}}{s} \tag{3.19}$$

Where R_ω is the transfer function of the PI current regulator and $\tau_{R\omega} = \frac{K_{P\omega}}{K_{I\omega}}$ is its time constant.

$$G_M = \frac{1}{sJ+B} = \frac{1}{B(1+s\tau_M)} \tag{3.20}$$

Where G_M is the transfer function of the mechanical system, that is the motor, and $\tau_M = \frac{J}{B}$ is its time constant. J is the inertia of the machine, and B is the viscous damping given from the Simulink model. The transfer function of the whole system is:

$$G_{TOT\omega} = \frac{K_{I\omega}(1+s\tau_{R\omega})}{B(1+s\tau_M)s} \tag{3.21}$$

Imposing the amplitude of (3.20) equal to the unity is obtain the following equation:

$$1 = \frac{K_{I\omega}\sqrt{1+(\nu_{\omega\omega}\tau_{R\omega})^2}}{f_{b\omega\omega}\sqrt{1+(\nu_{\omega\omega}\tau_M)^2}} \tag{3.22}$$

Where $\nu_{\omega\omega} = 2\pi f_{b\omega\omega} = 188.4956\, rad/s$.

Also in this occasion is impose the zero-pole cancellation between the speed regulator and the mechanical system, and so the equality between the time constant of PI regulator and the time constant of the mechanical system, the equation (3.21) is simplified by the cancellation of the two term under the square root. So, is possible to obtain:

$$K_{I\omega} = 2\pi f_{b\omega\omega}B \tag{3.23}$$

$$K_{P\omega} = 2\pi f_{b\omega\omega}B \tag{3.24}$$

These values are:

$K_{P\omega} = 0.5089$ and $K_{I\omega} = 0.0928$.

This values are obtained assuming $B = 0.0027\, Kg * m^2$, and $J = 0.0004924\, N * m * s$, data coming from the Simulink model of the adopted machine, that lead to a mechanical time constant of:

$$\tau_M = \frac{J}{B} = \ 0.1824 \ > 0.008144 = \frac{L_s}{R_s} = \tau_E \tag{3.25}$$

In Figures 3.28 and 3.29 are represented the Bode Diagram and the Root Locus of this controller.

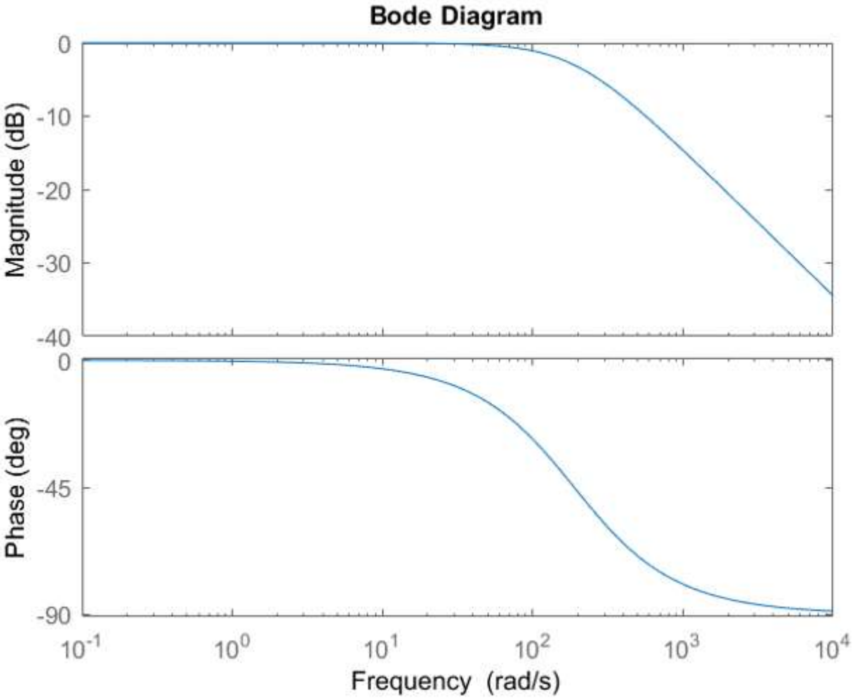

Figure 3.28 *- Speed Regulator Bode diagram.*

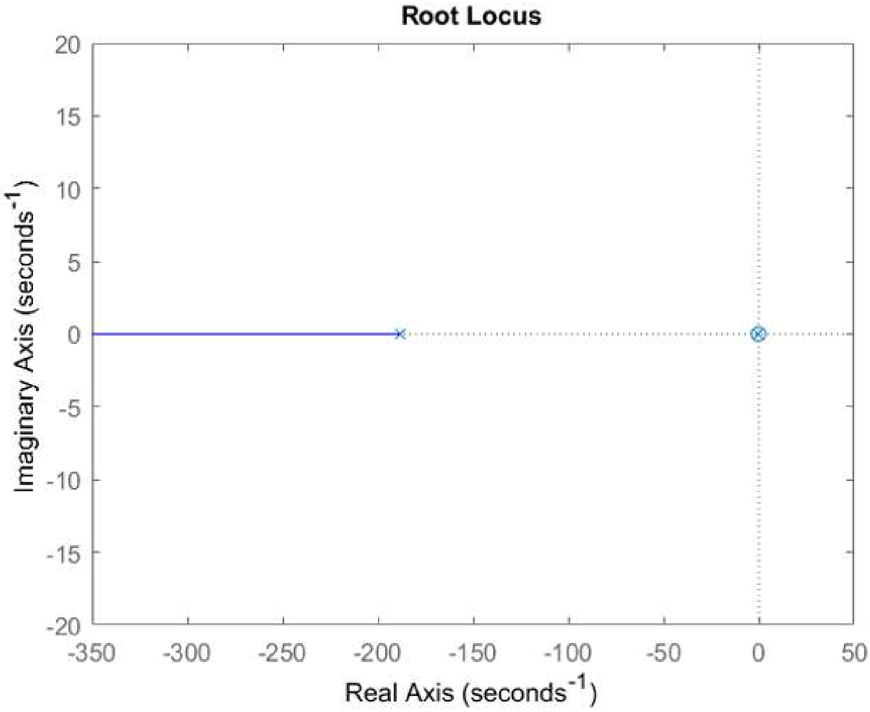

Figure 3.29 *- Speed Regulator Rot Locus diagram.*

3.8 Phase Shift Compensation Block

The *Phase Shift Compensation* block, represented in Figure 3.30, is necessary to remove the phase shift present on the estimated angle.

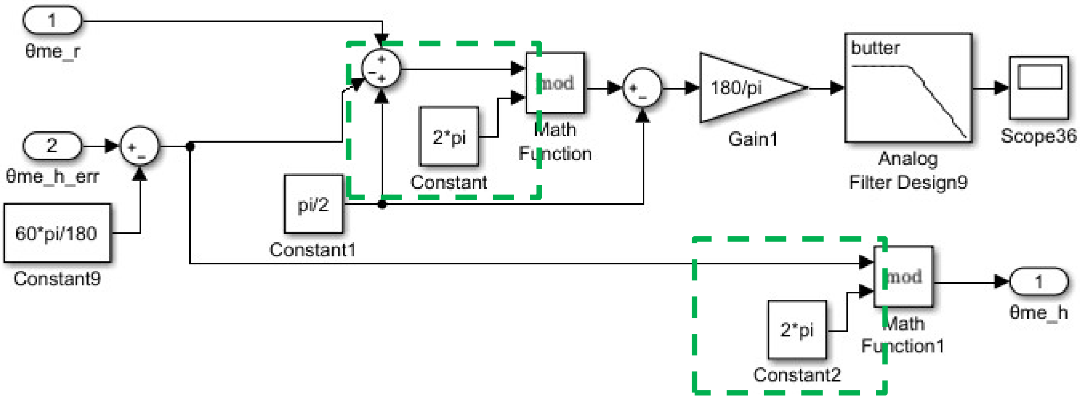

Figure 3.30 *- Phase Shift Compensation block.*

In fact, the filtering stages, that the back-EMF components undergo to pull out the frequency and position information of the machine, introduce a delay on the angle estimated by the MCCF-PLL. For this reason is named $\theta_{me\_err}^{h}$ to underline that is affected by error.

This block compares the machine angle coming from the Simulink model, θ_{me}^{r}, and the estimated one $\theta_{me\_err}^{h}$. It subtracts the second to the first, using a $\frac{\pi}{2}$ constant, and transforms this difference from electrical radiant to electrical degrees through the *Gain1*, and then filters to remove the high frequency noise. To reduce the phase shift a constant, *Costant9*, is subtracted from the $\theta_{me\_err}^{h}$, and a good correction is obtained once the signal shown by the *Scope36* gives an acceptable error angle, so amongst $\pm 10^{el.\circ}$. After different tests, the correct constant value have been found at $60^{el.\circ}$, that are

$$\frac{60*\pi}{180} = 1.0472\ el.rad.$$

The operations bordered by the green dashed line are necessary to remodel the angles in the range $0 \div 2\pi\ el.rad$, that otherwise, they will grow continuously from zero to over 2π. The signal displayed by the Scope36, is shown in Figure 3.31.

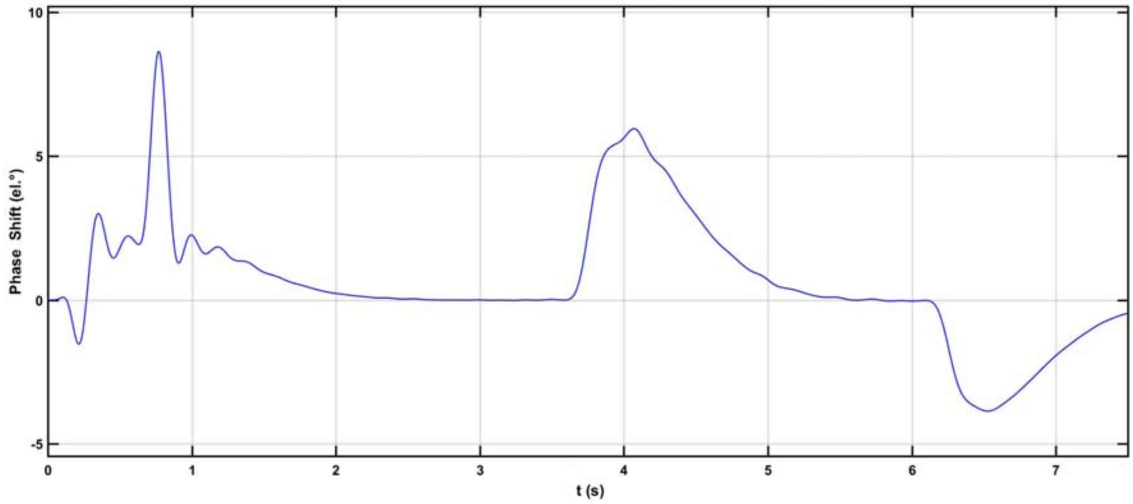

***Figure 3.31**- Estimated angle phase shift.*

As can be seen, the difference between θ_{me}^{r} and θ_{me}^{h} after the compensation is always included between the thresholds set. The variations from the ideal *0* value come at the speed profile variations, and on the first moments where the estimated angle differs from the real one of the Simulink machine model owing to the very low speed.

3.9 Simulations results

In this chapter are shown the results of the Simulink simulation, that are the principal signals that describe the correct working of the subject of this thesis work: the frequency/position estimation by means of the Multi-Complex Coefficient-Fiter Phase-Looked Loop feeded with digital Hall signals. The signals here displayed are all coming from the *Scope* blocks, properly located in the whole model described above. However, they are not represented on the overlying blocks images due to clarity of image.

For all the simulations a sample time of $T = 10^{-5}\ s$ has been used, and the period of the simulation was set to 7.5 s. The solver used was the ode5 (Dormand-Prince) in Fixed-step type. The two back-EMF signals in input of the MCCF have been already represented on the previous Figure 3.143and 3.14. Are now represented the fundamental positive components extracted by the MCC-Filter, so the same signals but deprived of the -5th, 7th, -11th, 13th harmonics.

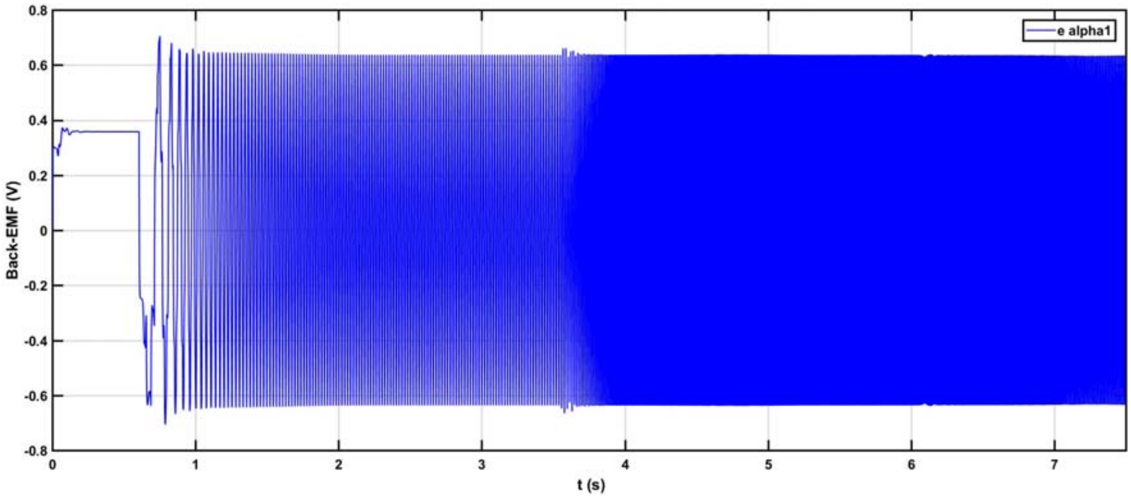

Figure 3.32 *- Alpha fundamental positive component in output of the MCCF block.*

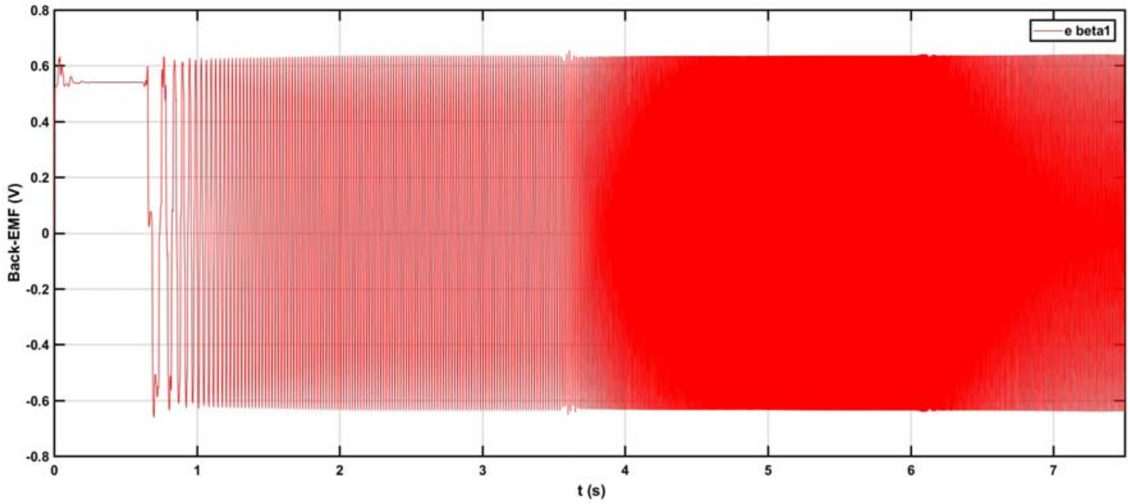

Figure 3.33 *- Beta fundamental positive component in output of the MCCF block.*

As have been already said, with the increasing of the machine speed the period of the signals become shorter. On the following Figure 3.34 and 3.35 are represented again these two signals but zoomed, to better show their waveform.

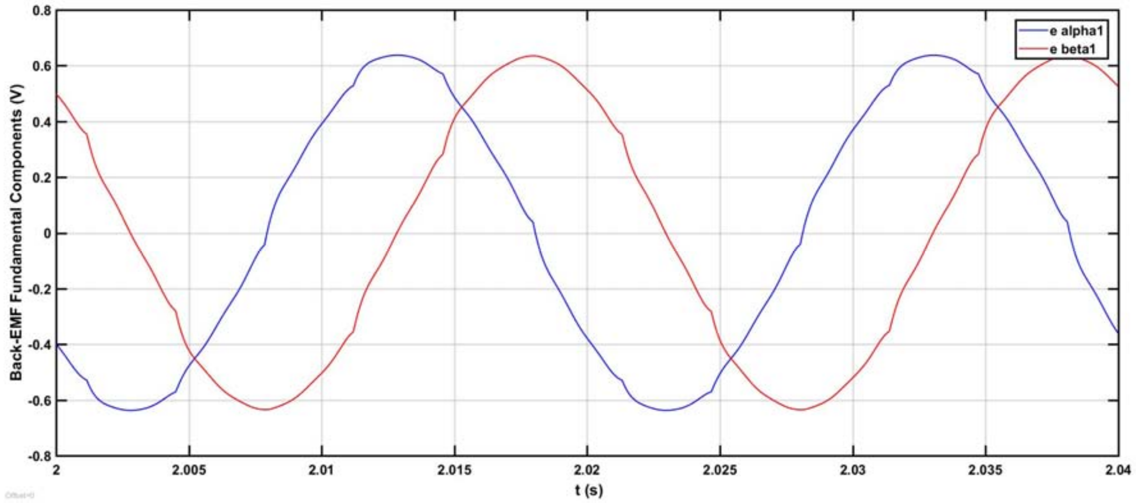

Figure 3.34 *- Fundamental positive component in output of the MCCF block, zoomed in the time interval: 2÷2.04 s.*

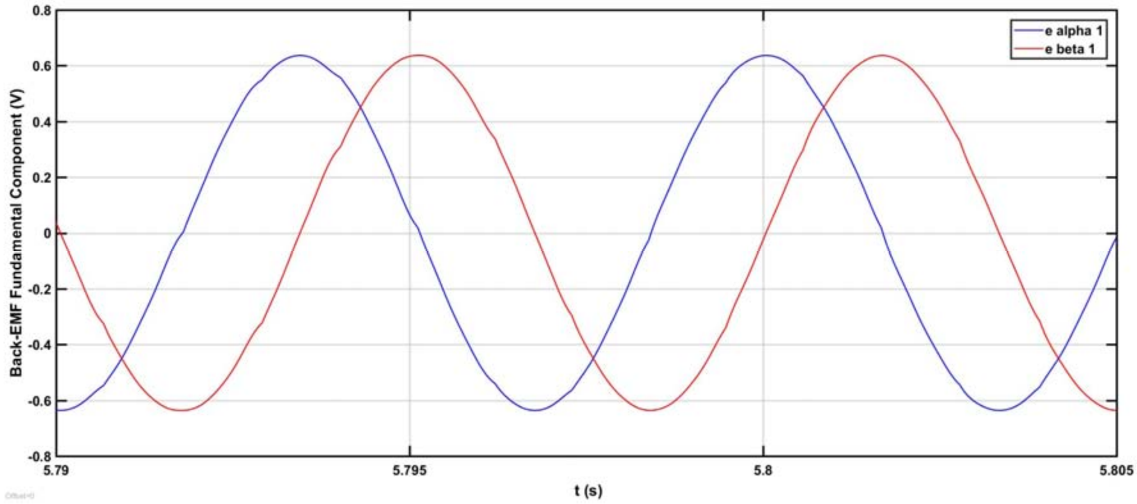

Figure 3.35 *- Fundamental positive component in output of the MCCF block, zoomed in the time interval: 5.79÷5.805s.*

The Figure 3.34 is taken in a period of time when the speed is around $314\ el.rad/s$ and shows that the signals extracted are very close to the sinusoidal shape, but due to the not high speed the influence of others harmonics is bigger than in the Figure 3.35, taken when the speed is $942\ el.rad/s$. This is due to the discrete absolute-position information provided by the Hall-effect sensors with only $\pm 30^{el.\circ}$ resolution that cause a low resolution rotor angle feedback which affects the back-EMF estimation mainly at low speed.

The peak values of both the signals are close to $0.636\ V$. These values are almost constant after the first $2\ s$ because of the reason just cited. Another variations of the peak values during the simulation are due of the reference speed steps, in fact they occur at the time of the speed change. This happens because the SFR-PLL has not an infinity high dynamic response, so it takes some time to follow the change of the speed reference. Anyway, as the images show, it has been reached a very good dynamic response on the *POSITION DETECTION BLOCK* that allows to consider them as good results.

To better prove the correct working of the *MCCF* block, six signals are compered on the following scheme, that is inside the *MCCF* block and use the already mentioned *check* signals on the §3.5.

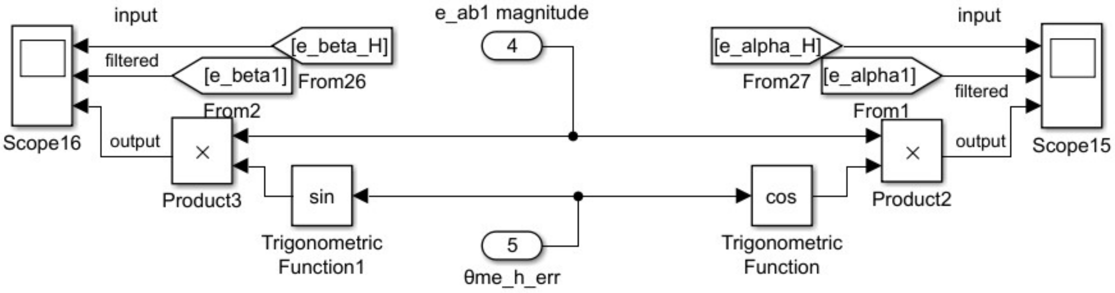

Figure 3.36 *- Scheme utilized to compare the phase and amplitude of the signals in input of the MCCF block, the signals obtained from the MCC filtering stage and the check signals.*

On the two scopes are visualized three signals, called *input*, *filtered*, *output*. On the right side of the scheme in Figure 3.36 these three signals correspond, respectively, to:

- *e_alpha_H* that is the alpha component of the back-EMF coming from the Hall-effect signals;
- *e_alpha_1*, that is the fundamental component of the previous one, obtained by filtration process in the MCC-Filter;
- the *check* signals, that are the mathematical reconstruction of *e_alpha_1*, obtained with the magnitude of the fundamental αβ signal calculated on the *Normalization* block, *e_ab1 magnitude*, and the estimated angle $\theta_{me\_err}^{h}$.

On the left side of Figure 3.36, these three signals correspond to the equivalent beta component. The two groups of signals are represented in Figure 3.37 and 3.39, and enlarged in Figure 3.38 and 3.40.

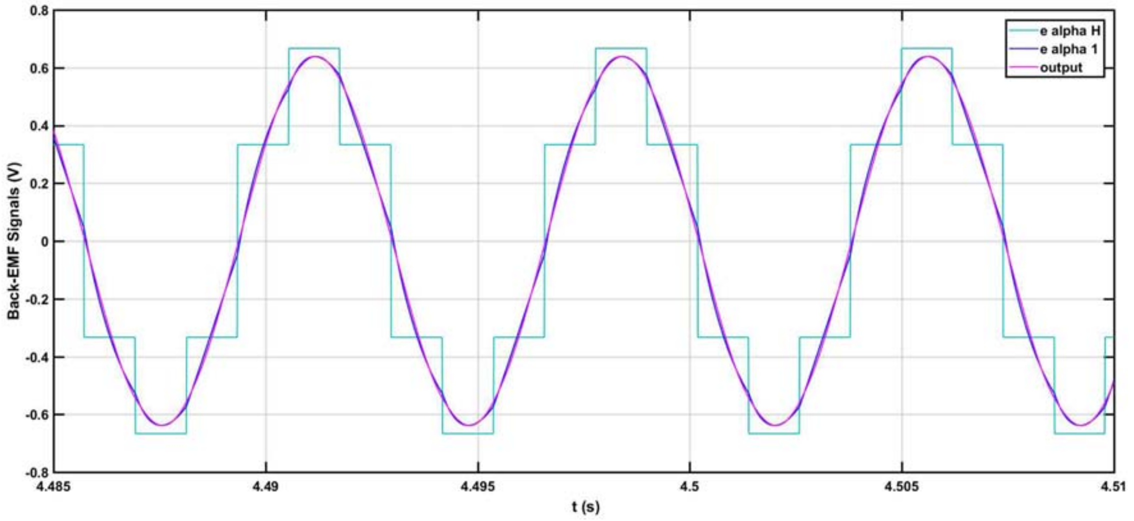

Figure 3.37 *- Alpha signals comparison.*

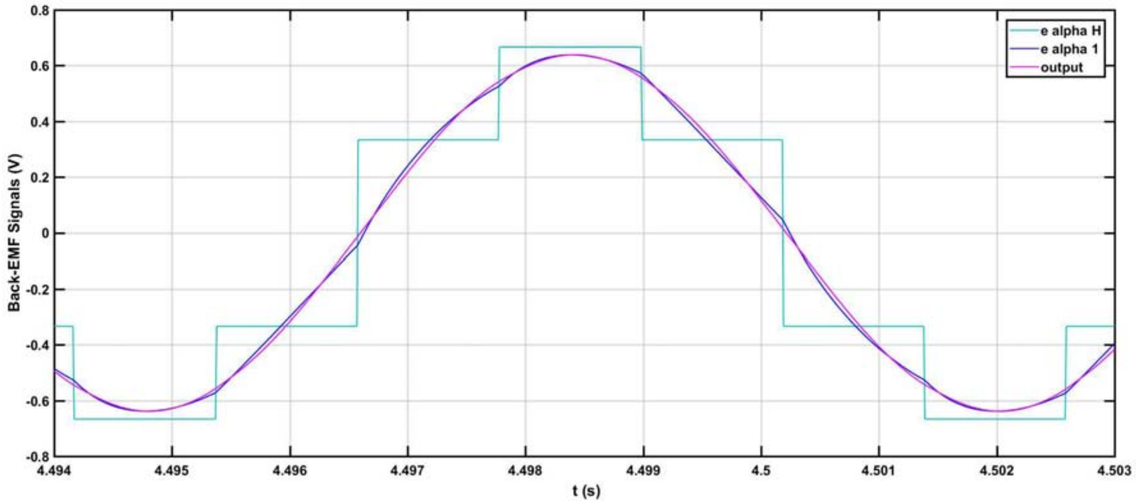

Figure 3.38 *- Compared signals of Figure 3.37 enlarged in time.*

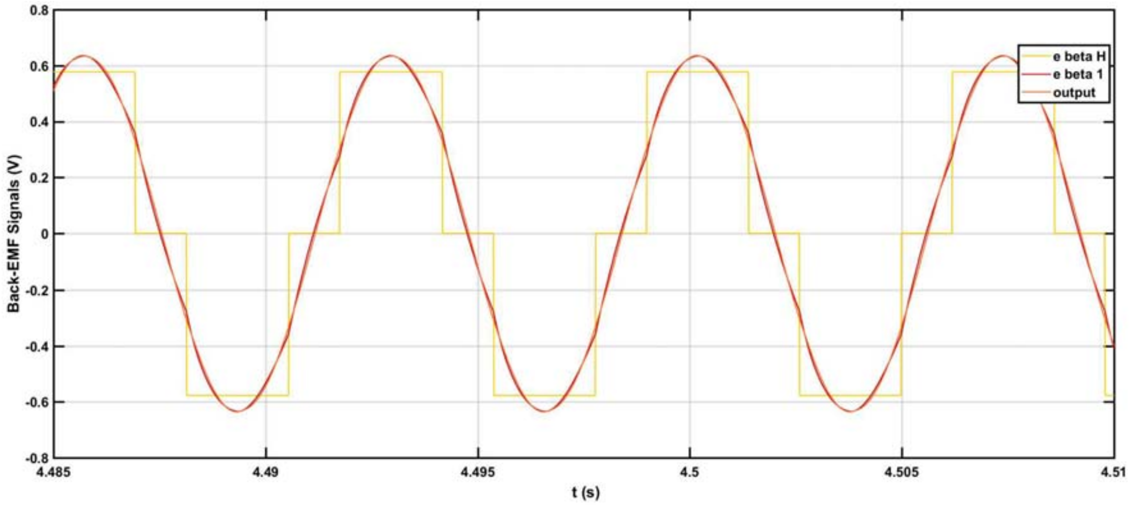

Figure 3.39 *- Beta signals comparison.*

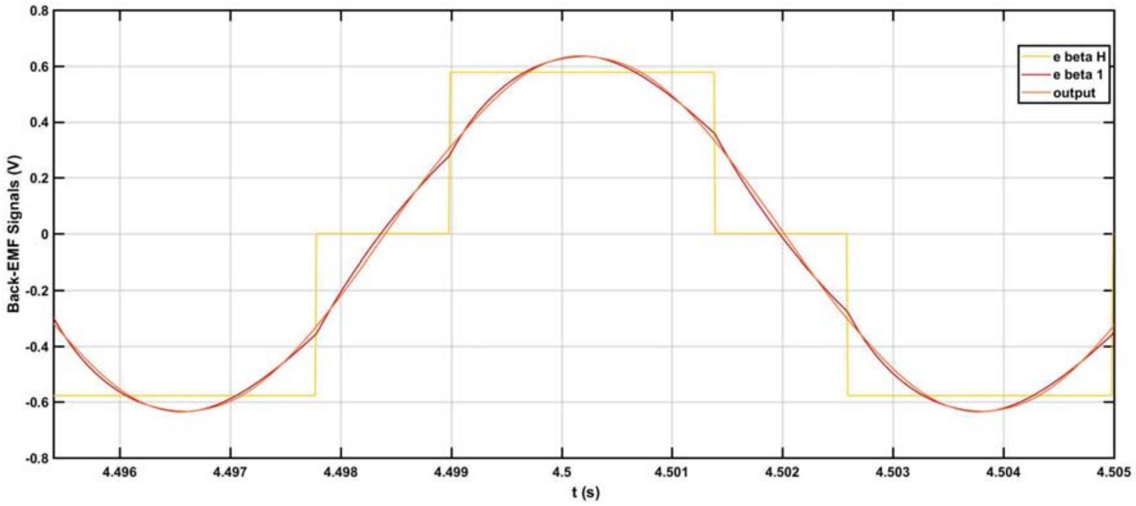

Figure 3.40 *- Compared signals of Figure 3.39 enlarged in time.*

Can be seen, especially in Figure 3.38 and 3.40, that the output signal is almost coincident with the fundamental one, without phase shift error between them and the back-EMF inputs. This means that the *MCCF* block is not introducing delay on the signals.

Now that the correctness of the signals elaborated in the Multi-Complex Coefficient-Filter is verified, the two fundamental components of the back-EMF signal given by the Hall-effect sensors, *e_alpha_1/e_beta_1*, are normalized and sent to the SFR-PLL. Here they are converted in the *DQZ* reference frame and only the *q* component is used in the PLL to obtain the frequency and the position angle of the machine. All these passages have been already described in §3.5, and here are shown the frequency and the position angle achieved with the Simulink scheme developed and described in this work.

The Figure 3.41 display the frequency of the machine given by the Simulink model, ω_{me}^{r}, and the one extracted by the *POSITION DETECTION BLOC* , $\widehat{\omega}_h$, in the image named ω_{me}^{h} .

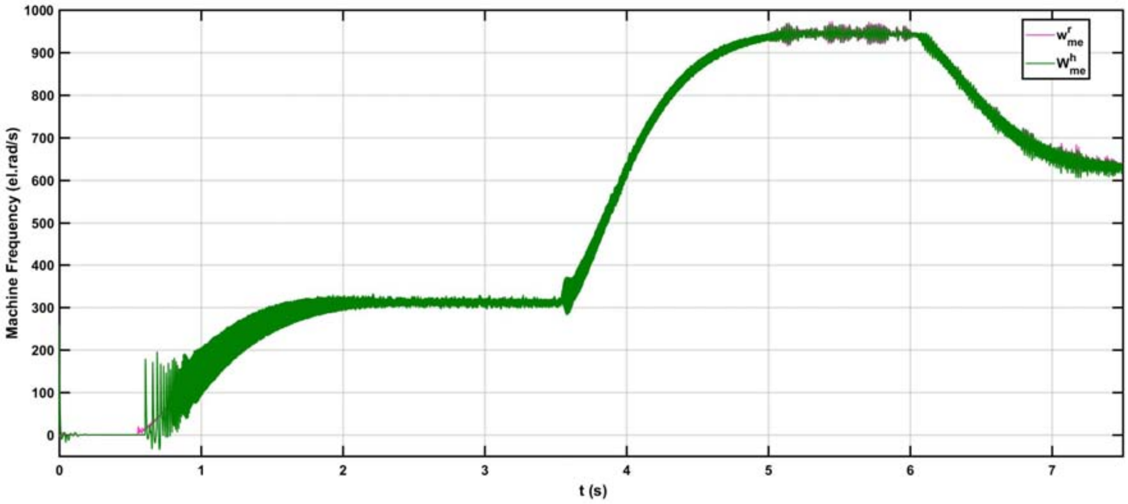

Figure 3.41 *- Real and extracted machine frequency representation.*

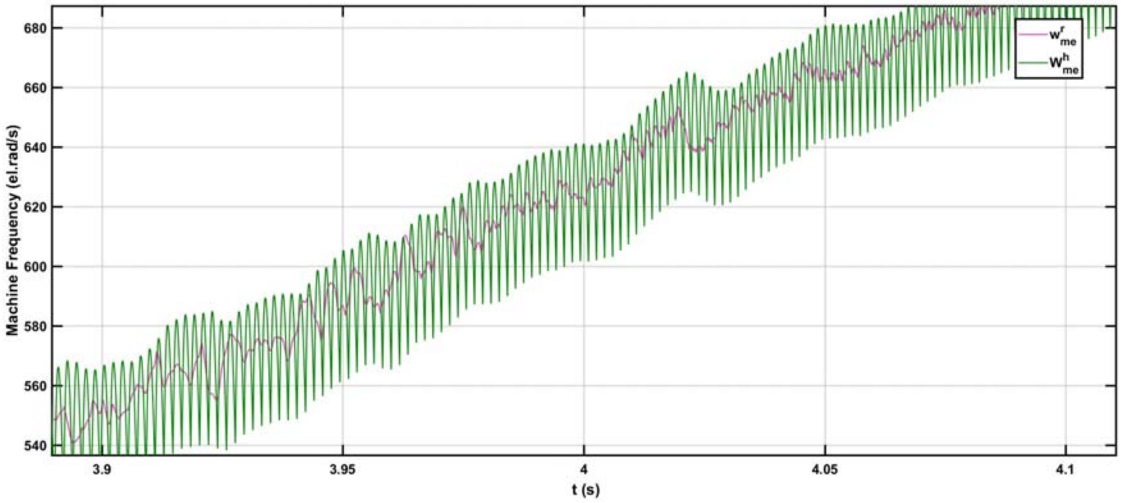

Figure 3.42 *- Real and extracted machine frequency enlarged in time.*

The two speeds are both affected by high-frequency noise present on the scheme as can be better seen in Figure 3.42. Despite of this noise, it can be noticed that they seem overlap quite well. To show that they actually overlap the two speeds are then shown in Figure 3.43, that displays the two signals filtered with a Butterworth *Low-Pass Filter* with passband edge frequency of $20\ Hz$, that cleans them from all the high-frequency noise.

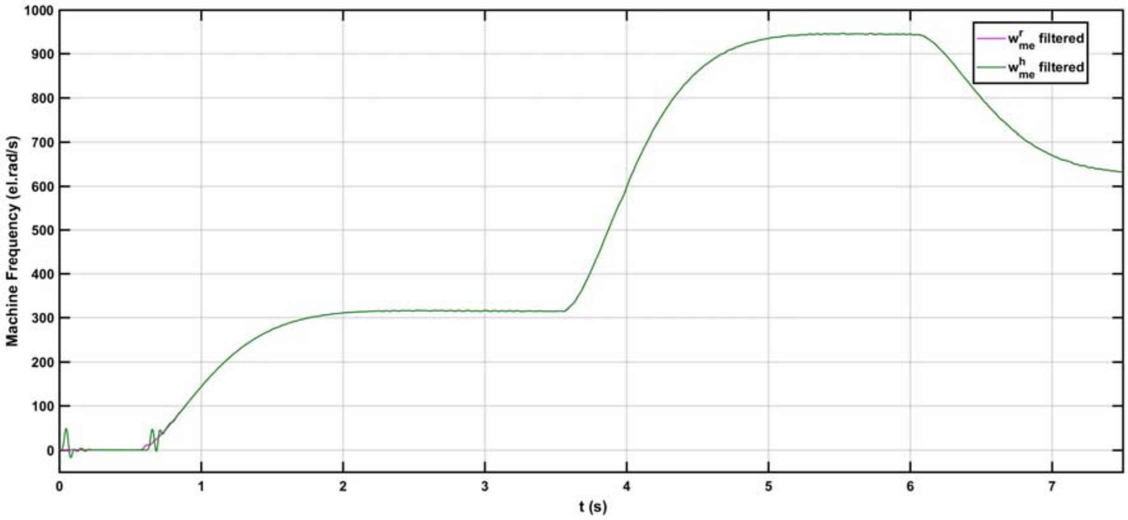

Figure 3.43 *- Real and extracted machine speed after have been filtered.*

Are now shown two enlargement of the Figure 3.44 and 3.45, for a more clear comprehension of the accuracy of the data.

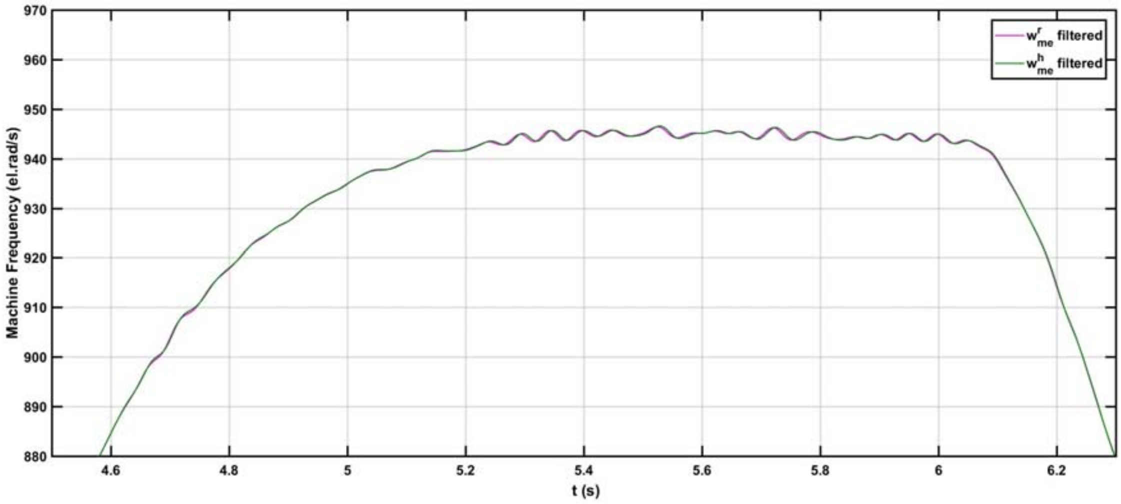

Figure 3.44 *- Enlargement of the real and extracted machine speed after have been filtered*

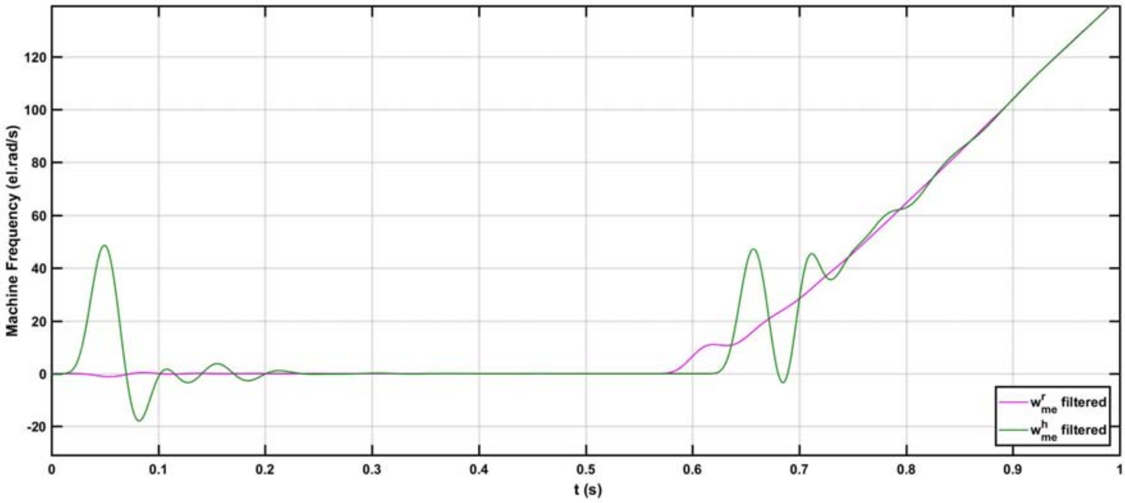

Figure 3.45 *- Enlargement of the real and extracted machine speed after have been filtered*

The few inaccuracies present at the initial part of the speed images are due to the low speed, that implies an incorrect back-EMF and angle estimation by the low resolution Hall-effect. sensors.

At last, the position angle extracted is shown in Figure 3.46.

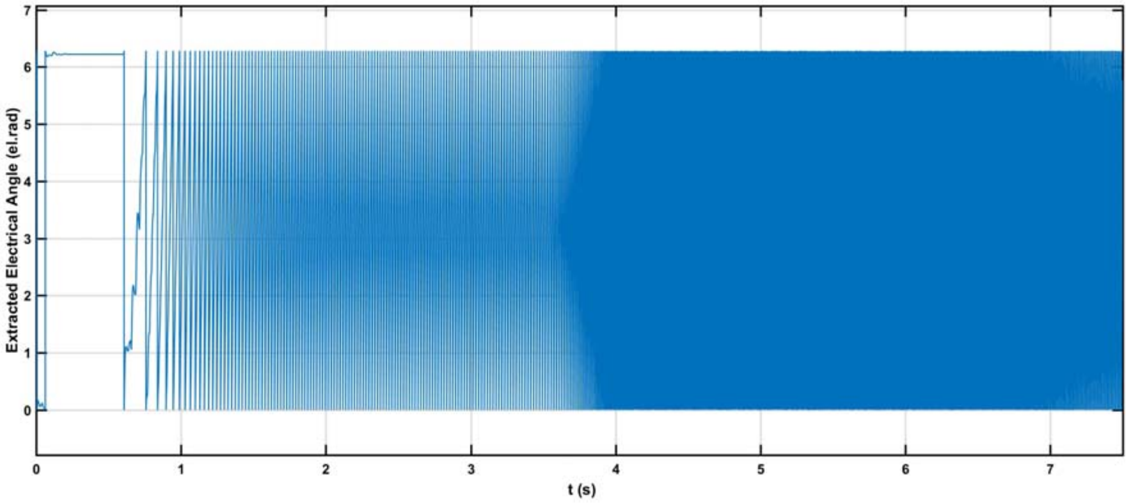

Figure 3.46 *-* θ^h_{me} *representation.*

This last figure displays the θ^h_{me} , that is the $\theta^h_{me\_err}$ compensated of the $60^{el.°}$ phase shift from the angle information coming from the Simulink machine model. A part from the almost first second, when the machine speed is not high enough to provide a correct back-EMF information form the three Hall-effect sensors, as have been already shown in Figure 3.6, the extracted angle (once it is compensated) is almost coincident with the one provided by the machine model. This is demonstrate in the §3.8, where it has been shown in 3.31, that the shift between θ^r_{me} and θ^h_{me}

is always included between $\pm 10^{el.\circ}$. Here is display in the following Figure 3.47 a zoom of the two angles in comparison.

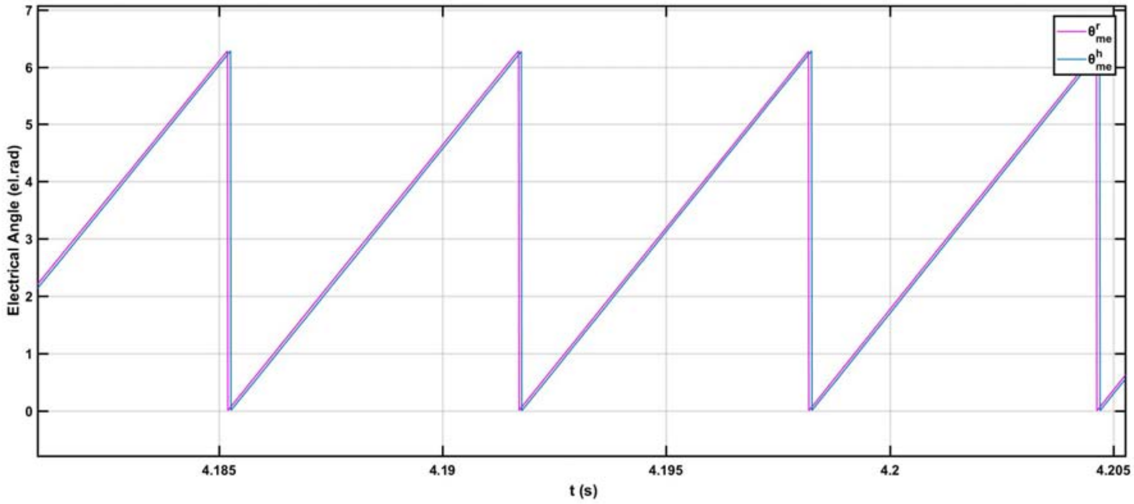

Figure 3.47 *- Real and estimated angle comparison.*

The results provided in this chapter prove that the machine frequency/position estimation with the developed scheme is correct. The practical work of this thesis will be described on the next chapter.

CHAPTER 4

PRACTICAL EXPERIMENTATIONS

This chapter discusses the experimental implementation of the multiple-complex coefficient-filter(MCCF)-based phase-looked loop synchronization technique using analog Hall-effect sensors.

4.1 Test Bench Description

For the experimentations the set up used is the one schematized in Figure 4.1. It is located at the Electric Machines Laboratory of the Escuela Politécnica de Ingenería de Gijón.

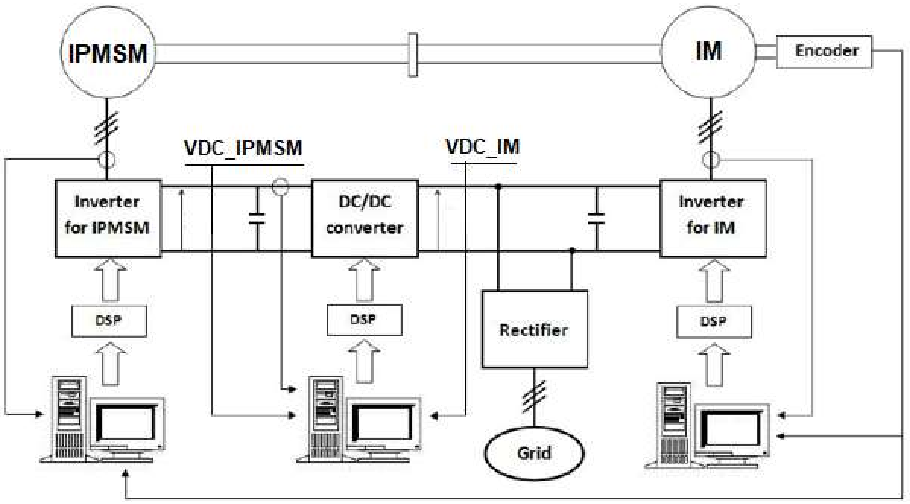

Figure 4.1 *- Experimentations set up illustration.*

This test bench consists of two coupled machines, an Induction Motor (IM) that works as motor, and an Interior Permanent Magnet Synchronous Motor (IPMSM) that works as load. The Figures 4.2 and 4.3 show the two machines from am above and lateral point of view.

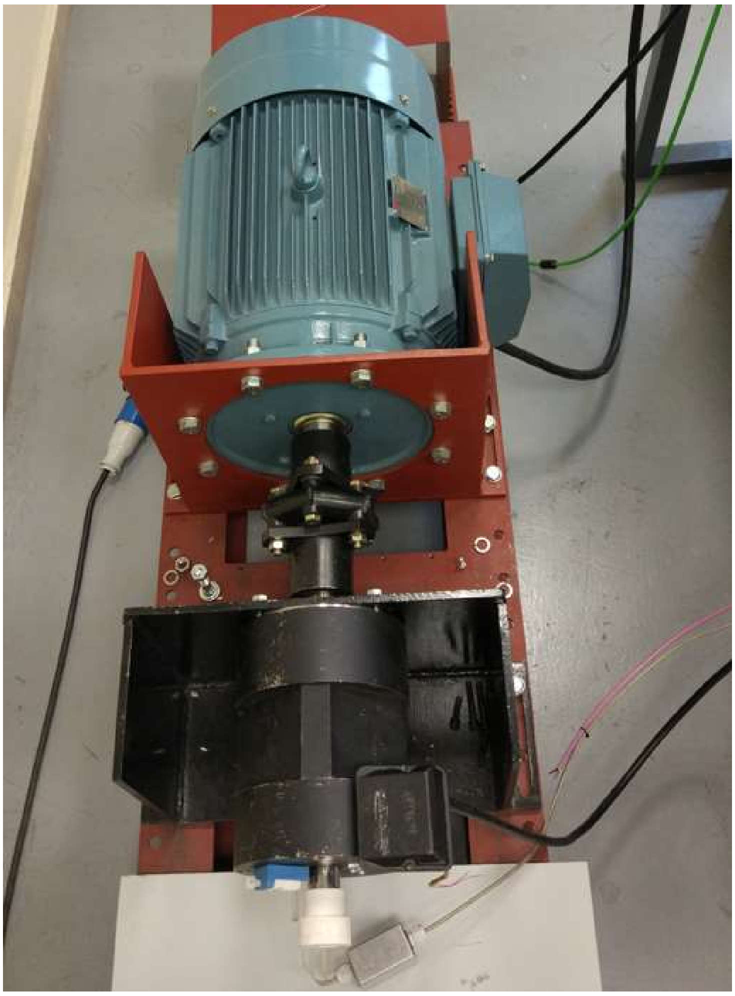

Figure 4.2 *- View from above of the two coupled machines.*

Figure 4.3 *- Lateral point of view of the two coupled machines.*

The main parameters of the IPM motor used are reported on the Table 4.1 below.

Table 4.1 *- Plate data of the Interior Permanent Magnet Synchronous Machine.*

Parameters	**Values**
Power	7.5 kW
Rated Torque	55 Nm
Rated Speed	1800 rpm
Rated Phase Voltage	300 V
Rated Phase Current	14 A
Pole Pairs	3
Stator resistance (R_s)	1.7
d-axis inductance (L_d)	0.00205 H
q-axis inductance (L_q)	0.00391 H

For the IM machine, the parameters are reported in the subsequent Table 4.2 for the case of a delta-connection of the stator winding.

Table 4.2 *- Plate data of the Induction Machine.*

Parameters	**Values**
Power	45 kW
Rated Torque	55 Nm
Rated Speed	2970 rpm
Rated Phase Voltage	400 V
Rated Phase Current	78.81 A
Pole Pairs	1

The IM machine is controlled through encoder and is used to set the speed profile that the IPMSM, physically attached, has to follow. The IPMSM machines, instead, has implemented on itself six Hall-effect sensors: three in the radial direction of the internal magnetic field and three on the tangential direction as can be seen in Figure 4.4 and Figure 4.5.

Figure 4.4 *- View on the Hall-effect sensors placed on the end shield of the IPM machine.*

Figure 4.5 *- View on the Hall-effect sensors placed on the end shield of the IPM machine.*

These two different direction were chosen for previous studies carried out by the research group of the laboratory, and these are about temperature and field distribution measurement system for IPMSM and estimation of the magnetization estate of the machine. In this work are used only the sensors placed on the radial direction of the magnetic field because the other ones had problems in the conditioning electronic circuits.

As one can see from Figure 4.1, each machine is fed from an inverter of $100\ kW$ that is in turn controlled by the corresponding Digital Signal Processor (DSP). There is another DSP that controls the DC/DC converter used to change the value of the DC voltage V_{DC_IPMSM} bus that feeds the inverter connected to the IPMSM. With this converter the bus voltage can be made to vary between $0\ V$ to $480\ V$, but for the experimentations will be set a $400\ V$ voltage. The two inverters and the DC/DC converter are three-legs power converters using IGBT transistors as switches. The power is supplied by the greed at $400\ V$ AC, converted by a diodes rectifier in a DC voltage V_{DC_IM} of $560\ V$. The resulting system is completely flexible as the energy con flow in both directions, that is, both machine can work either as a motor or as a generator. As it can be noticed in Figure 4.1, the power links are distinguished from the measuring links using thick lines for the former and thin lines for the latter.

The interface used to program the DSPs is the integrated development environment Code Composer Studio 5.3.0 provided by Texas Instruments. The different codes used are written and compiled on the different computers, which transfers them to the corresponding DSP implementing the control. For this work it has been written only on the PC controlling the DSP correlated to the IPM machine. The DSP adopted is the 32-b fixed-point TMS320F2812 with sample rate of 10 kHz and the Q variables used are on IQ19 format.

In the following pictures are shown the rectifier and the inverter connected to the Induction Machine, the inverter connected to the IPMSM and then the DC/DC rectifier.

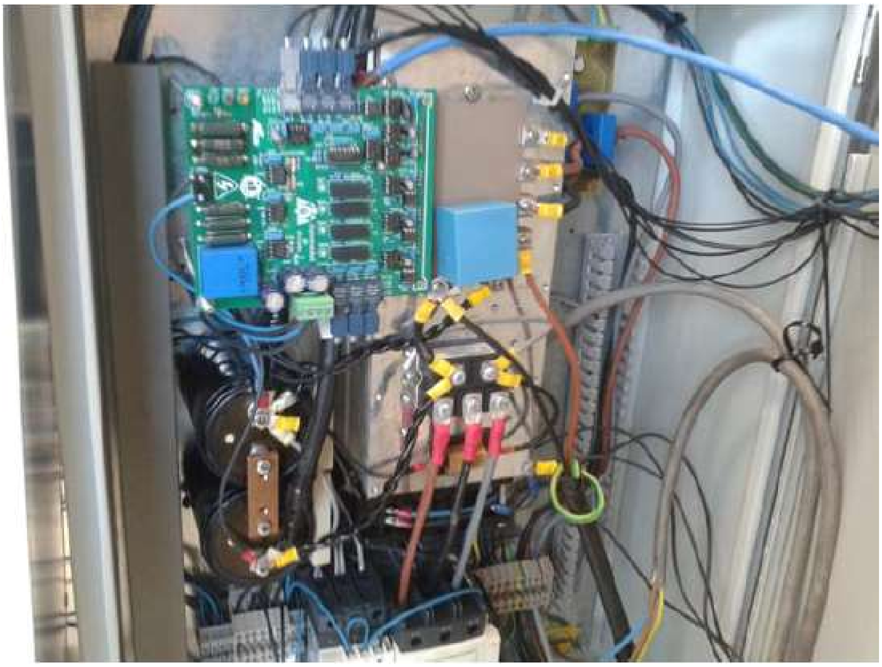

Figure 4.6 *- Rectifier and inverted connected to the IM.*

Figure 4.7 *- Inverter connected to the IPM synchronous machine.*

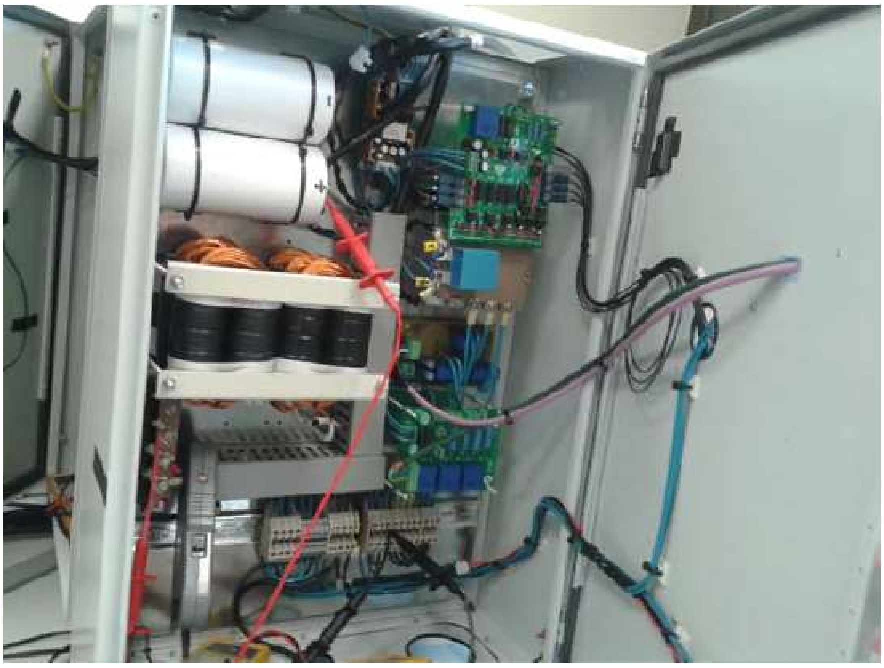

Figure 4.8 *- DC/DC converter.*

In this last, is shown the overall view of the system, including the cabinets containing the three power converter shown above.

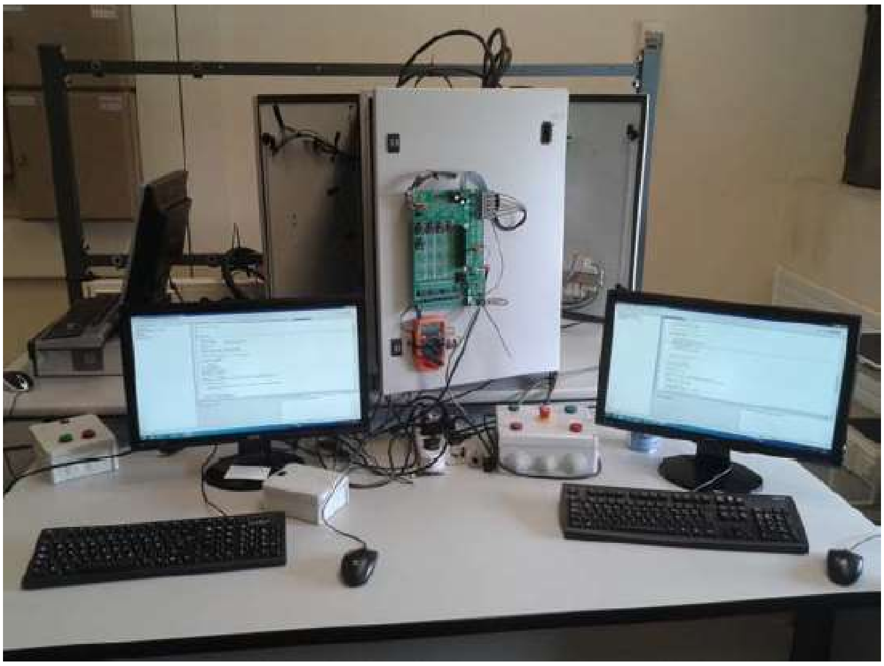

Figure 4.9 *- Workstation.*

4.2 Hall-effect sensors conditioning

The sensors used are Continuous-Time Ratiometric Linear Hall Effect Sensor ICs A1302 from Allegro MicroSystem LLC. They are optimized to accurately provide a voltage output that is proportional to an applied magnetic field. These devices have a quiescent (that is with no significant magnetic field: $B = 0$) output voltage that is 50% of the supply voltage, and they are supplied with a 5 V voltage.

The Hall-effect integrated circuit included in each device includes a Hall circuit, a linear amplifier, and a CMOS Class A output structure. Integrating the Hall circuit and the amplifier on a single chip minimizes many of the problems normally associated with low voltage level analogic signals.

High precision in output levels is obtained by internal gain and offset trim adjustments made at end-of-line during the manufacturing process. They have a temperature range from -40°C to 125°C which suit the operating range of the used machine. In the following are shown variations of the output voltage according to the temperature and voltage supply, the main characteristics of this kind of sensor.

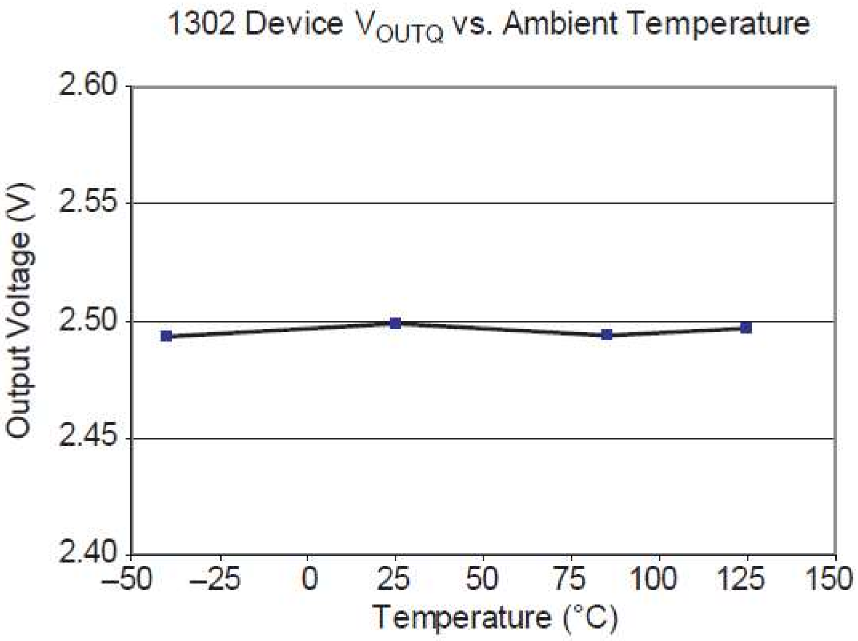

Figure 4.10 - *Output voltage variation according to the temperature.*

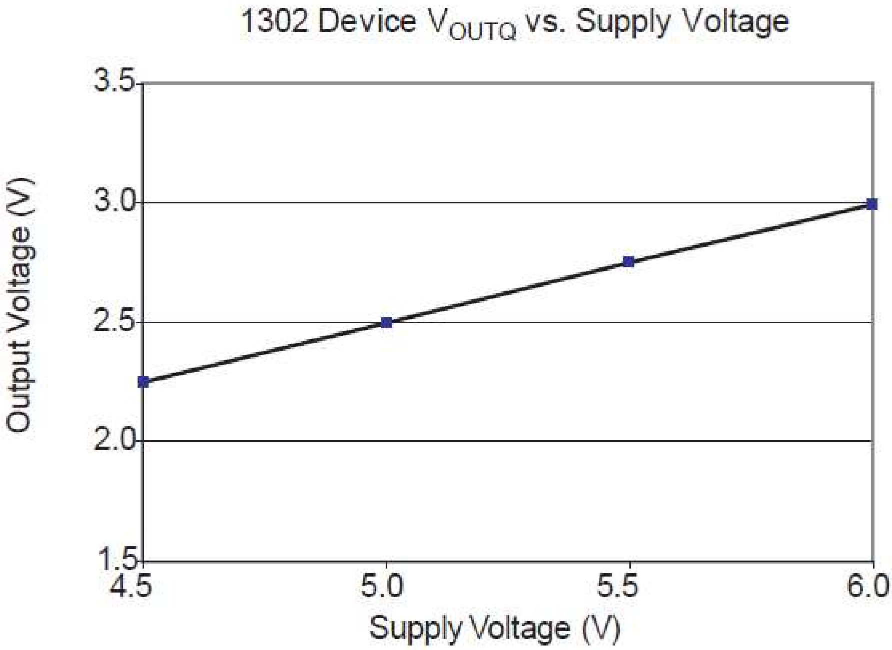

Figure 4.11 *- Output voltage variation according to the supply voltage.*

Now that a brief description of the Hall-effect sensors utilized is given, it will be described the conditioning circuit in Figure 4.12. This circuit has the task of adapting the parameters of electricity, generated by the transducer, to the input characteristics of the measuring system (signal conditioning) that is a microcontroller with $0 \div 3\ V$signal input voltage. In fact the Hall-effect sensors are passive transducer. These kind of transducers must necessarily be inserted within a conditioning circuit so that the physical quantity applied to the input produces a variation of an electrical parameter that is associated with a voltage, current or signal frequency variation. In this case the electrical parameter that varies is the resistance and is hence associated with a voltage variation.

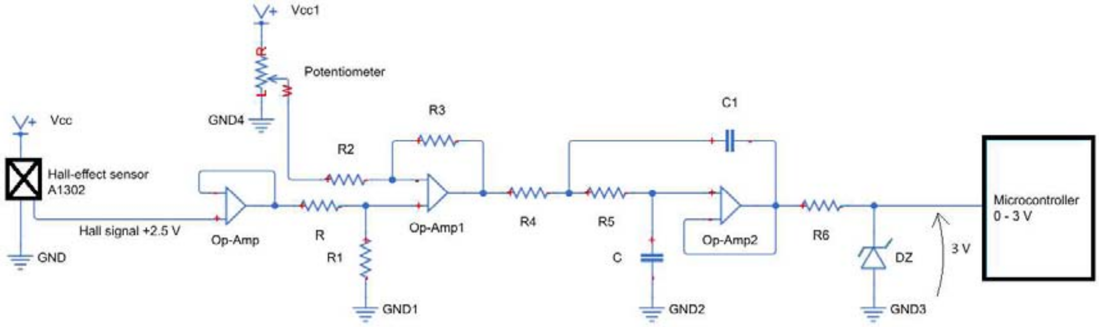

Figure 4.13 *- Hall-effect sensors conditioning circuit.*

As can be seen, the first stage is the Hall-effect sensor with the output voltage around the $+2.5\ V$, that is a theoretical mean value.

The next stage is an operational amplifier configured as Voltage Follower. This is an high-impedance follower that creates a galvanic isolation between the circuit in input and output. In this way, the current absorbed from the amplifier, is zero and the signal from the sensor is not modified by the load.

Subsequently there is a differential operational amplifier, with on one input the signal from the sensor and on the other one the signal from a potentiometer. The last one is used to correct the mean value of the sensor one. This mean value con be also modified by the CCS code on the channels reading. The important of the possibility to modify this value is that, as all the sensors, the Hall-effect sensor is affected of temperature variation, not perfect positioning on the machine, vibrations etc., so the given mean value can be not the one expected.

After this stage there is a Sallen-Kay Typology filter, a second order low-pass filter to avoid all the noises and disturbs that can affect the signal.

At last, there is a Zener-diode, necessary to limit the voltage of the signal to the accepted values in input of the microcontroller. Once the signal is received, the microcontroller subtracts to it the mean value and create a signal oscillating around the zero value.

4.3 CCS code

In this section the behavior of the IPMSM is investigated, and for this purpose it has been modified a CCS interrupt subroutine code previously used in the laboratory for other projects. This code is implemented in the DPS which controls the inverter that feeds the IPM machine. On the contrary, for the inverter that feed the induction machine and the DC/DC converter it has been used ready codes. Inasmuch is the IPM the object of analysis and the IM machine is only used to rotate the IPM ones.

Will be shown only the principal part of the code that have been created and/or modified for the thesis aim, not showing the scripts already existing that are covered by copyright.

First modification of the code, that is called inside the main script, is the digitalization of the signals coming from the Hall-effect sensors. These signals, being analog, have a sinusoidal trend but the majority of the commercial machine are equipped with digital sensors because they are mainly used to detect the polarity of the machine while is running. The digital sensors have also some advantages respect the analog ones: they require less post processing and less electronics since they give a signal that can be used directly on a microcontroller in a simpler way. Besides, they are less sensible to the temperature variations and are way less affected by noise, which are always present during the working mode of an electrical machine. Hence, the utilization of digital signals has more practical feedback than the analog case.

The digitalization procedure is reported hereunder.

```
x90=ReadADInput(ADCINB7);
x50=ReadADInput(ADCINB6);
x10=ReadADInput(ADCINB5);

Update_Data();

x90_data[N]=x90;
x50_data[N]=x50;
x10_data[N]=x10;

e_abx.d=_IQmpy(x90,_IQ(0.6667))-
        _IQmpy(_IQmpy(x50,_IQ(0.5)),_IQ(0.6667))-
        _IQmpy(_IQmpy(x10,_IQ(0.5)),_IQ(0.6667));
e_abx.q=_IQmpy(_IQmpy(x50,(SQRT3DIV2)),_IQ(0.6667))-
      _ _IQmpy(_IQmpy(x10,(SQRT3DIV2)),_IQ(0.6667));

e_abx_norm.d=_IQdiv(e_abx.d,_IQmag(e_abx.d,e_abx.q));
e_abx_norm.q=_IQdiv(e_abx.q,_IQmag(e_abx.d,e_abx.q));

x_a=e_abx_norm.d;
x_b=_IQmpy(e_abx_norm.d,_IQ(-0.5))+_IQmpy(e_abx_norm.q,(SQRT3DIV2));
x_c=_IQmpy(e_abx_norm.d,_IQ(-0.5))-_IQmpy(e_abx_norm.q,(SQRT3DIV2));

if(x_a>=trashold_pos)
            digit_x90[N]=_IQ(1);
       else if (x_a<=trashold_neg)
                        digit_x90[N]=_IQ(0);
                  else digit_x90[N]=digit_x90[N1];
if(x_b>=trashold_pos)
            digit_x50[N]=_IQ(1);
         else if (x_b<=trashold_neg)
                        digit_x50[N]=_IQ(0);
                  else digit_x50[N]=digit_x50[N1];
if(x_c>=trashold_pos)
            digit_x10[N]=_IQ(1);
         else if (x_c<=trashold_neg)
                        digit_x10[N]=_IQ(0);
                  else digit_x10[N]=digit_x10[N1];
```

After reading the channels concerning to the Hall-effect sensors and have updated all the variables needed in the script, to the volatile variable with memory `x90_data[N]`, `x50_data[N]`, `x10_data[N]` is assigned the Hall signals values. These are firstly saved as variable without data and then used to obtain the alpha and beta components, `e_abx.d`, `e_abx.q` of the back-EMF, as in the case of the Simulink model. To this purpose is used the Clarke transformation applying the matrix in formula (3.6). The two components are then normalized and reconverted in the stationary abc reference frame: `x_a`, `x_b`, `x_c`, implementing the matrix in formula (3.7). This procedure is used to do not influence the results with the different magnitudes of the signals coming from the Hall-effect sensors. The signals obtained are then digitalized applying a Schmitt Trigger code, that lead to the signals `digit_x90[N]`, `digit_x50[N]`, `digit_x10[N]`.

This is a particular kind of threshold comparator with hysteresis, that is, a circuit that allows to transform an analog signal into an output that varies only between two voltages values depending on whether the input exceeds a certain threshold or is lower than a second threshold. The switching of the output must takes place in an ideally null time, in practice much less of the characteristic time with which the input signal varies. The two trigger thresholds are one high and one low, not coincident: when the Hall signal is below the low threshold, the output assumes the low value; when the Hall signal is above the high threshold, the output assumes the high value. When the input value is between the two thresholds, the output retains the previous value until the input has changed sufficiently to start the trigger (trigger action). This operation implies some memory in the trigger that takes the name of hysteresis, ad for this reason are used volatile variable with memory (two slots memory): `digit_x90[N]`, `digit_x50[N]`, `digit_x10[N]`. The two threshold are: `threshold_neg`$= -0.001$, `threshold_pos`$= 0.001$, the low value is 0, while the high one is 1 according to the digital one level signal.

The benefit of the Schmitt trigger compared to other systems at a single input threshold is represented by its greater stability. In fact, with only one input threshold, a noisy entry signal, close to the threshold value like the one coming from the Hall-effect sensors, can swing quickly around this value, oscillating also the output between its low and high value. With the Schmitt Trigger, a noisy signal near a threshold can cause only one switching of the output value, after which it must grow or decrease to the other threshold in order to cause further switching.

The three digital signals obtained are thus converted again in the alpha and beta back-EMF components applying the formula (3.6), and then normalized.

```
e_abx_mccf.d=_IQmpy(digit_x90[N],_IQ(0.6667))-
            __IQmpy(_IQmpy(digit_x50[N],_IQ(0.5)),_IQ(0.6667))-
            __IQmpy(_IQmpy(digit_x10[N],_IQ(0.5)),_IQ(0.6667));
e_abx_mccf.q=_IQmpy(_IQmpy(digit_x50[N],(SQRT3DIV2)), _IQ(0.6667))-
            _IQmpy(_IQmpy(digit_x10[N],(SQRT3DIV2)),_IQ(0.6667));

e_abx_mccf_norm.d=_IQdiv(e_abx_mccf.d,
                  _IQmag(e_abx_mccf.d,e_abx_mccf.q));
e_abx_mccf_norm.q=_IQdiv(e_abx_mccf.q,
                  _IQmag(e_abx_mccf.d,e_abx_mccf.q));

MCCF_PLL() ;
```

Finally the subroutine *`MCCF_PLL`* is called. This one contain the Multi-Complex Coefficient-Filter SRF PLL and return the estimated frequency and position. Its code is shown below.

```
void MCCF_PLL(void);
void BP_CCF_Vod(volatile_iq*Vod,volatile_iq*Vid,volatile_iq*Viq,
                  volatile_iq*Vid_n1,volatile_iq*Viq_n1,volatile_iq*
                  Vid_n2,volatile_iq*Viq_n2,volatile_iq*Vod_n1,
                  volatile_iq*Vod_n2,volatile_iq*wo);
void BP_CCF_Voq(volatile_iq*Voq,volatile_iq*Vid,volatile_iq*Viq,
                  volatile_iq*Vid_n1,volatile_iq*Viq_n1,volatile_iq*
                  Vid_n2,volatile_iq*Viq_n2,volatile_iq*Voq_n1,
                  volatile_iq*Voq_n2,volatile_iq*wo);

void MCCF_PLL(void)
{

Eab_dec.d[N]=e_abx_mccf_norm.d-Vab_1.d[N1]-Vab_m5.d[N1]-Vab_7.d[N1]-
            Vab_m11.d[N1]-Vabv13.d[N1];
Eab_dec.q[N]=e_abx_mccf_norm.q-Vab_1.q[N1]-Vab_m5.q[N1]-Vab_7.q[N1]-
            Vab_m11.q[N1]-Vab_13.q[N1];

Kp_MCCF_PLL=_IQ(15);
Ki_MCCF_PLL=_IQ(200);

//Band Pass - Positive Sequence
Punto1.d[N]=Eab_dec.d[N]+Vab_1.d[N1];
Punto1.q[N]=Eab_dec.q[N]+Vab_1.q[N1];
BP_CCF_Vod(&Vab_1.d[N],&Punto1.d[N], &Punto1.q[N], &Punto1.d[N1],
            &Punto1.q[N1],&Punto1.d[N2], &Punto1.q[N2], &Vab_1.d[N1],
            &Vab_1.d[N2],&f_PLL_f[N1]);
BP_CCF_Voq(&Vab_1.q[N], &Punto1.d[N], &Punto1.q[N], &Punto1.d[N1],
            &Punto1.q[N1],&Punto1.d[N2], &Punto1.q[N2], &Vab_1.q[N1],
            &Vab_1.q[N2], &f_PLL_f[N1]);
```

```
//Band Pass - -5th Harmonic
Punto5m.d[N]=Eab_dec.d[N]+Vab_m5.d[N1];
Punto5m.q[N]=Eab_dec.q[N]+Vab_m5.q[N1];
w_m5=_IQmpy(_IQ(-5.0),f_PLL_f[N1]);
BP_CCF_Vod(&Vab_m5.d[N],&Punto5m.d[N],&Punto5m.q[N],&Punto5m.d[N1],
            &Punto5m.q[N1],&Punto5m.d[N2],&Punto5m.q[N2],
            &Vab_m5.d[N1],&Vab_m5.d[N2],&w_m5);
BP_CCF_Voq(&Vab_m5.q[N],&Punto5m.d[N],&Punto5m.q[N],&Punto5m.d[N1],
            &Punto5m.q[N1],&Punto5m.d[N2],&Punto5m.q[N2],
            &Vab_m5.q[N1],&Vab_m5.q[N2],&w_m5);

//Band Pass - 7th Harmonic
Punto7.d[N]=Eab_dec.d[N]+Vab_7.d[N1];
Punto7.q[N]=Eab_dec.q[N]+Vab_7.q[N1];
w_7=_IQmpy(_IQ(7.0),f_PLL_f[N1]);
BP_CCF_Vod(&Vab_7.d[N],&Punto7.d[N],&Punto7.q[N],&Punto7.d[N1],
            &Punto7.q[N1],&Punto7.d[N2],&Punto7.q[N2],&Vab_7.d[N1],
            &Vab_7.d[N2] &w_7);
BP_CCF_Voq(&Vab_7.q[N],&Punto7.d[N],&Punto7.q[N],&Punto7.d[N1],
            &Punto7.q[N1],&Punto7.d[N2],&Punto7.q[N2],&Vab_7.q[N1],
            &Vab_7.q[N2],&w_7);

//Band Pass - -11th Harmonic
Punto11m.d[N]=Eab_dec.d[N]+Vab_m11.d[N1];
Punto11m.q[N]=Eab_dec.q[N]+Vab_m11.q[N1];
w_m11=_IQmpy(_IQ(-11.0),f_PLL_f[N1]);
BP_CCF_Vod(&Vab_m11.d[N],&Punto11m.d[N],&Punto11m.q[N],
            &Punto11m.d[N1],&Punto11m.q[N1],&Punto11m.d[N2],
            &Punto11m.q[N2],&Vab_m11.d[N1],&Vab_m11.d[N2],&w_m11);
BP_CCF_Voq(&Vab_m11.q[N],&Punto11m.d[N],&Punto11m.q[N],
            &Punto11m.d[N1],&Punto11m.q[N1],&Punto11m.d[N2],
            &Punto11m.q[N2],&Vab_m11.q[N1],&Vab_m11.q[N2],&w_m11);

//Band Pass - 13th Harmonic
Punto13.d[N]=Eab_dec.d[N]+Vab_13.d[N1];
Punto13.q[N]=Eab_dec.q[N]+Vab_13.q[N1];
w_13=_IQmpy(_IQ(13.0),f_PLL_f[N1]);
BP_CCF_Vod(&Vab_13.d[N],&Punto13.d[N],&Punto13.q[N],&Punto13.d[N1],
            &Punto13.q[N1],&Punto13.d[N2],&Punto13.q[N2],
            &Vab_13.d[N1],&Vab_13.d[N2],&w_13);
BP_CCF_Voq(&Vab_13.q[N], &Punto13.d[N], &Punto13.q[N],&Punto13.d[N1],
            &Punto13.q[N1],&Punto13.d[N2],&Punto13.q[N2],
            &Vab_13.q[N1],&Vab_13.q[N2],&w_13);

Vab_1_norm.d[N]=_IQdiv(Vab_1.d[N],_IQmag(Vab_1.d[N],Vab_1.q[N]));
Vab_1_norm.q[N]=_IQdiv(Vab_1.q[N],_IQmag(Vab_1.d[N],Vab_1.q[N]));
```

```
//SRF-PLL
      ROTATE_POS(Vab_1_norm,Eqd,theta_PLL[N1]-PIDIV2-_IQ(0.384));
      f_PLL[N]=f_PLL[N1]-_IQmpy(Kp_MCCF_PLL,-Eqd.q[N1]) +
            __IQmpy((Kp_MCCF_PLL+_IQmpy(_IQmpy(Kp_MCCF_PLL,Ki_MCCF_PLL),DT)
            ),-Eqd.q[N]);
      f_PLL_f[N]=(_IQmpy(B0_LPF1_f,(f_PLL[N]+f_PLL[N1]))+
                  _IQmpy(A1_LPF1_f,f_PLL_f[N1]));
      INT(f_PLL,theta_ref_PLL);
      WRAP2PI(theta_ref_PLL[N]);

      theta_PLL[N]=theta_ref_PLL[N]+PIDIV2-_IQ(0.384);

      WRAP2PI(theta_PLL[N]);
      phase_shift=phase_rotor[N]-theta_PLL[N];
      WRAP2PI(phase_shift);
      }
      void BP_CCF_Vod(volatile_iq*Vod,volatile_iq*Vid,volatile_iq*Viq,
                        volatile_iq*Vid_n1,volatile_iq*Viq_n1,
                        volatile_iq*Vid_n2,volatile_iq*Viq_n2,
                        volatile_iq*Vod_n1,volatile_iq*Vod_n2,
                        volatile_iq*wo)
      {
      ViddNTerm=_IQ(31.755123004252532)/2;
      ViddN1Term=_IQ(0.697225974696975)/2;
      ViddN2Term=_IQ(-31.057897029555555)/2;

      ViqdNTerm=_IQmpy(_IQ(-0.001570328771840),*wo)/2;
      ViqdN1Term=_IQmpy(_IQ(-0.003140657543680),*wo)/2;
      ViqdN2Term=_IQmpy(_IQ(-0.001570328771840),*wo)/2;

      VodNTerm=_IQmpy(_IQmpy(_IQ(0.000007073553026306459),*wo),*wo)/2
                  +_IQ(2892.571056174977)/2;
      VoddN1Term=_IQmpy(_IQmpy(_IQ(0.000014147106052612920),*wo),*wo)/2
                  -_IQ(2829.060810166472)/2-_IQ(2829.060810166472)/2;
      VoddN2Term=_IQmpy(_IQmpy(_IQ(0.000007073553026306459),*wo),*wo)/2
                  +_IQ(2766.945016107361)/2;

      *Vod=_IQdiv((_IQmpy(ViddNTerm,*Vid)+_IQmpy(ViddN1Term,*Vid_n1)
            +_IQmpy(ViddN2Term,*Vid_n2)+_IQmpy(ViqdNTerm,*Viq)
            +_IQmpy(ViqdN1Term,*Viq_n1)+_IQmpy(ViqdN2Term,*Viq_n2)
            -_IQmpy(VoddN1Term,*Vod_n1)-
      _IQmpy(VoddN2Term,*Vod_n2)),VodNTerm);
      }
      void BP_CCF_Voq(volatile_iq*Voq,volatile_iq*Vid,volatile_iq*Viq,
                        volatile_iq*Vid_n1,volatile_iq*Viq_n1,
                        volatile_iq*Vid_n2,volatile_iq*Viq_n2,
```

```
                  volatile_iq*Voq_n1,volatile_iq*Voq_n2,
                  volatile_iq *wo)
{
ViddNTermq=_IQ(31.755123004252532)/2;
ViddN1Termq=_IQ(0.697225974696975)/2;
ViddN2Termq=_IQ(-31.057897029555555)/2;

ViqdNTermq=_IQmpy(_IQ(-0.001570328771840),*wo)/2;
ViqdN1Termq=_IQmpy(_IQ(-0.003140657543680),*wo)/2;
ViqdN2Termq=_IQmpy(_IQ(-0.001570328771840),*wo)/2;

VodNTermq=_IQmpy(_IQmpy(_IQ(0.000007073553026306459),*wo),*wo)/2
            +_IQ(2892.571056174977)/2;
VoddN1Termq=_IQmpy(_IQmpy(_IQ(0.000014147106052612920),*wo),*wo)/2
            -_IQ(2829.060810166472)/2-_IQ(2829.060810166472)/2;
VoddN2Termq=_IQmpy(_IQmpy(_IQ(0.000007073553026306459),*wo),*wo)/2
            +_IQ(2766.945016107361)/2;

*Voq=_IQdiv((-_IQmpy(ViqdNTermq,*Vid)-_IQmpy(ViqdN1Termq,*Vid_n1)
      -_IQmpy(ViqdN2Termq,*Vid_n2)+_IQmpy(ViddNTermq,*Viq)
      +_IQmpy(ViddN1Termq,*Viq_n1)+_IQmpy(ViddN2Termq,*Viq_n2)
      -_IQmpy(VoddN1Termq,*Voq_n1)
      _IQmpy(VoddN2Termq,*Voq_n2)),VodNTermq);
}
```

At the beginning of the subroutine are defined the variables which are used only during its call, these are variables with, and without, memory. Are also defined the parameters called on the subroutines *`BP_CCF_Vod`* and *`BP_CCF_Voq`*, which inside are implemented the bandpass complex-coefficient filters for the *d* and *q* components of the signal.

Once inside the main part of the *`MCCF_PLL`* subroutine, to the alpha and beta components of the back-EMF, `e_abx_mccf_norm.d`, `e_abx_mccf_norm.q`, are subtract all the harmonics that are investigated in the next code, which are the -5th, 7th, -11th, 13th. Then the values of the gains K_P and K_I used in the PI controller of the PLL are settled, and as can been seen they are: `Kp_MCCF_PLL= 15` and `Ki_MCCF_PLL= 200`. These values are obtained manually for attempts, since was not possible to apply the same calculations and results reached in the Simulink simulations because the here investigated IPM machine has different characteristics from the one of the simulations.

Subsequently, the filtering action is implemented calling the bandpass filter subroutines for each harmonics stage and the positive sequence of the fundamental. These subroutines are placed at the end of the shown code, and are a discretization of the corresponding kind of filter provided from a previous code. To test the well behavior of the filtering actions each filter was tested alone, starting from the one of the fundamental positive sequence, with the machine operating in steady state. According with [17], the cutoff frequency of the filtering stages is set to $\omega_c = 222\,rad/$, which imply an optimum dumping ratio of $0.707\omega_0$ for the filter, that ensures an optimum dynamic response. Moreover, differently from the Simulink model, here is used the same value of cutoff frequency for all the filters, not distinguishing from fundamental and others harmonics. This cutoff frequency value affected the design of the `BP_CCF_Voq/Vod` function created by Prof. Christian Blanco of University of Oviedo, bringing the numerical values present on the script.

These bandpass filter subroutines are the ones that creates some problems on the frequency and position estimation, but this point will be discuss on the §6.1.

Once that all the harmonics are detected, the alpha and beta component of the fundamental are normalized, `Vab_1_norm.d[N]`, `Vab_1_norm.d[N]`, and then switched on the DQZ reference frame rotating at the estimated speed of the SFR PLL by mean of the `ROTATE_POS` function shows on the Appendix. In this stage the correction on the estimated angle is done subtracting the values $PIDIV2$ and $\_IQ(0.384)$ that are respectively $\pi/2$ and a number found for attempts.

The SFR PLL extracts the frequency of the machine, `f_PLL[N]`, by implementing a PI discretize controller, filters it to avoid the noisy component, and integrates it to obtain the relative position of the motor, `theta_ref_PLL[N]`. This angle is adapted to fluctuate among the *0* and π values by means of the `WRAP2PI` function, then it is correct, in `theta_PLL[N]`, by a phase filter compensation to yield to a lower possible phase shift. This is because the filtering stages introduce some delay on the operation. Finally the phase shift between the machine angle coming from the encoder (and so the real one), `phase_rotor[N]`, and the estimated one is calculated.

In the end, as can be seen on the next code, to cope the lack of memory problems of the DSP adopted and to better visualize and save the data coming from the experimentations, these data are decimated. This also made it possible to save at the same time two or three variables to have a good comparisons of the values, for example the estimated speed and the one coming from the encoder of the Induction Motor, or all the three Hall signals, the alpha and beta component of the signal and so on.

```
nn=nn+1;
if  ((capture==1))
{
if((nn==10))
{
        if(pp<250)
        {
                //iadat[pp]=digit_x90[0];
                iadat[pp]=x90;
                ibdat[pp]=x50;
                icdat[pp]=x10;
                //iadat[pp]=phase_rotor[0];
                //iadat[pp]=f_PLL[0];
                //iadat[pp]=Vab_13.d[0];
                //iadat[pp]=e_abx_mccf.d;
                //iadat[pp]=phase_shift;

                nn=0;
                pp=pp+1;
        }

        else
        {
                pp=0;
                nn=0;
        }
}
}
```

The data are saved equaling them to the variables `iadat[pp]`, `ibdat[pp]`, `icdat[pp]`. The variable `nn` and `pp` are counters, as `capture`. The latter one was introduced to be able to catch the transitory of speed: the data are saved once the value 1 is typed on the variable window of the CCS program, and this command goes just after to have changed the Induction Motor machine speed.

In the following paragraph the experimentation results are shown.

4.4 Experimentations Results

The following images are obtained from saved data from the CCS code, and are then created using a MATLAB script. The different data are saved at the following speed values:

$-30\ |-60\ |-90\ |-120\ rad/s.$

The speeds are negative because it has been set the IM speed as positive, so the IPM machine, physically attached to it, rotates on the opposite direction.

Besides, are taken in consideration only the data coming from the Hall-effect sensors placed on the radial direction of the magnetic field, and here called `x10`, `x50`, `x90`. They are shifted of $120^{el.\circ}$ that correspond to $40^{el.\circ}$, since the number of pole pairs od the machine is $p = 3$. The time references are indicative since the samples are taken in different occasions, anyway they are correct in their time duration.

At first are shown the three Hall signals at the four different mechanical speeds, as indicated on the top of each graph of Figure 4.14.

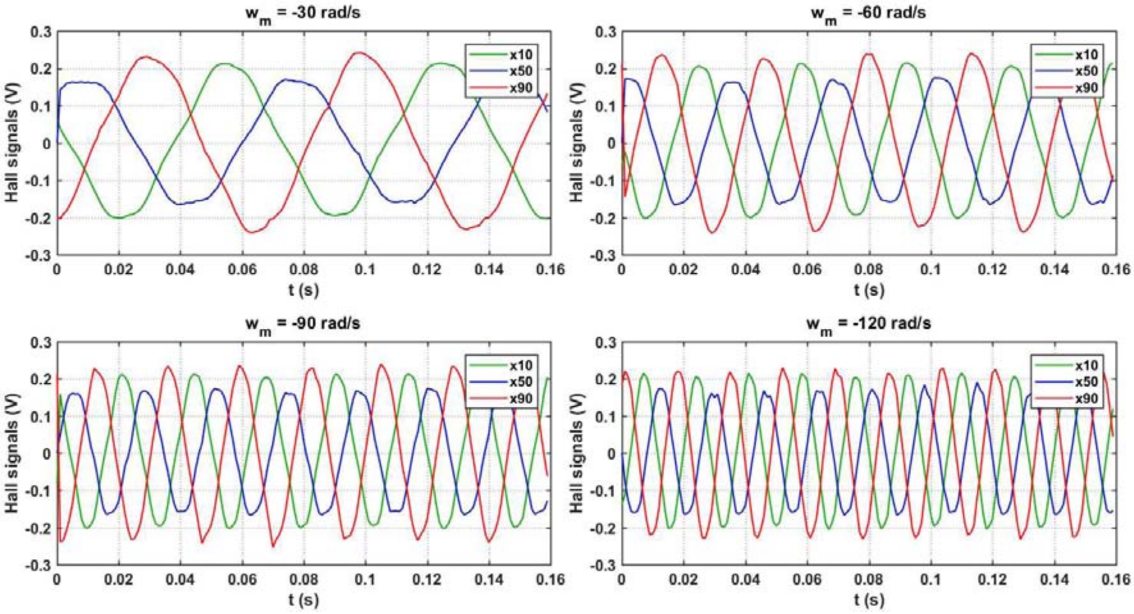

__Figure 4.14__ - Hall signals at different mechanical speeds value.

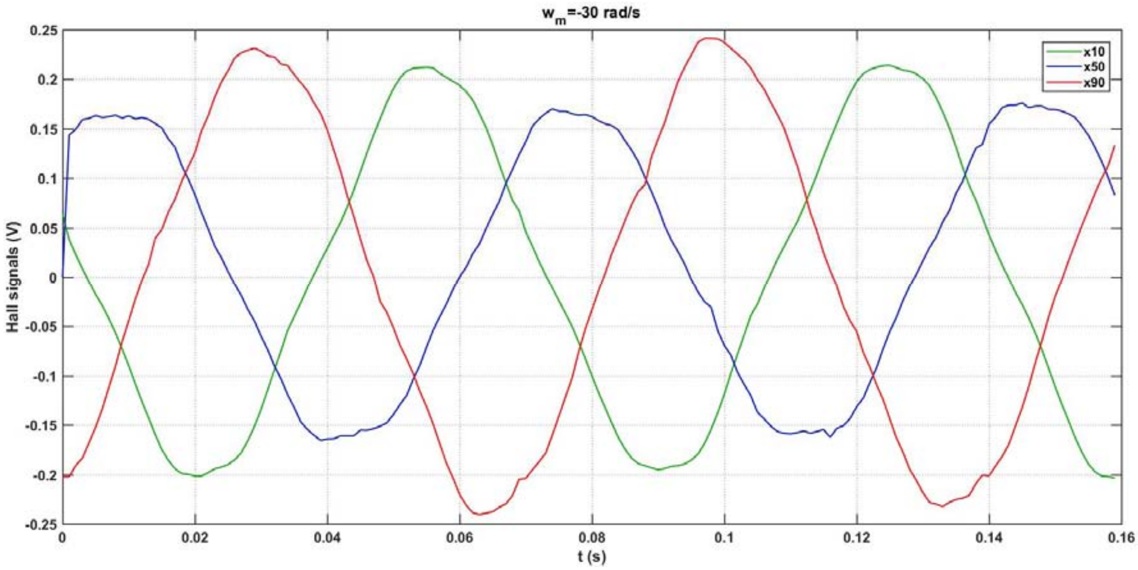

Figure 4.15 *- Enlarged in time of a Hall signal at* $\omega_m = -30\ rad/s$.

Can noticed, more easily with the Figure 4.15, that, despite the same conditioning circuits, the three sensors provide signals slightly different from each other in terms of amplitude and smoothness. For also this reasons is better work with digital Hall-effect sensors that analogic ones. In the following Figure 4.16 are shown the `x90` signal and its respective digitized `digit_x90`.

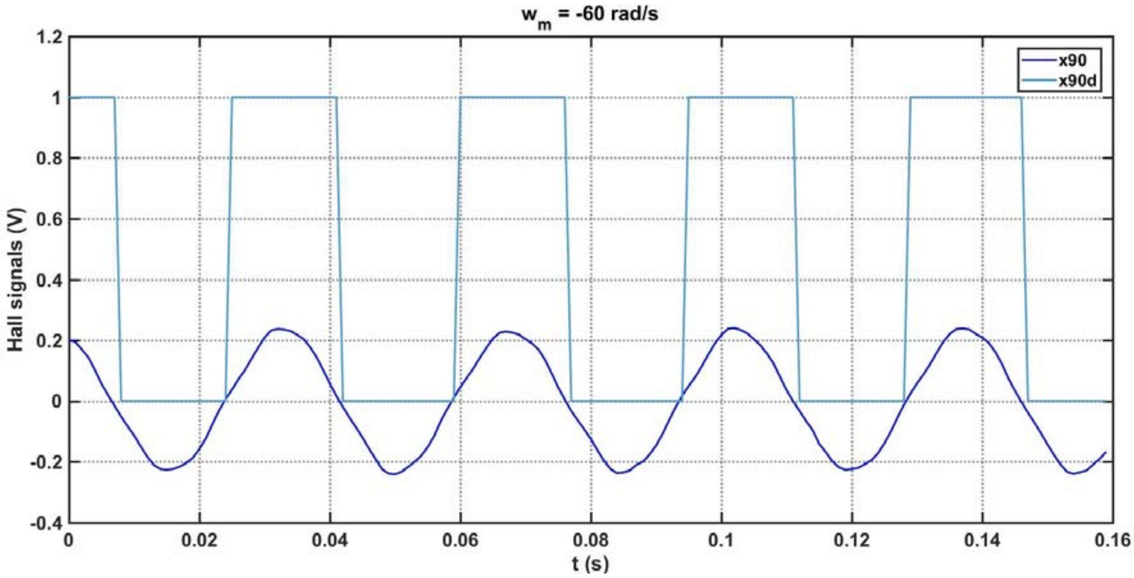

Figure 4.16 *- Representation of a Hall signal in the analogic and digital form.*

The edges of the digital signal are not perfectly vertical, but a bit tilt. This is only a graphic problem due to the little memory of the DSP and the decimation of the data, necessary to save more signal on the same time. On the next Figure 4.17 are present the three digitized signals at the mechanical speed of $-60\ rad/s$.

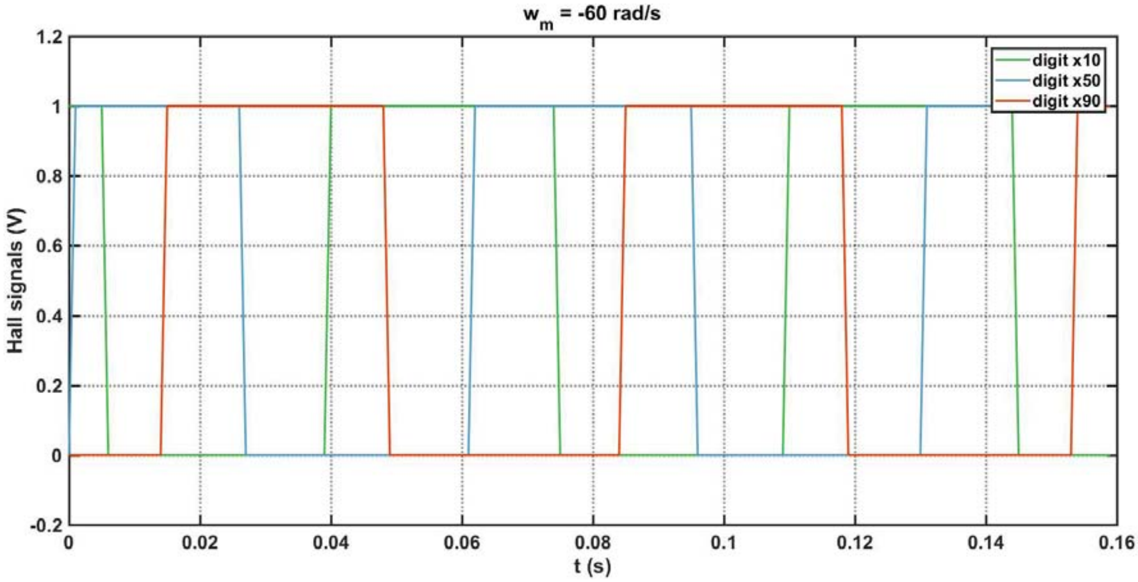

Figure 4.17 *- The three Hall digitized signal.*

From these three digital signals is extracted the back-EMF of the machine, represented in Figure 4.18. The alpha and beta components here are called as in the CCS script, respectively, `E_abx_mccf.d`, `E_abx_mccf.q`.

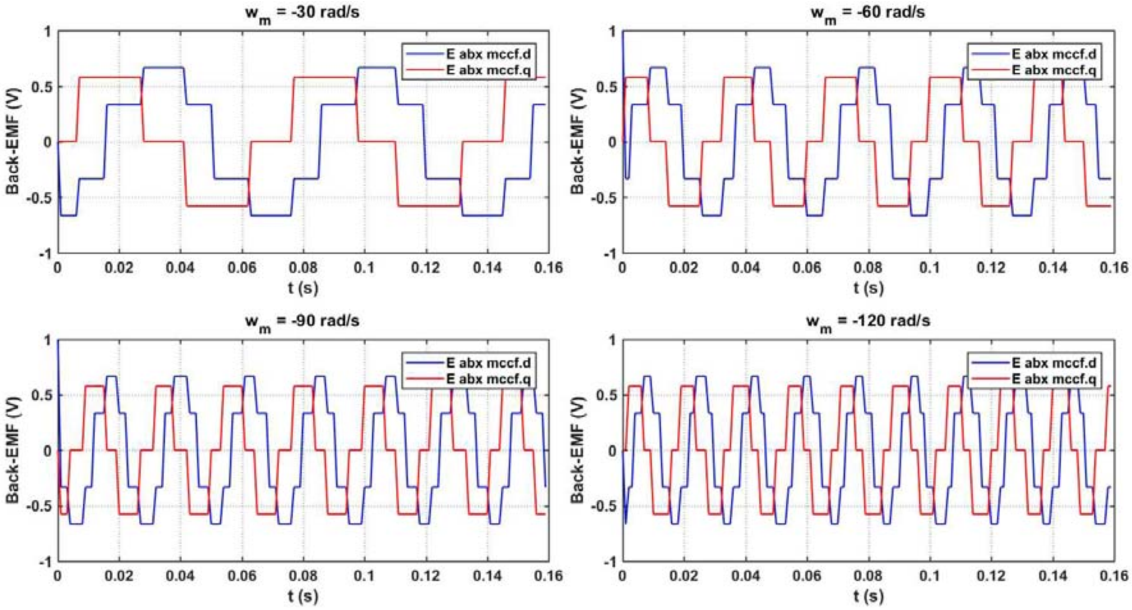

Figure 4.18 *- Back-EMF signals extracted from the Hall-effect sensors signals.*

Also the borders of the newly obtained signals are not vertical, for the same decimation problem hinted before. Comparing the figure above with Figure 3.15, comes out that the machine rotates on the opposite direction of the Simulink simulation, thus counterclockwise. This two components must be normalized before enter on the *MCCF-PLL* stage, as is represented in Figure 4.19, with the names given on the script and the exceptional mechanical speed of $-75\,rad/s$.

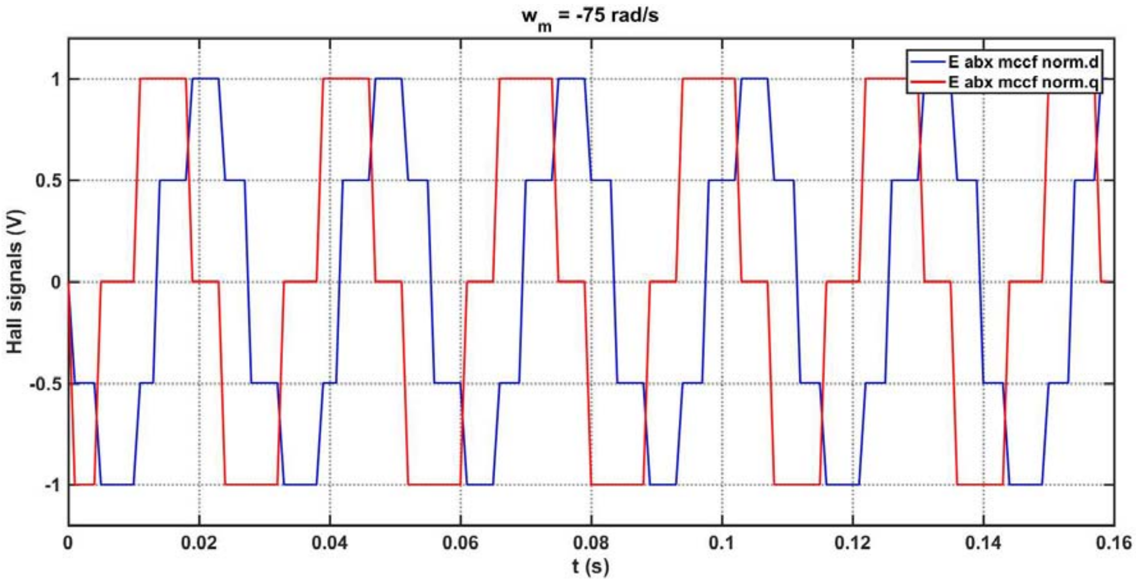

Figure 4.19 *- Normalize version of the back-EMF component obtained from the Hall signals.*

The alpha and beta components obtained from the Hall-effect sensors are sent as input in the $MCCF$ function that has to extract the frequency and position of the IPM machine. In this function are implemented all the operation that have been already explain on the previous chapters. Are here shown the fundamental-frequency positive components of the back-EMF signals in input for two speed levels. Those are the normalized version of the fundamental filtered by the Multi-Complex Coefficient-Filter because these kind of signals allow better results once they are used in the SFR-PLL.

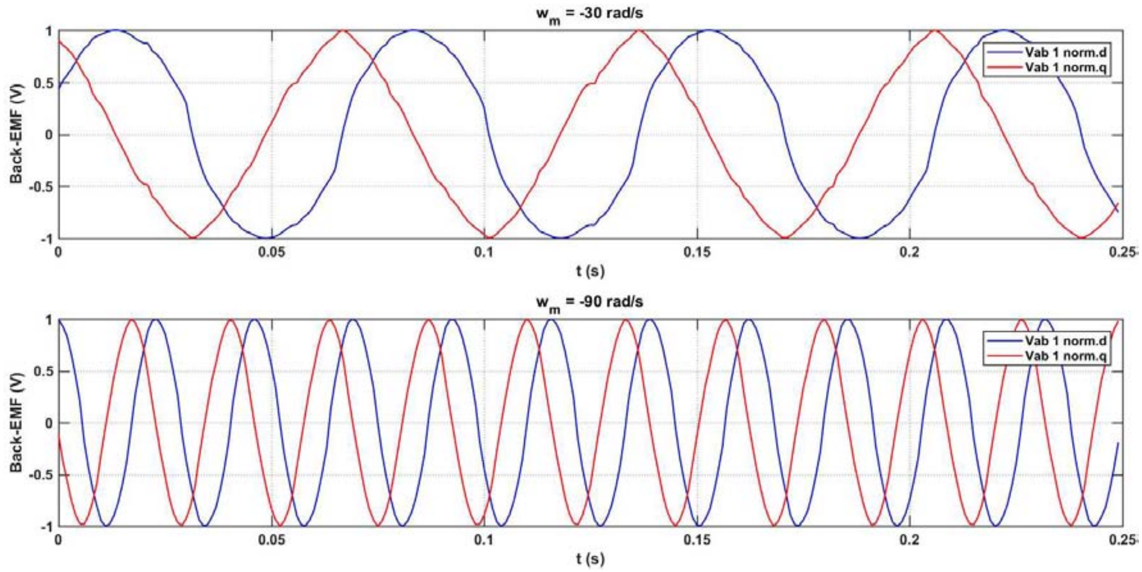

Figure 4.4 *- Fundamental-frequency positive component of the back-EMF.*

It can be noticed as with the increasing of the speed the signals extracted are better. This come for the same reason of the Simulink simulation, that is the discrete absolute-position information with electrically $\pm 30°$ resolution, provided by the Hall-effect sensors, that cause a low resolution rotor angle feedback which affects the back-EMF estimation mainly at low speed. From the two signals shown in Figure 4.20, are obtained the electric frequency of the machine and its electric angle position by the $SFR-PLL$ function. These two last signals are the `f_PLL[N]`, that is the ω_{me}^{h}, and the `theta_PLL[N]`, that is the θ_{me}^{h}, both coming from the Hall-effect sensors information. The extracted machine frequency, and the machine frequency detected by the encoder, are now represented in the same figures: Figure 4.21, Figure 4.22 and Figure 4.23, for the speed range $0 \div -120\ rad/s$. This speed range has been chosen based on the rated speed of the IPMSM, that is $188.5\ rad/s$. On the top of each figure is reported the mechanical speed, ω_m, and the electromechanical one, ω_{me}, that is obtained multiplying the first by the number of pole pair, $p = 3$.

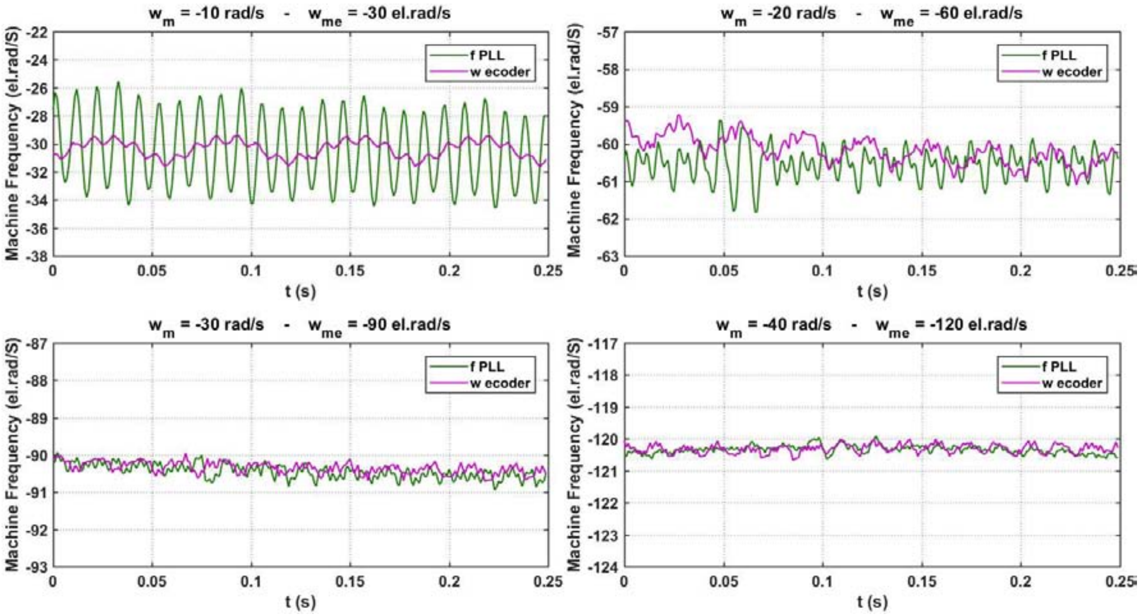
w_m = -10 rad/s - w_{me} = -30 el.rad/s

w_m = -20 rad/s - w_{me} = -60 el.rad/s

w_m = -30 rad/s - w_{me} = -90 el.rad/s

w_m = -40 rad/s - w_{me} = -120 el.rad/s

Figure 4.21 *- Comparison between the speed coming from the encoder and the speed extracted by the implemented script in the low speed range,*

The pictures above demonstrate that at already relative low speed, the machine frequency obtained by the system set utilizing the Hall-effect sensors, follows really well the frequency coming from the encoder placed on the IM machine. Can be settled at $-20\ rad/s$ the lower limit for a good speed estimation.

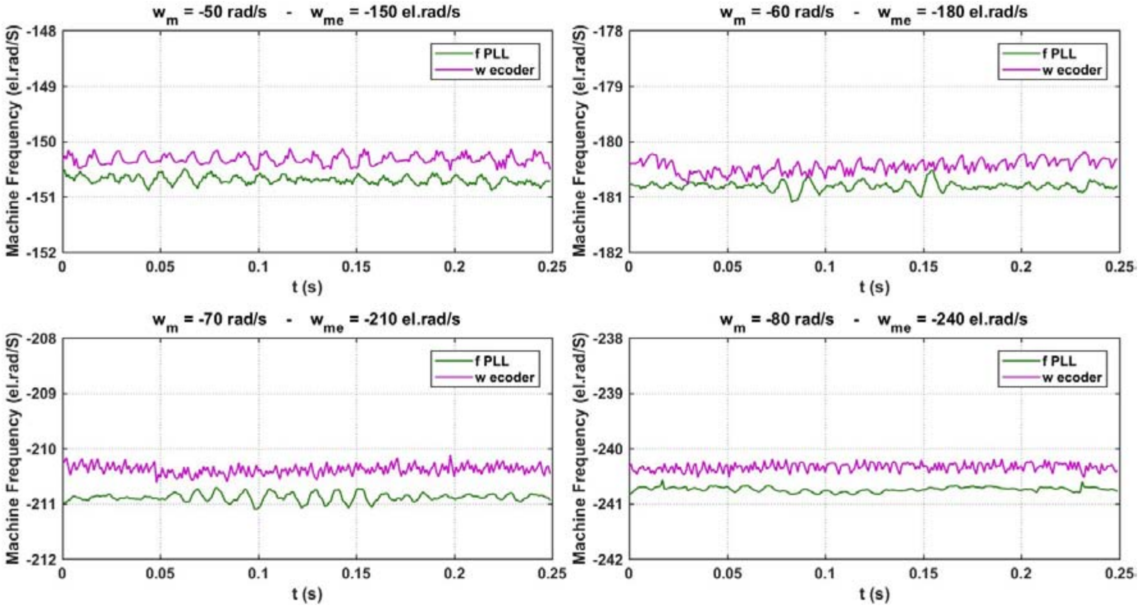
w_m = -50 rad/s - w_{me} = -150 el.rad/s

w_m = -60 rad/s - w_{me} = -180 el.rad/s

w_m = -70 rad/s - w_{me} = -210 el.rad/s

w_m = -80 rad/s - w_{me} = -240 el.rad/s

Figure 4.22 *- Comparison between the speed coming from the encoder and the speed extracted by the implemented in the medium speed range.*

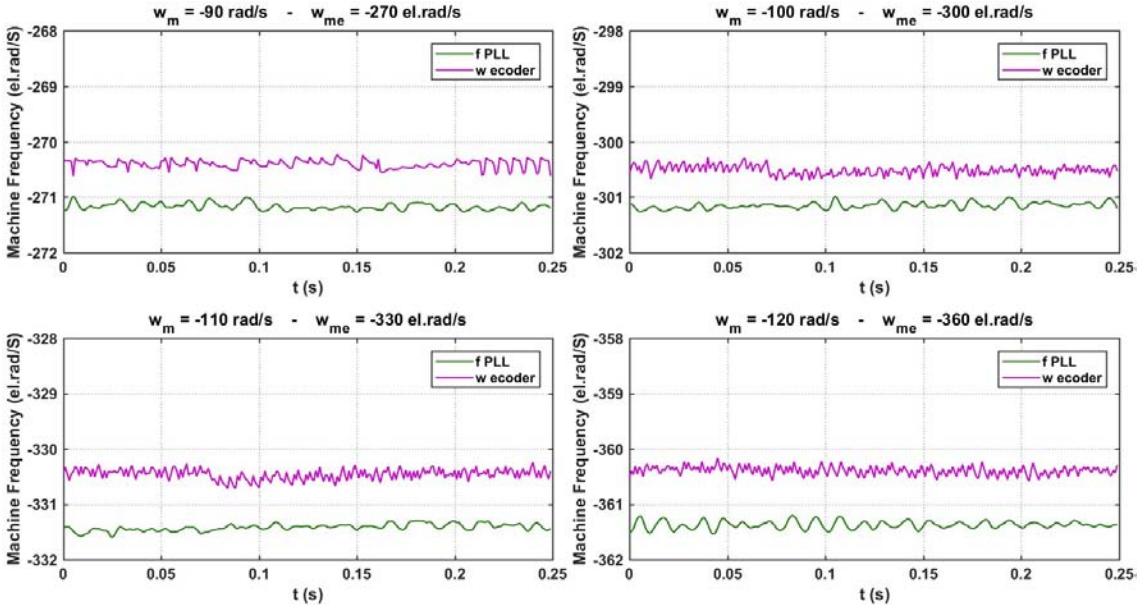

Figure 4.23 - *Comparison between the speed coming from the encoder and the speed extracted by the implemented script in the high speed range.*

In all the situations illustrated above the obtained frequency deviate from the encoder frequency of less then 0.4%. Since the encoder speed information is considered a real good estimation of the machine speed, the very little variation from this last one means that the obtained results are good.

The comparison between the estimated angle, `theta_PLL[N]`, and the angle provided by the encoder, `phase_rotor[N]`, is reported in the Figure 4.24, Figure 4.25 and Figure 4.26.

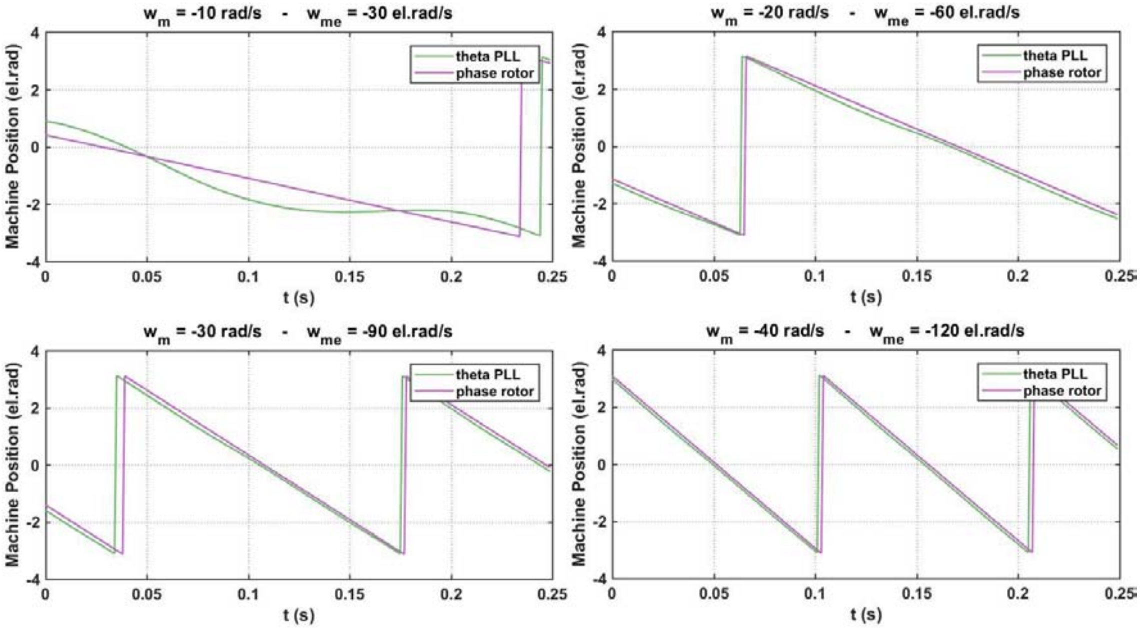

Figure 4.24 - *Comparison between the estimated angle and the angle provided by the encoder in the low speed range.*

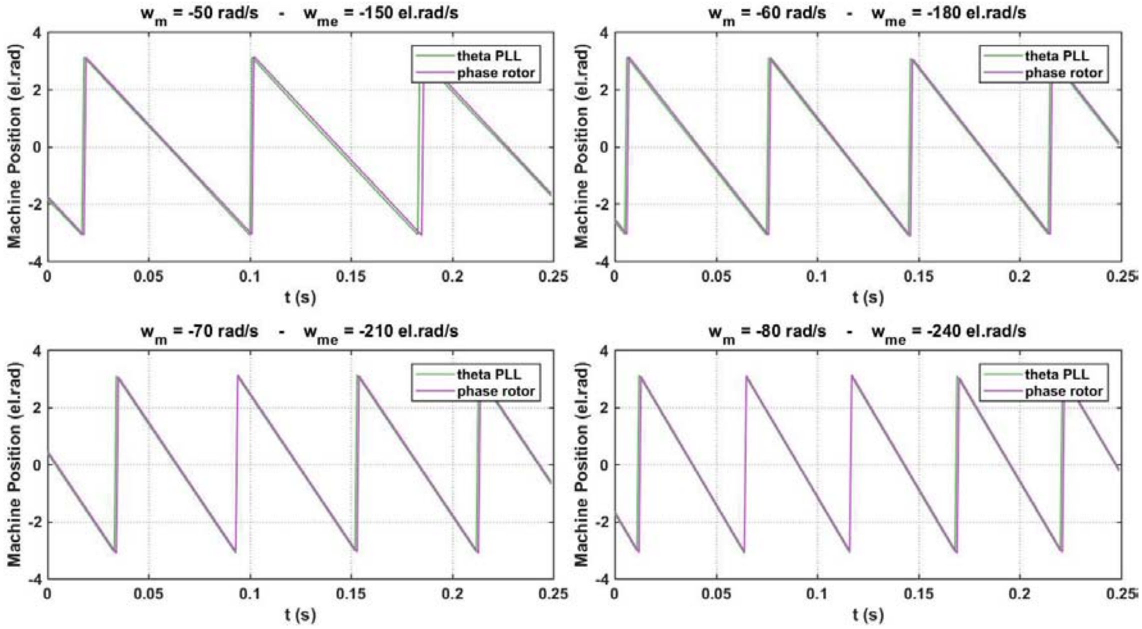

Figure 4.25 *- Comparison between the estimated angle and the angle provided by the encoder in the medium speed range.*

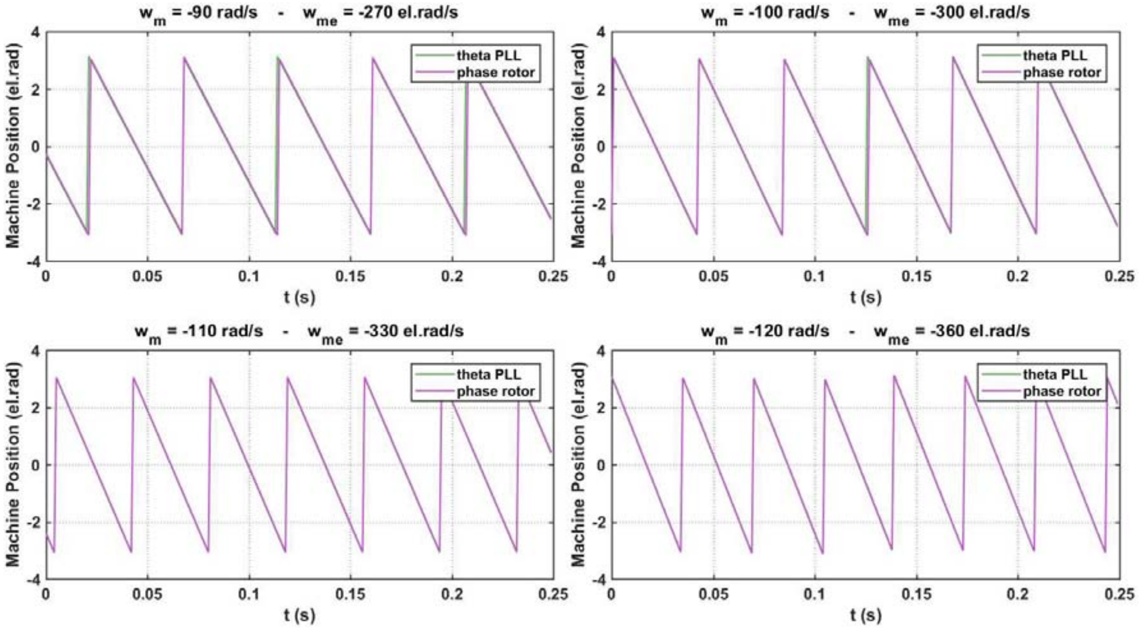

Figure 4.26 *- Comparison between the estimated angle and the angle provided by the encoder in the high speed range.*

As can be noticed, with the increasing of the speed the two signals overlap more and more, pointing out, one more time, that this estimation method works well over a certain level of low speed. To better understand the extent of the difference between the two machine angle position information is shown the phase shift between them in the next figures. As in the case of the Simulink simulation, a good result correspond to a phase displacement between $\pm 10^{el.\circ}$.

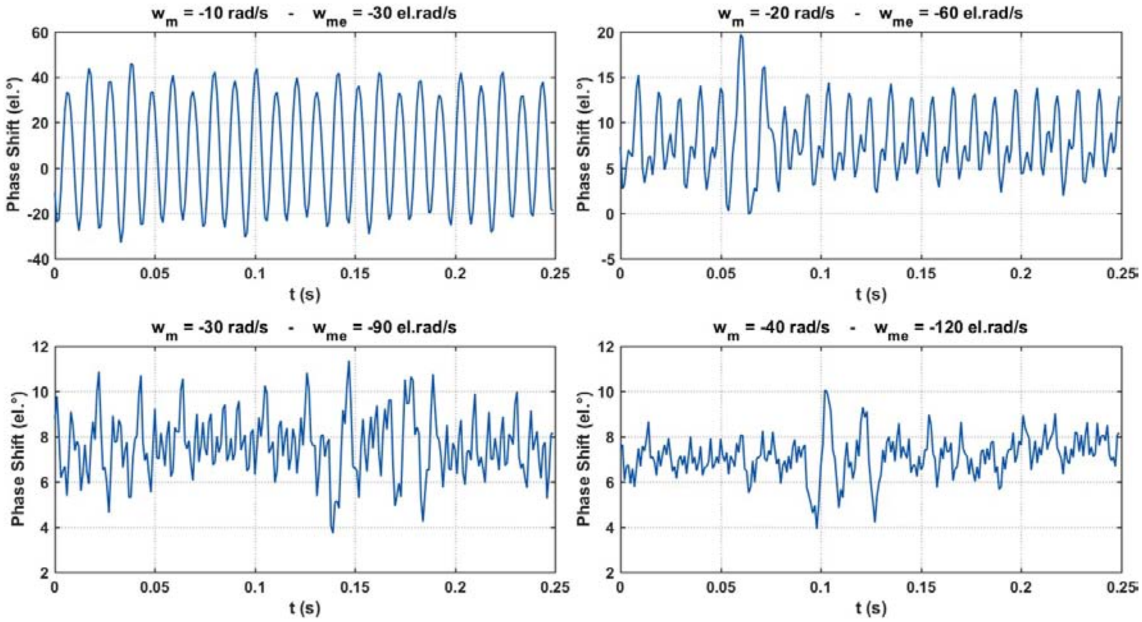

__Figure 4.27__ - Phase shift between the estimated rotor angle and the rotor angle given by the encoder in the low speed range.

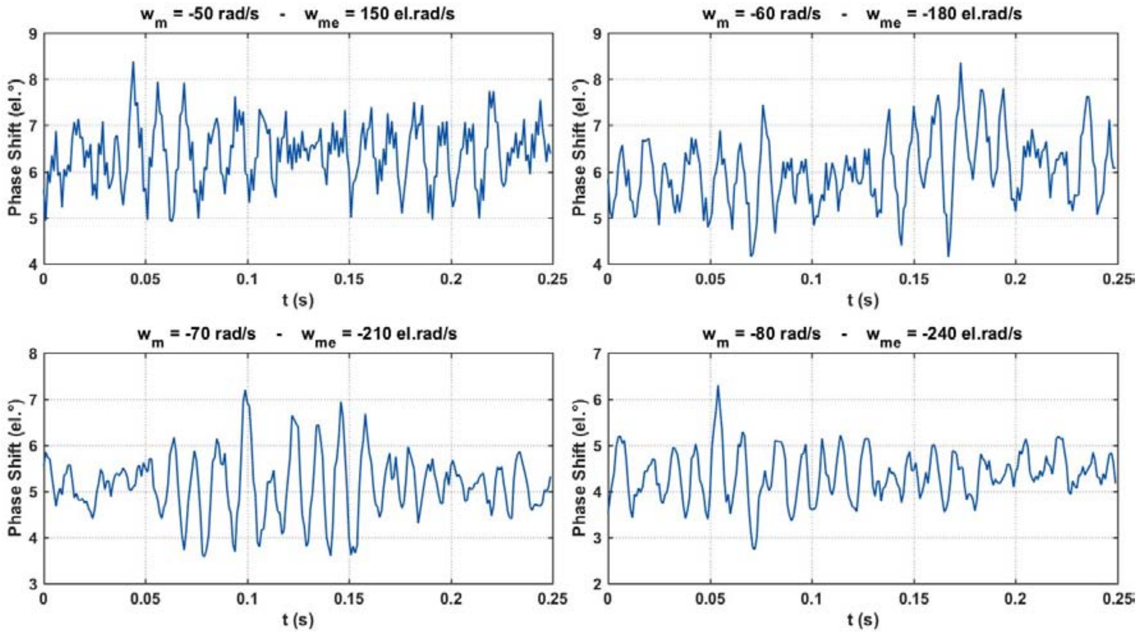

__Figure 4.28__ - Phase shift between the estimated rotor angle and the rotor angle given by the encoder in the medium speed range.

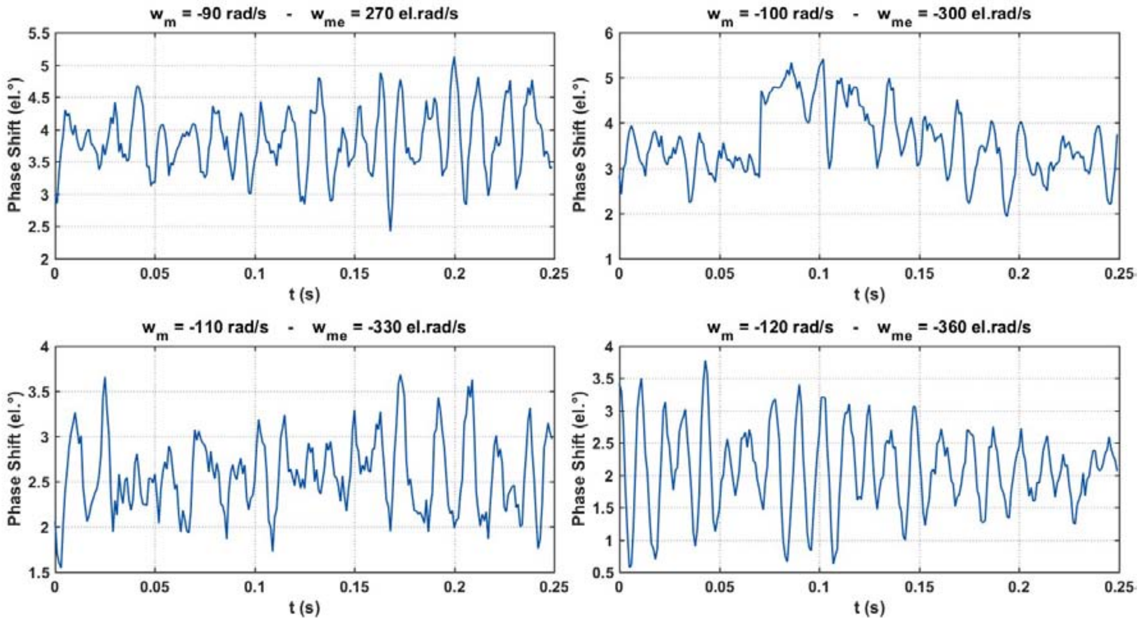

Figure 4.29 - *Phase shift between the estimated rotor angle and the rotor angle given by the encoder in the high speed range.*

If for the speed estimation a good result has been reached already at $-20\ rad/s$, for the position estimation this data should be shift to $-40\ rad/s$, because at this speed the thresholds set are not surmounted at all. In practice, the results can be accepted as good result starting from $-30\ rad/s$.

At last, on the following figures is shown the behaviour of the frequency/position detection model developed on this thesis work at the transients. Are analysed three speed steps, as indicate the titles of the figures below. For each step corresponds one figure because the data memory available on the DSP was not enough large to allow to save the necessary data for more then one step at a time.

First are shown the speed results, with the indication of the signal coming from the Encoder and the signal coming from the developed model, and then the phase shift between the angle position relative of the two frequency signals.

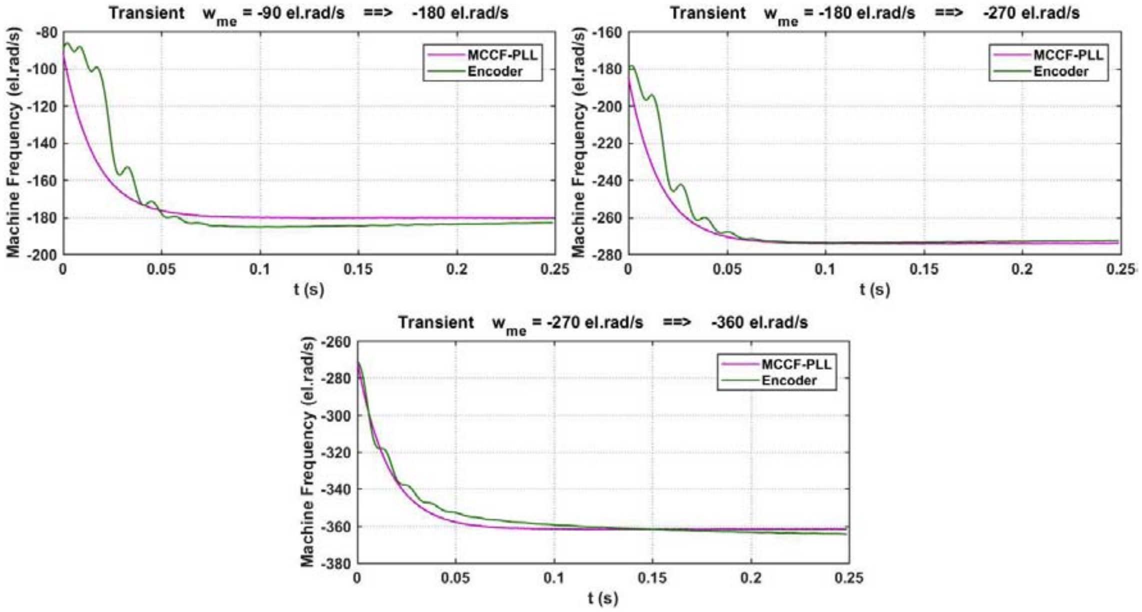

Figure 4.30 *- Increasing estimated and encoder speed steps in transient mode.*

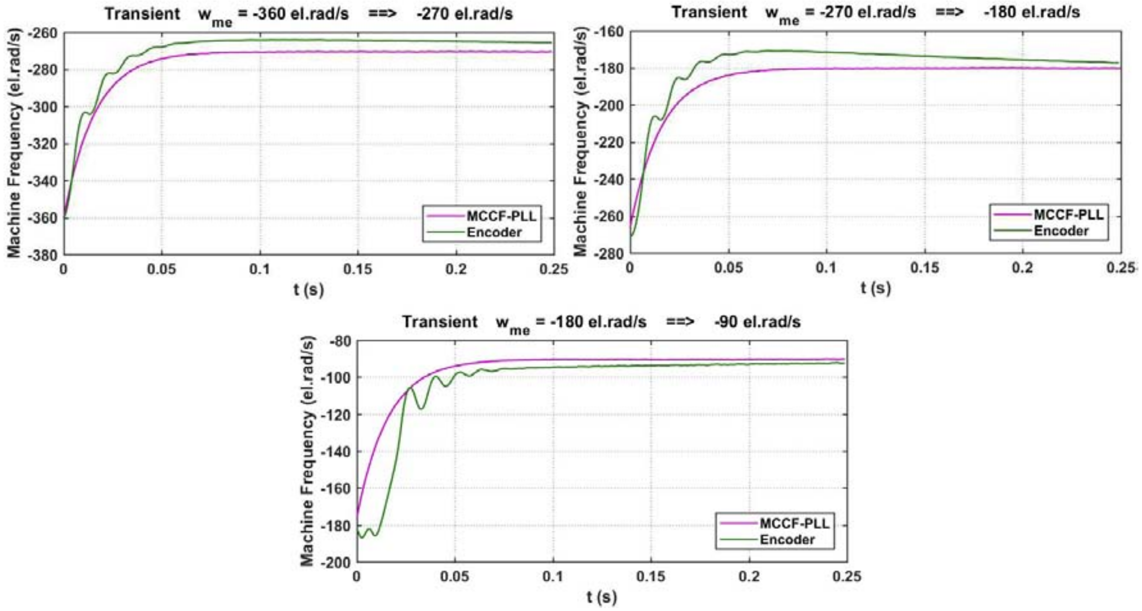

Figure 4.34.4-1 *- Decreasing estimated and encoder speed steps in transient mode.*

Is possible to see that the estimated speed follow properly the one given by the encoder, that is another confirmation of the quality of the system Multi-Complex Coefficient-Filter SFR-PLL.

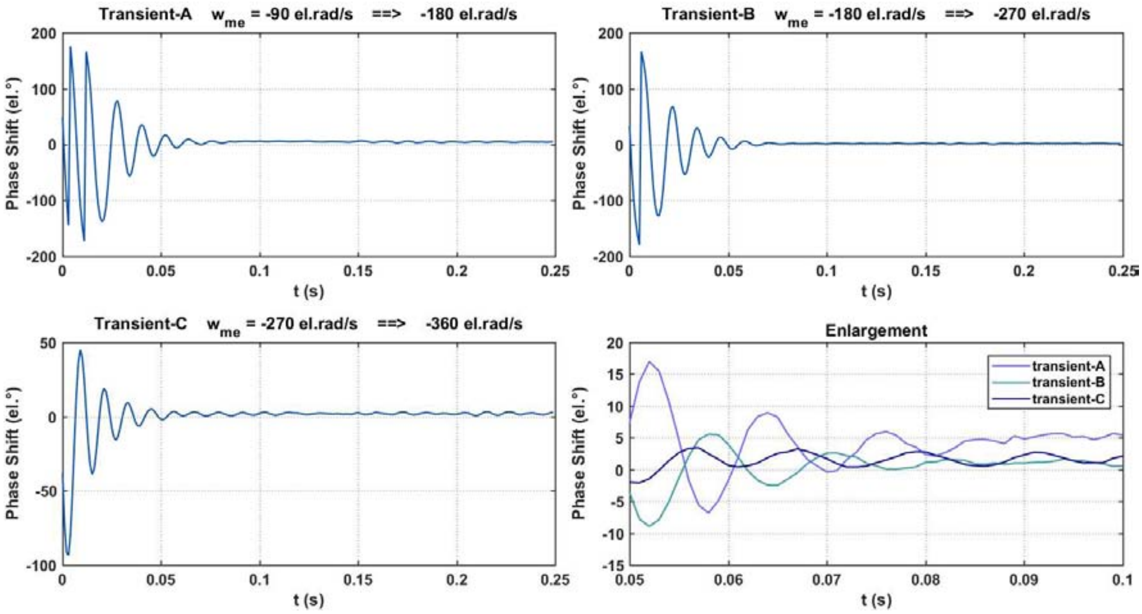

Figure 4.32 *- Phase shift in transient mode for increasing speed values.*

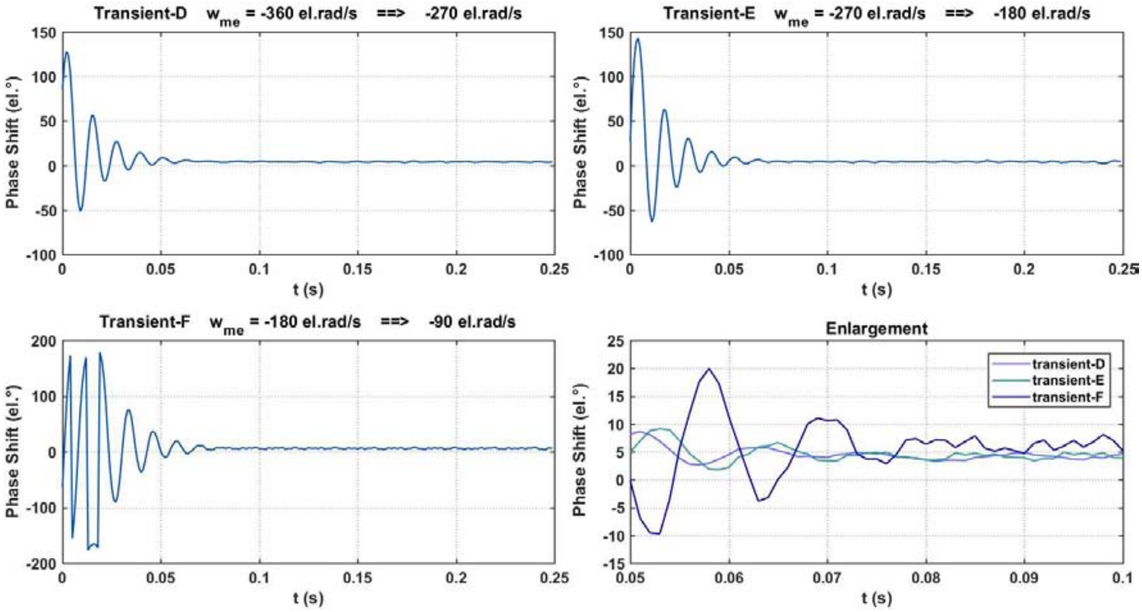

Figure 4.33 *- Phase shift in transient mode for decreasing speed values.*

The last two figures show that after an initial short oscillation, the phase shift between the estimated angle and the angle provided by the encoder is contained between the threshold of $\pm 10^{\text{el.}\circ}$. This is the last prove of the good quality of the method here adopted.

CHAPTER 5

COMPARISON BETWEEN SIMULATIONS AND PRACTICAL ECPERIMENTATIONS

In the light of the obtained results, the method has been checked working properly in both simulation and practical setting. The two differ mainly on the speed range profile utilized and on the fact that on the Simulink simulation are not present all those external and real factors that can influence the results as electromagnetic noise, vibrations, mechanical coupling, working temperature and worming-up of the machine and of the magnets, signals transmission, conditioning and elaboration and so on. Despite all of this, the MCCF SRF PLL has been proven as a good method to estimate frequency and position of the machine in both the situations, after the start of the machine.

In this chapter is point out the harmonic analysis of the two settings to compare them. Before this, for a better comparison, the Simulink model has been run with a speed profile that follow the values utilized on the Practical setting for the harmonic analysis:

$0\,rad/sec - 90\,rad/sec - 270\,rad/sec - 180\,rad/sec$

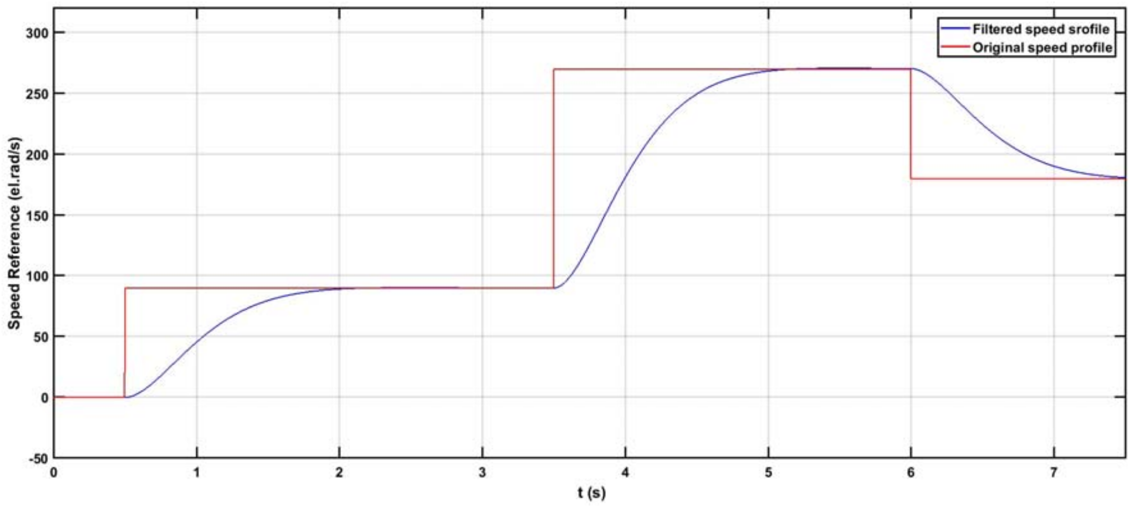

Figure 5.1 *- Speed reference profile.*

Are firstly shown the more relevant results of the Simulink simulation with new speed references. They have the same behaviour of the results shown in §3 for the first speed profile, with only a slight decrease of performances due to the lower speed. At first are illustrated the back-EMF components obtained after Clarke transformation from the three Hall signals, e_alpha_H and e_beta_H, in Figure 5.2, and the fundamental positive alpha and beta components of them at 90 $el.rad/s$ and at 270 $el.rad/s$.

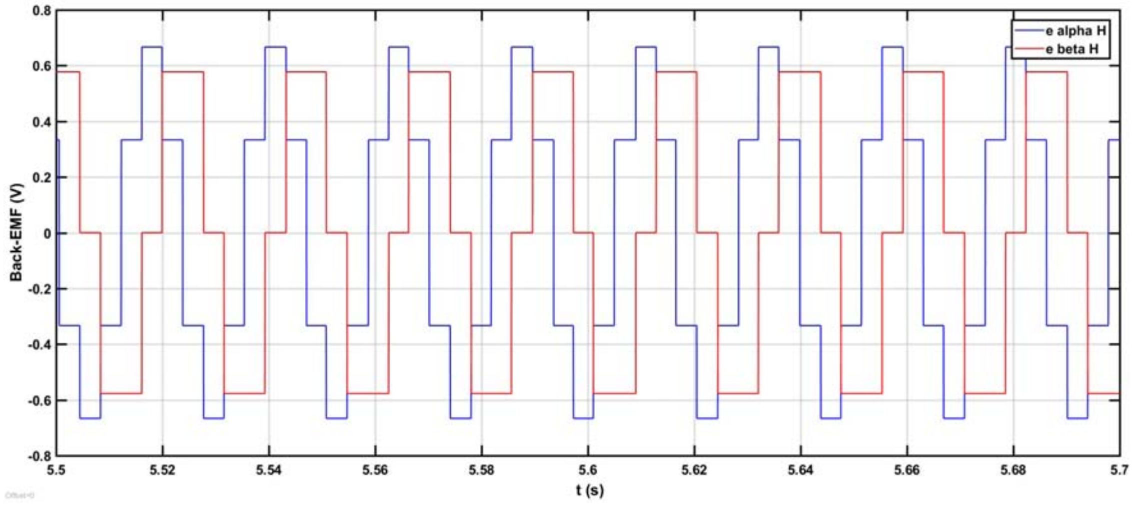

Figure 5.2 *- Back-EMF alpha and beta components.*

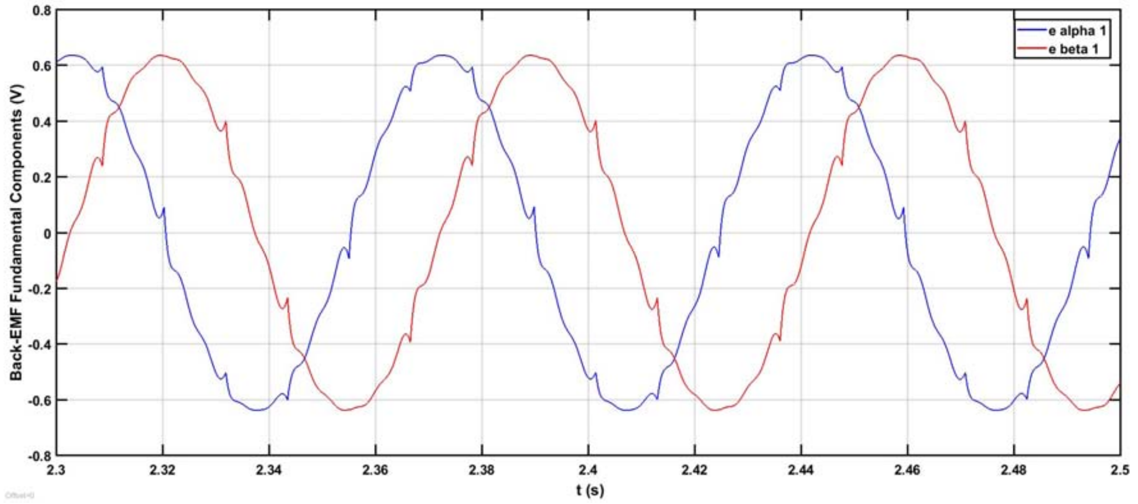

Figure 5.3 *- Fundamental back-EMF components at* $\omega_{me} = 90 el.rad/s$.

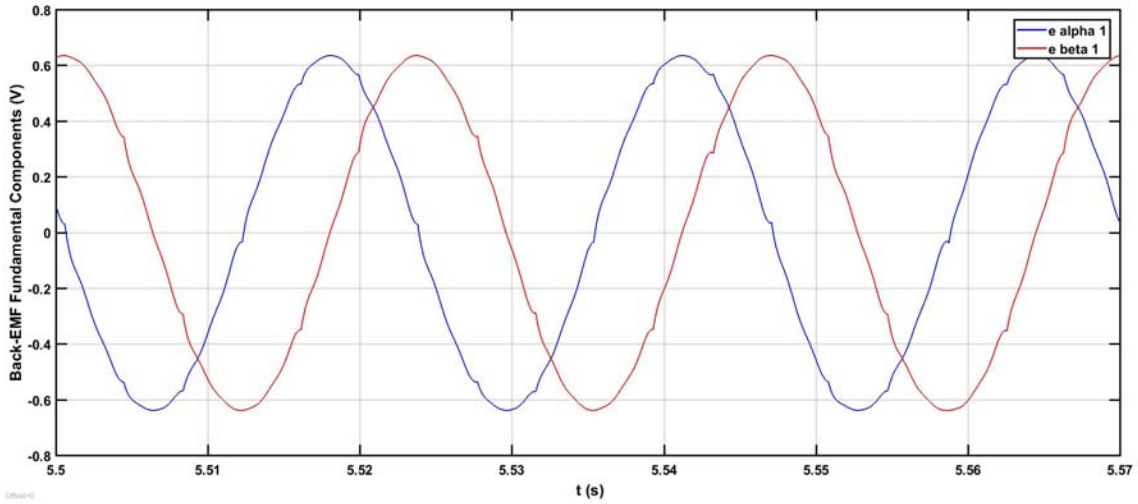

Figure 5.4 *- Fundamental back-EMF components at* $\omega_{me} = 270 el.rad/s$.

Can be notice that if the Figure 5.4 is really similar to Figure 3.35, the first one point put an higher harmonic component. This is caused by the worse angle estimation on the MCCF PLL due to the slow speed of the machine and the Hall-effect sensors resolution. Are shown below the comparison between the signals e_alpha_H, e_alpha_1, the alpha output of the check scheme of Figure 3.36. and the e_beta_H, e_beta_1, the beta output of the check scheme block.

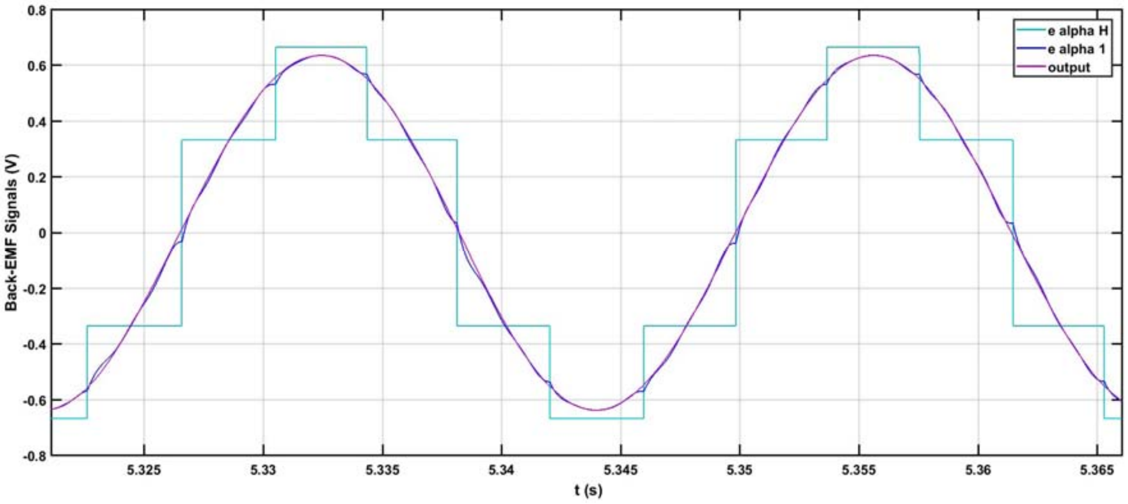

Figure 5.5 *- Alpha signals comparison.*

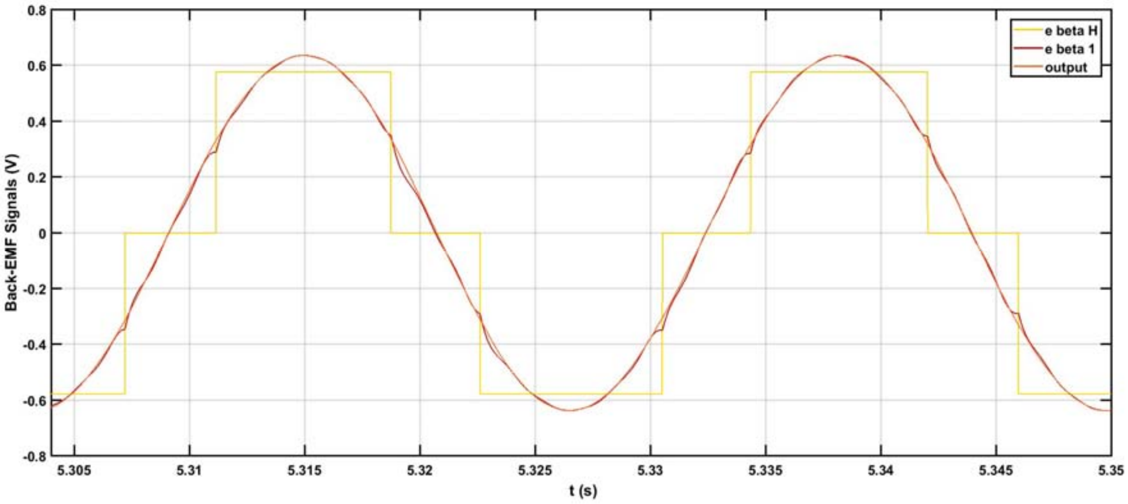

Figure 5.6 *- Beta signals comparison.*

The three signals are correctly in phase and submit to the amplitude ratio indorsing the correct working of the *POSITION DETECTION BLOCK*.

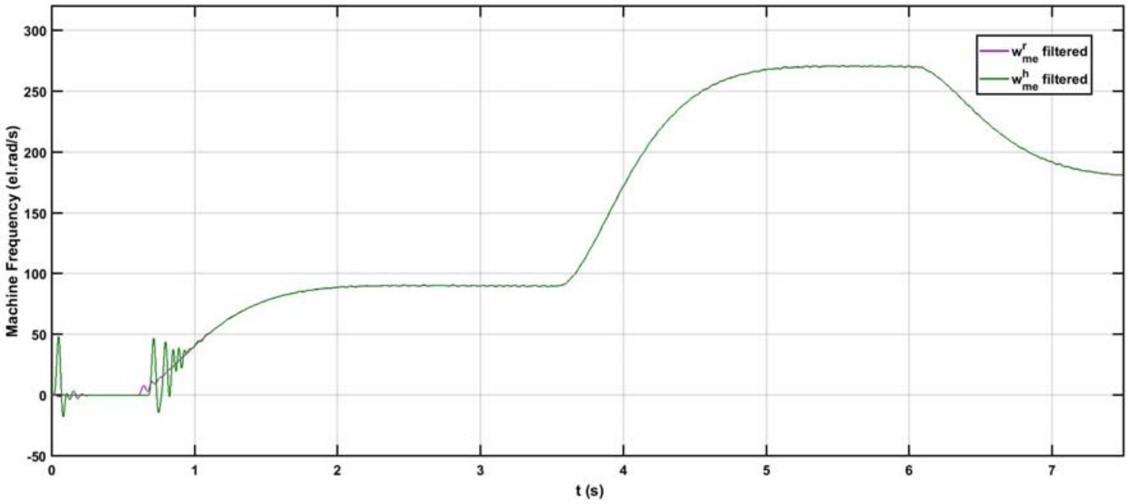

Figure 5.7 *- Filtered estimated and real machine frequency.*

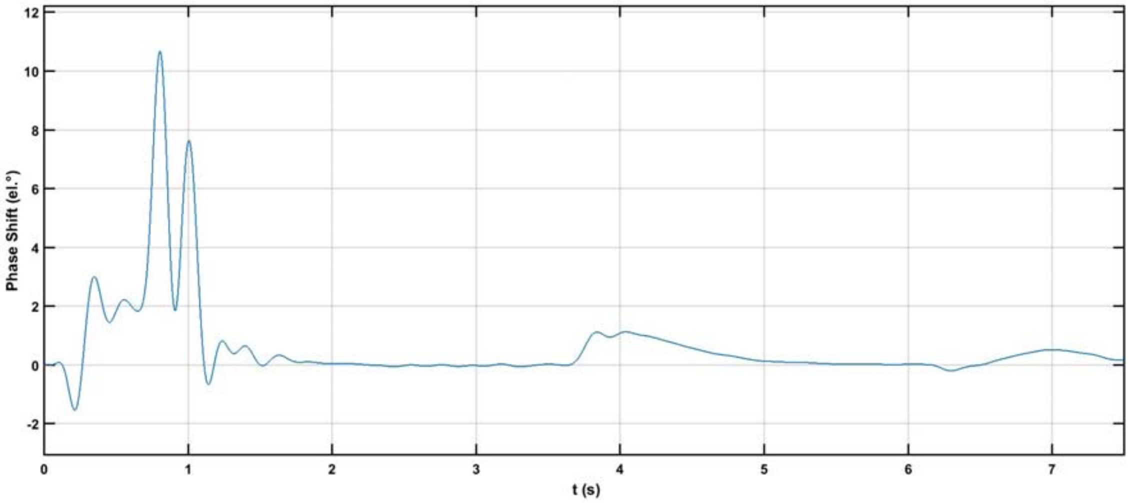

Figure 5.8 *- Phase shift plot.*

The Figure 5.7 shows as the machine frequency is well estimated, even if are present some more oscillations on the initial part, compered to Figure 3.33, because of the already mentioned limitations of the sensors. The phase shift graph, between the extracted angle θ^h_{me} and the one given by the model θ^r_{me}, displays the same trend of the one in Figure 3.31, with an exceeding of the positive threshold before to achieve really good values. Can be seen that on the flat part of the machine frequency in Figure 5.7 estimated with Simulink and of the CCS case in Figure 4.21÷4.23, the speed is never completely constant, but is always oscillate a little bit. This minimal oscillation are the cause of the not perfect numeric matching on the harmonic analysis figures. Anyway, for the magnitude of the differences, they can be neglected.

Now that the Simulink model has been verified working at the same speed profile of the practical experimentation, for the simulated and the practical case, the back-EMF signals in input of the MCCF stage and their harmonic components undergo to harmonic analysis. At this purpose the alpha and beta components of each signal are converted in a complex vector in turn processed by means of the Fast Fourier Transform implemented a MATLAB script. Must be clarified that, since the speed profile changes during the simulation, also the frequency of the signals does. To have a correct harmonic analysis of the signals, they must be analyzed when the speed is constant, and for the purpose it has been chosen the speed value of $\omega_{me} = \pm 270\ el.rad/s$ that allow the best visual results.

In the next figures will be marked on the *x*-axis the frequency of the fundamental and the harmonic components expected, instead on the plot there will be marked the frequency and the amplitude of the components obtained with the analysis.

To start, in Figure 5.9 and Figure 5.10, is represented the harmonic composition of the back-EMF signals obtained from the Hall-effect sensors that are respectively *e_alpha_H*, *e_beta_H* (in Figure 5.2) for the Simulink model and *E_abx_mccf.d*, *E_abx_mccf.q* (in Figure 4.19) for the CCS script.

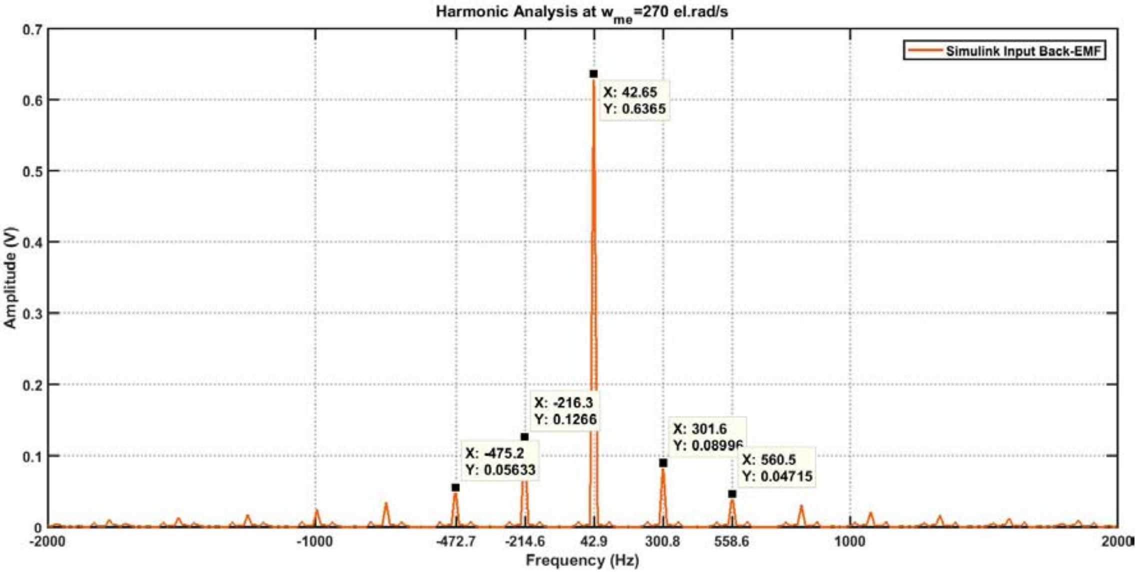

Figure 5.9 - *Simulink back-EMF harmonic composition.*

The figure above show as the values of frequency are almost coincident with the expected one seen the wavefrom of the input signals, and that the ratio between the fundamental and the -5^{th}, 7^{th}, -11^{th}, 13^{th}harmonic (the principal ones presented) is respected being the magnitude of these harmonic equal to $^1/_5$, $^1/_7$, , $^1/_{11}$, $^1/_{13}$, respectively of the fundamental amplitude. This good results, instead, are not reached in the case of the CCS Input signals, as shows the next figure.

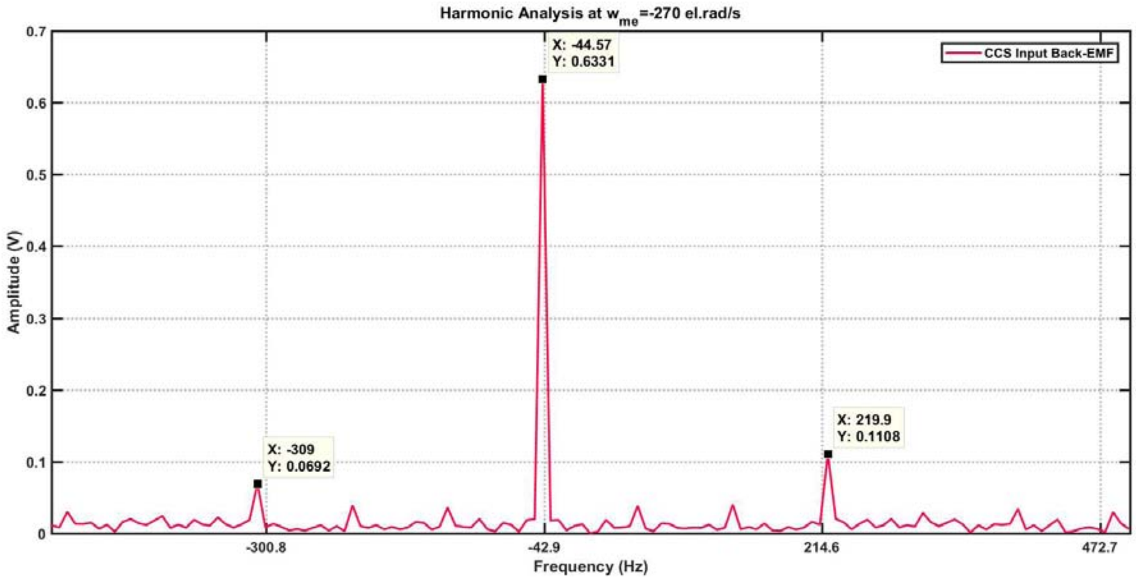

Figure 5.10 *- CCS back-EMF harmonic composition.*

Can be noticed as, from the frequency values to the amplitude ones, the harmonic analysis of the data saved by CCS are not really precise. This is not due to the not working of the system, as it has been proven to work properly on the previous chapter, but is a problem of data decimation. To be able to save two signals in the same time to have the same time reference, and to be able to compare them, it has been used for all the cases a sampling frequency of $1000\ Hz$, that combined with the little memory buffer available of 500 location in total, bring to save not enough information for a good harmonic analysis. Besides, as the Shannon Theorem says, for a correct signals reconstruction must be used a sample frequency larger then the double of the signals frequency. Can be easily seen that, for the machine sped considered on this picture of $-270\ el.rad/s$, the -11^{th} and 13^{th}harmonic has a frequency value of , respectively, $471.9\ Hz$ and $557.7\ Hz$, that does not respect this theorem, or is really close to the limit. To avoid this problem can be thought to analyze data for a lower speed value, but for lower speed the decimation effect is heavier. This wrong trend can be seen also on the next figures belonging of the CCS data.

The next two figures show the results of the harmonic analysis applied to the fundamental component, and as can be seen they are correctly obtained form the MCCF filtering stage.

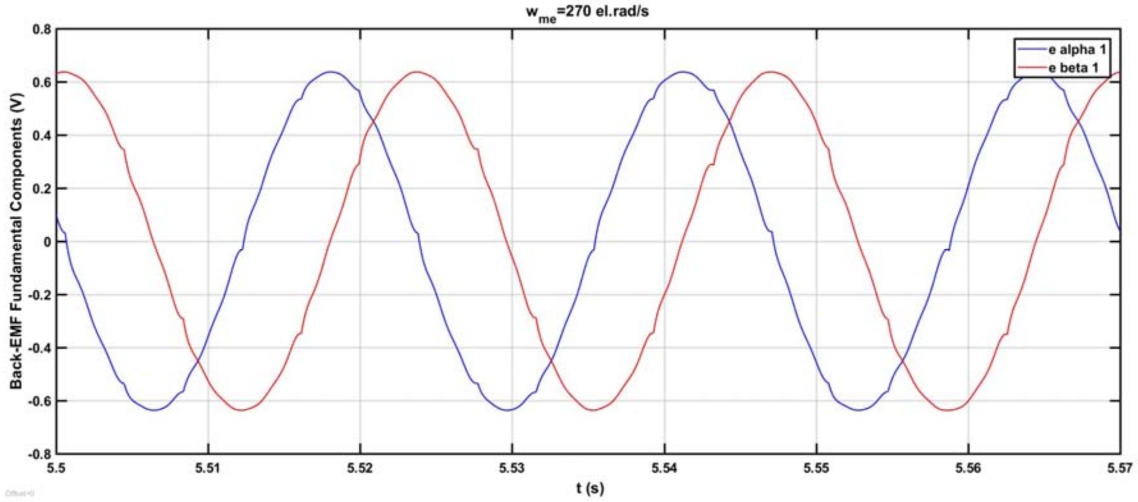

Figure 5.11 *- Back-EMF fundamental harmonic components at* $\omega_{me} = 270 el.rad/s$ *from Simulink simulations.*

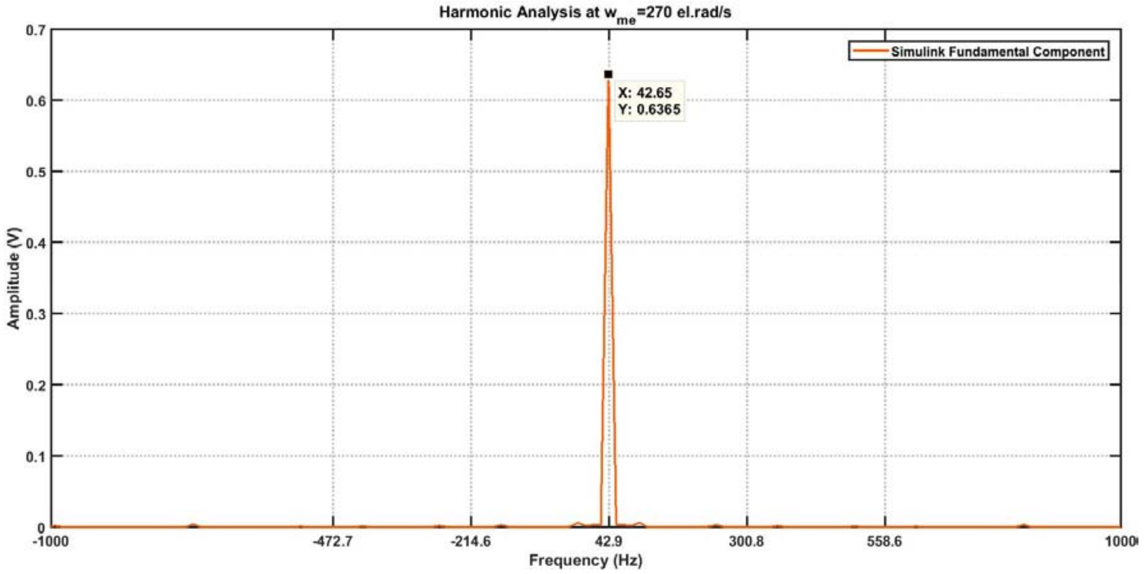

Figure 5.12 *- Harmonic analysis of the back-EMF fundamental harmonic components at* $\omega_{me} = 270 el.rad/s$ *from Simulink simulations.*

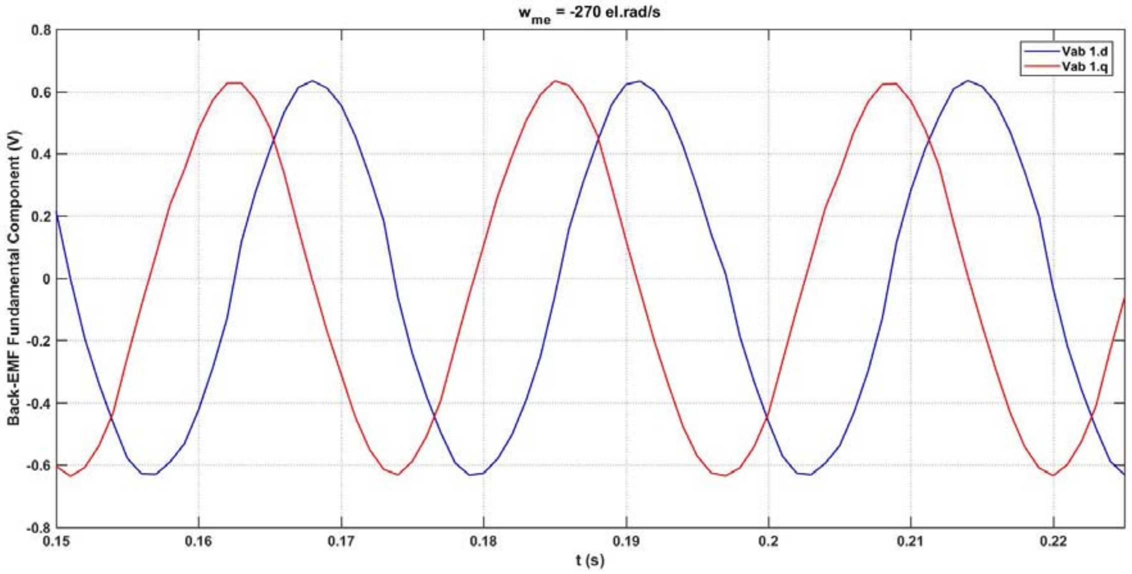

Figure 5.13 *- Back-EMF fundamental components at* $\omega_{me} = -270 el.rad/s$ *from CCS experimentations.*

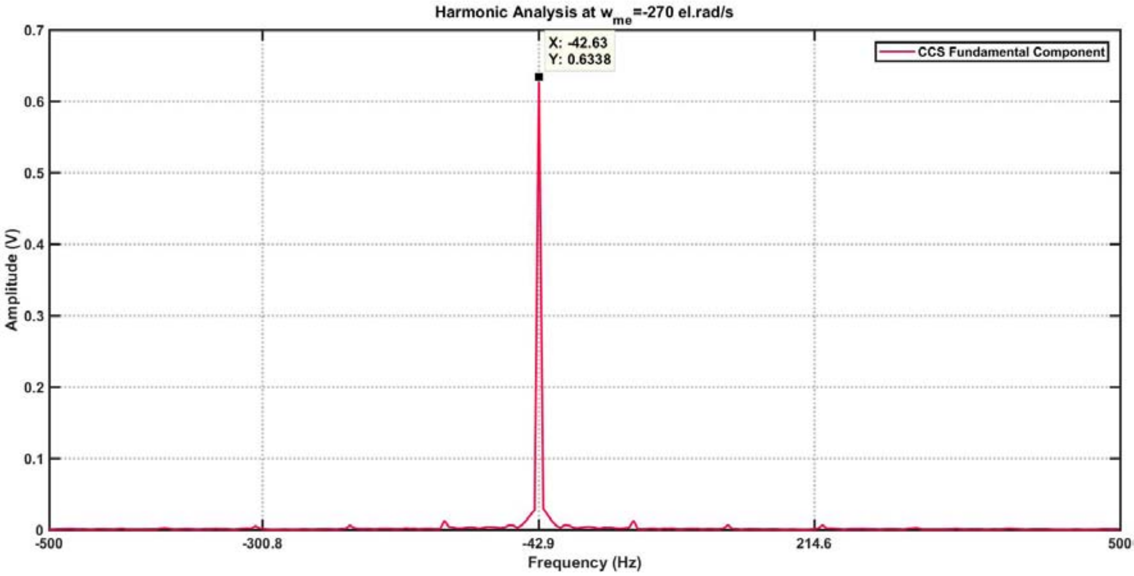

Figure 5.14 *- Harmonic analysis of the back-EMF fundamental components at* $\omega_{me} = -270 el.rad/s$ *from CCS experimentations.*

On the figures below will be represented the different harmonic component and their corresponding harmonic analysis, showing as in the case of the CCS script the decimation of the data does not allow to have a good representation of them. It start with the 7^{th} harmonic, also represented enlarged together with the fundamental component to show their sinusoidal waveform. The amplitude of the harmonics with the speed changes to reach the stable value when the speed is constant. The -5^{th}, -11^{th}, 13^{th} components follow.

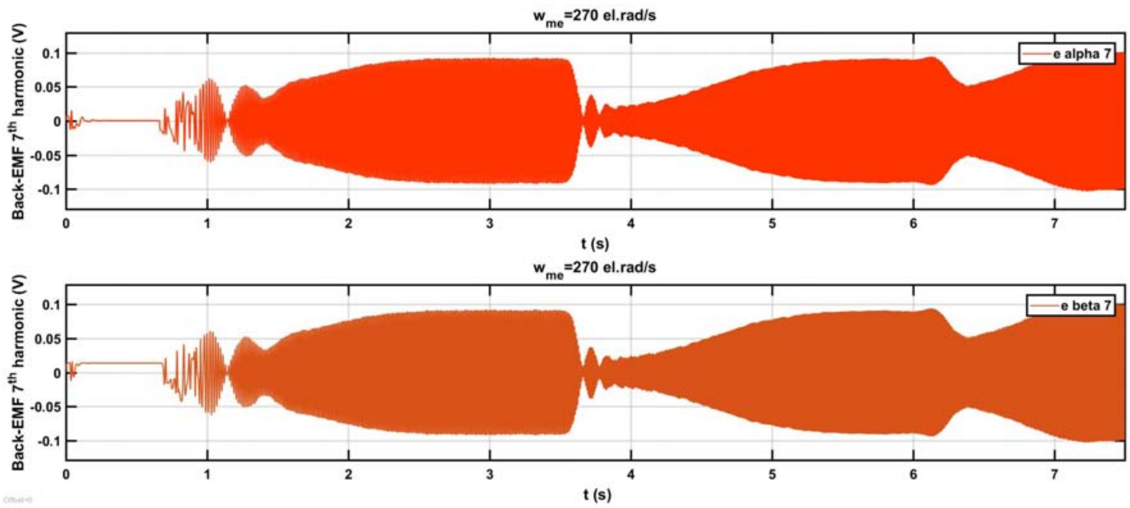

Figure 5.13 *- 7^{th} harmonic representations (alpha and beta) of the Simulink back-EMF signal.*

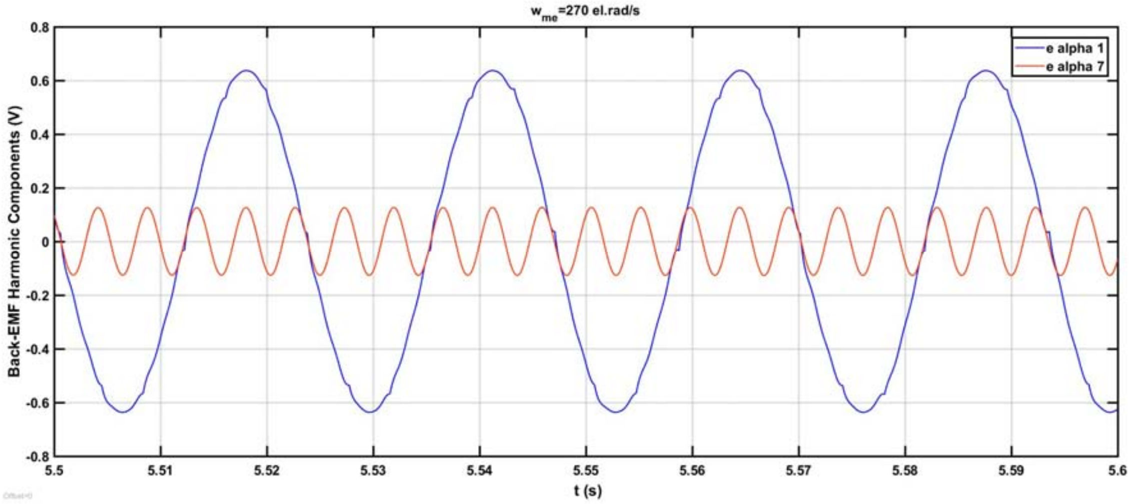

Figure 5.14 *- Comparison between the alpha component of the fundamental and 7^{th} harmonic components of the back-EMF from the Simulink simulation.*

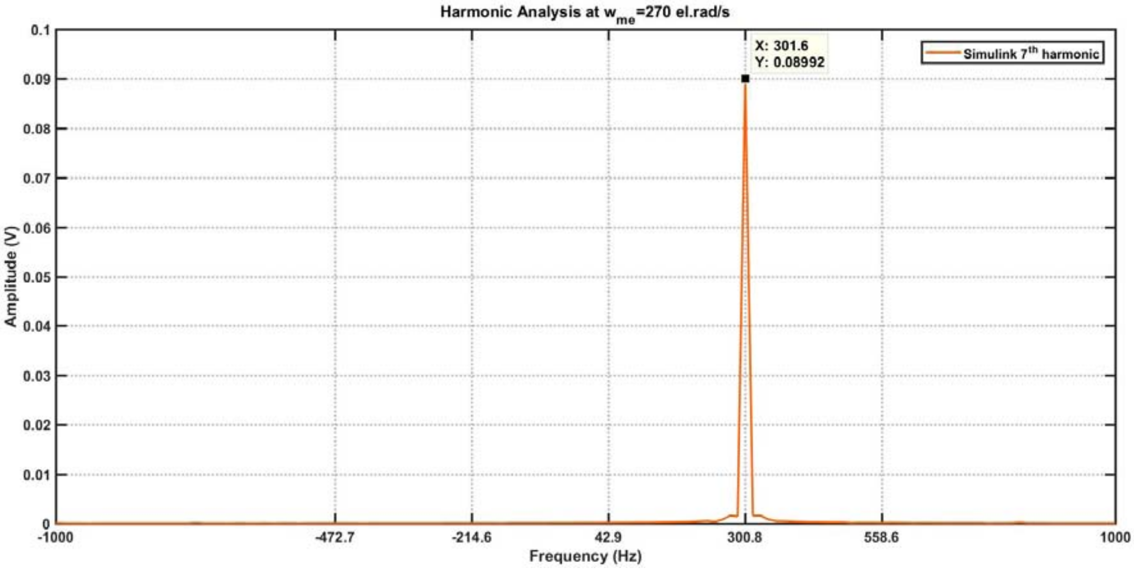

Figure 5.15 *- Harmonic analysis of the* 7^{th} *harmonic component of the back-EMF from the Simulink simulation.*

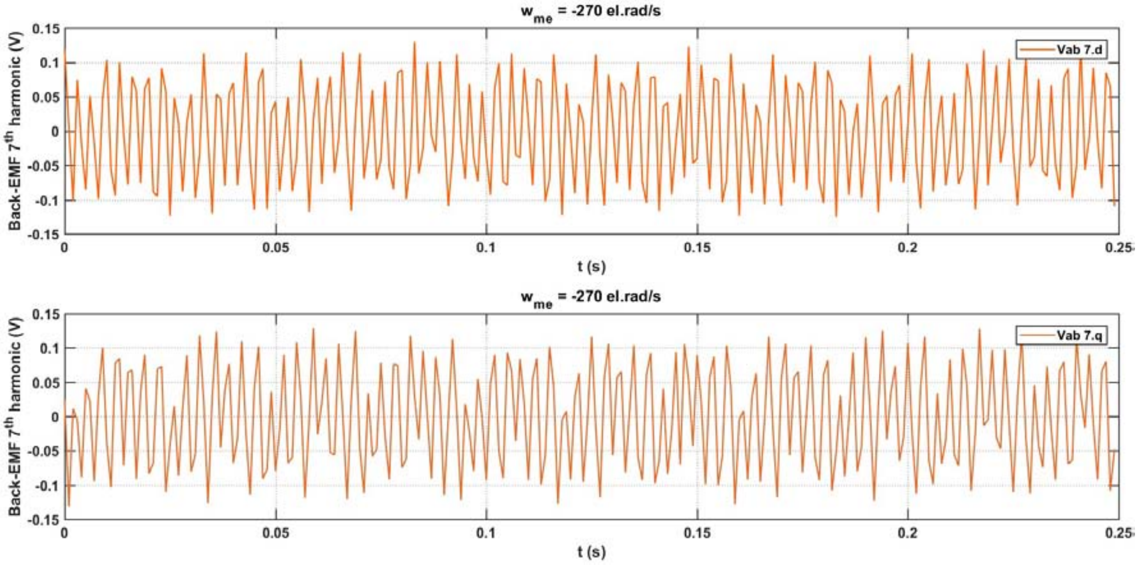

Figure 5.16 *-* 7^{th} *harmonic representations (alpha and beta) of the CCS back-EMF signal.*

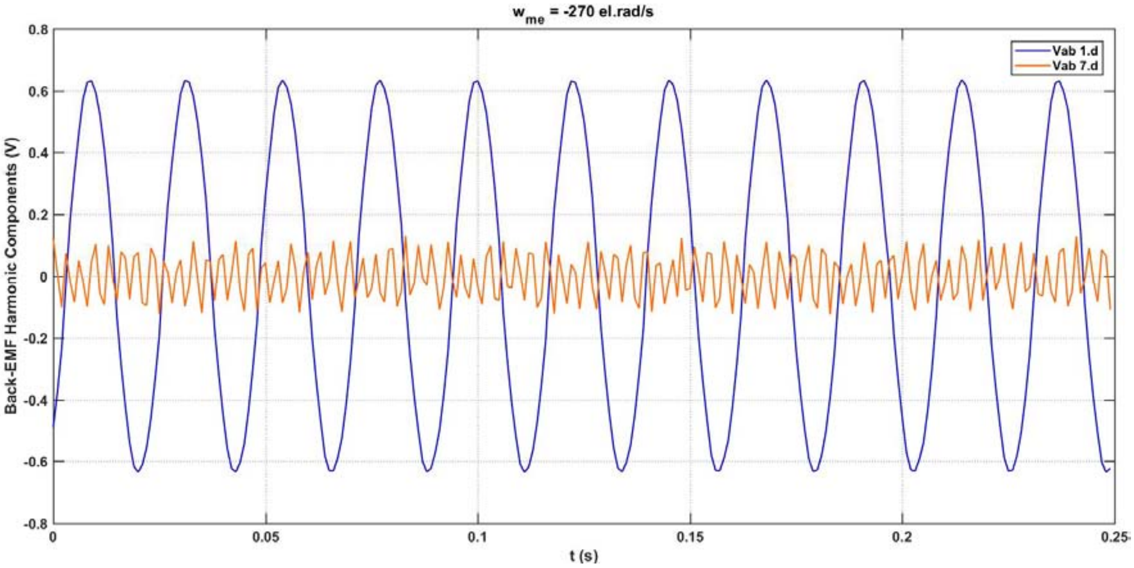

Figure 5.17 *- Comparison between the alpha component of the fundamental and* 7^{th} *harmonic components of the back-EMF from the CCS experimentations.*

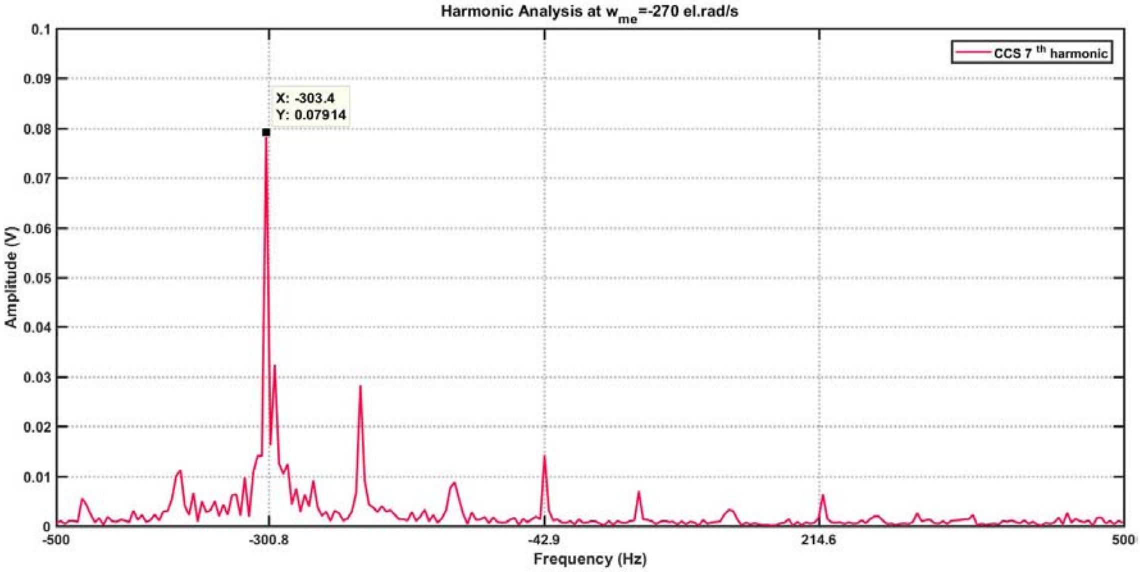

Figure 5.18 *- Harmonic analysis of the* 7^{th} *harmonic component of the back-EMF from the CCS experimentations.*

As can be seen, while for the Simulink figures the data are correctly represented, is not possible to say the same for the 7^{th} harmonic on the CCS Figures 5.16-5.17 due to lack of data saved. It is also not well estimated in amplitude: being $0.07914\ V$ against the $0.09054\ V$ expected.

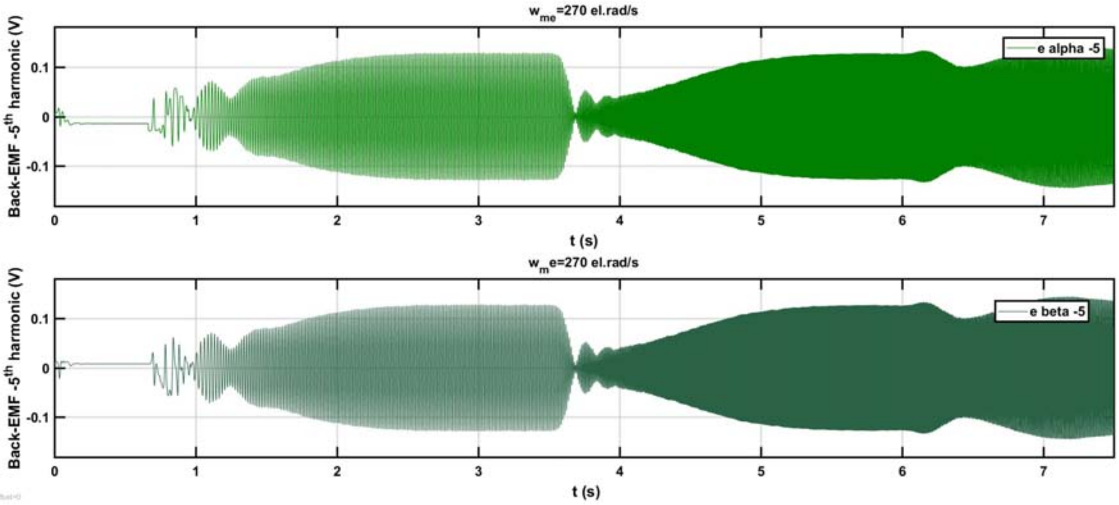

Figure 5.19 - -5^{th} *harmonic representations (alpha and beta) of the Simulink back-EMF signal.*

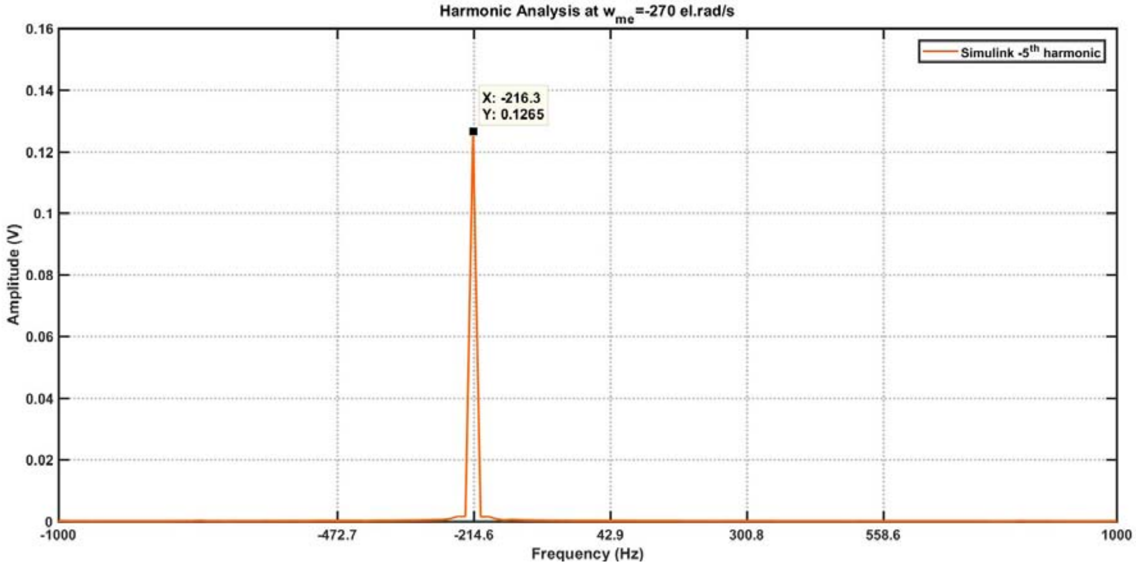

Figure 5.20 - *Harmonic analysis of the* -5^{th} *harmonic component of the back-EMF from the Simulink simulation.*

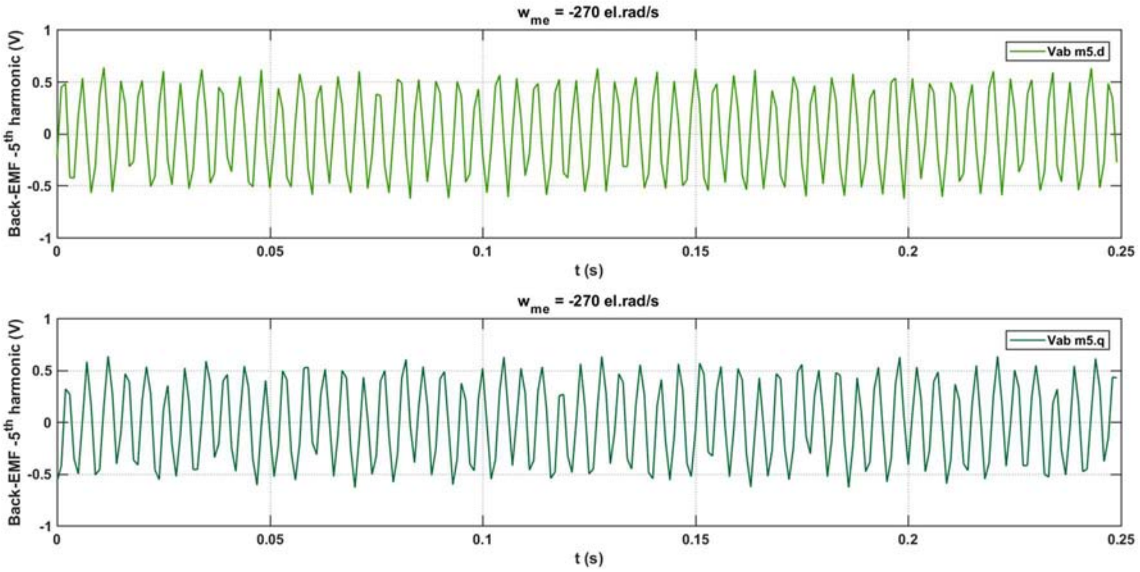

Figure 5.21 *-* -5^{th} *harmonic representations (alpha and beta) of the CCS back-EMF signal.*

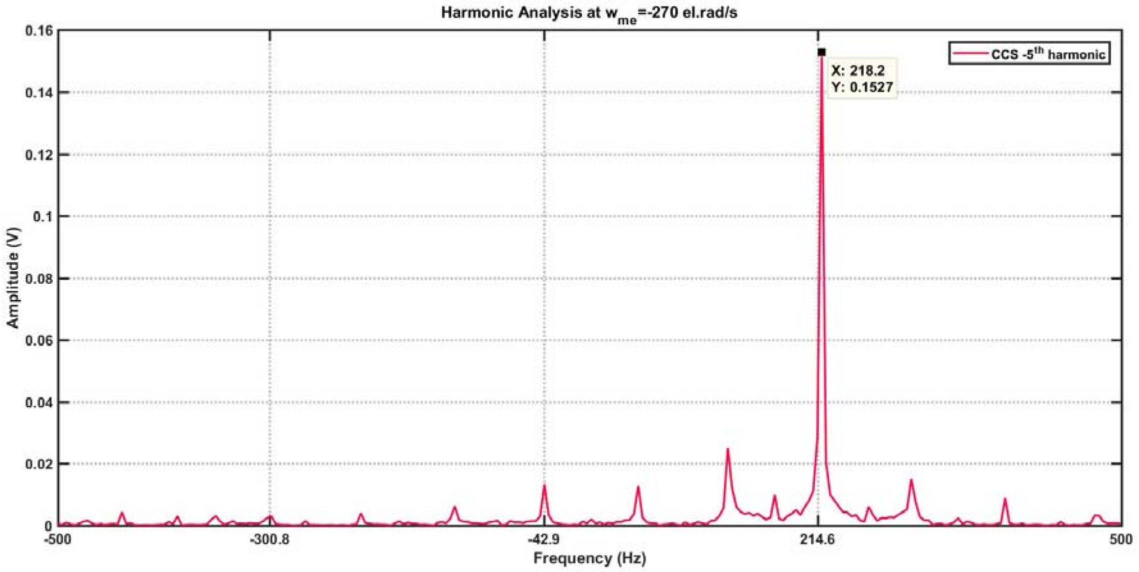

Figure 5.22 *-* *Harmonic analysis of the* -5^{th} *harmonic component of the back-EMF from the CCS experimentations.*

The same consideration of the 7^{th} harmonic can be done for the -5^{th} one regarding both frequency and amplitude values (expecting $0.1267\,V$ and obtaining $0.1527\,V$). The CCS signals are not even sinusoidal due to the lack of data saved. This effect is even more significant for the next components so that it is not possible to show their harmonic analysis.

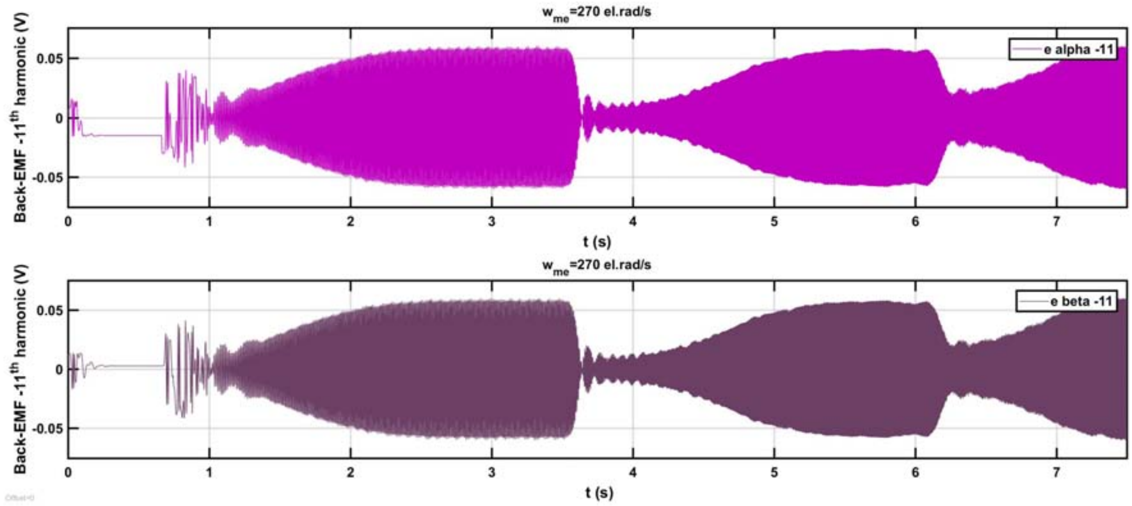

Figure 5.23 - *-11^{th} harmonic representations (alpha and beta) of the Simulink back-EMF signal.*

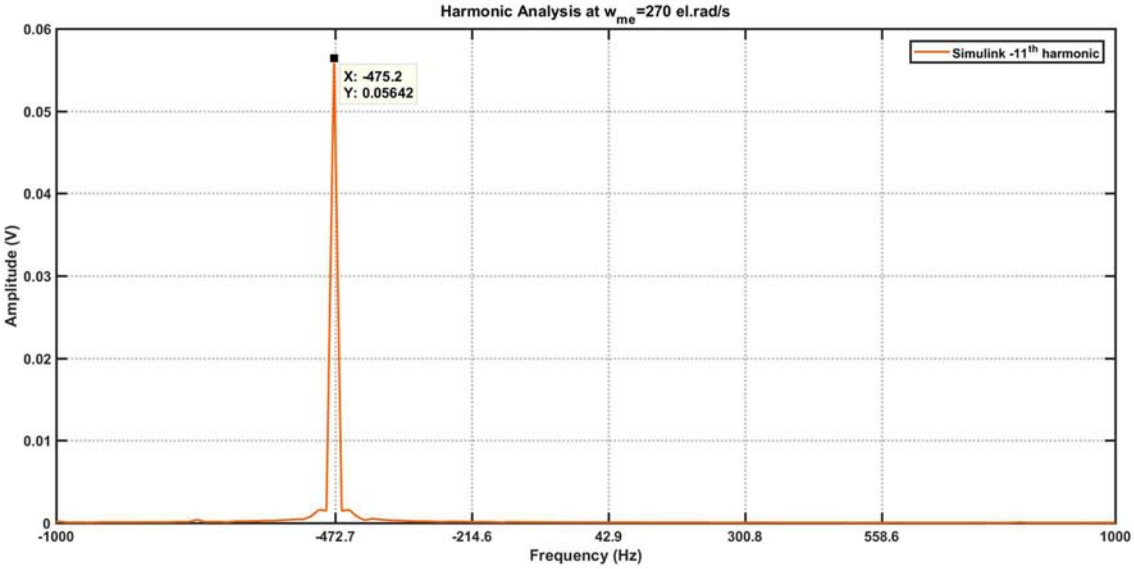

Figure 5.24 - *Harmonic analysis of the -11^{th} harmonic component of the back-EMF from the Simulink simulation.*

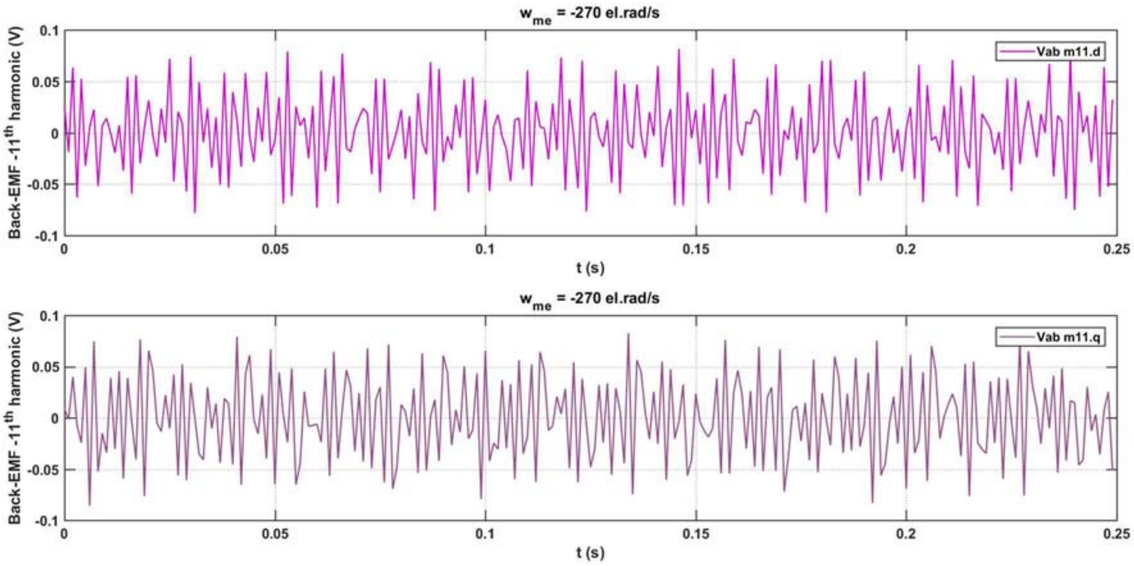

__Figure 5.25__ - -11^{th} harmonic representations (alpha and beta) of the CCS back-EMF signal.

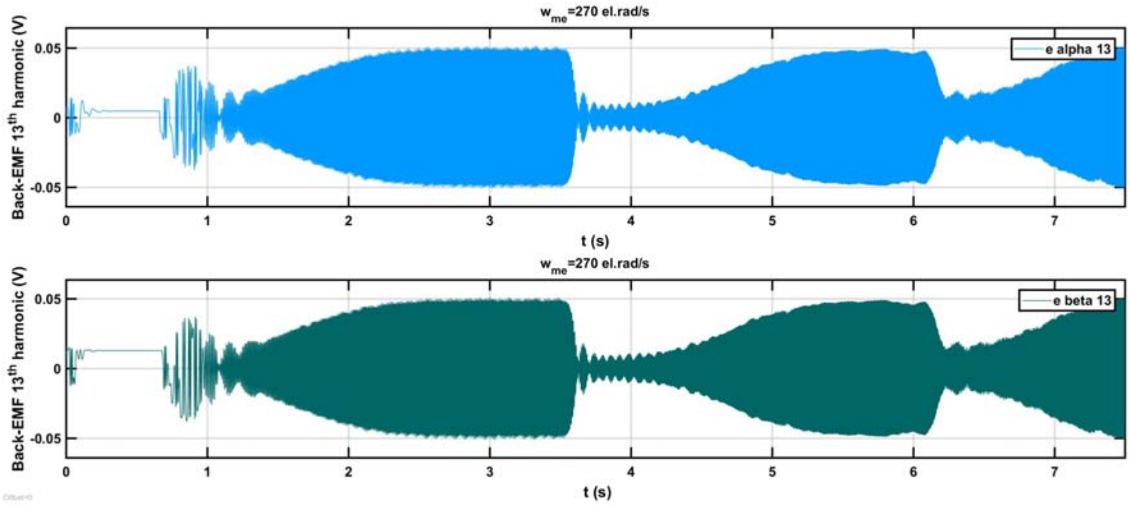

__Figure 5.26__ - 13^{th} harmonic representations (alpha and beta) of the Simulink back-EMF signal.

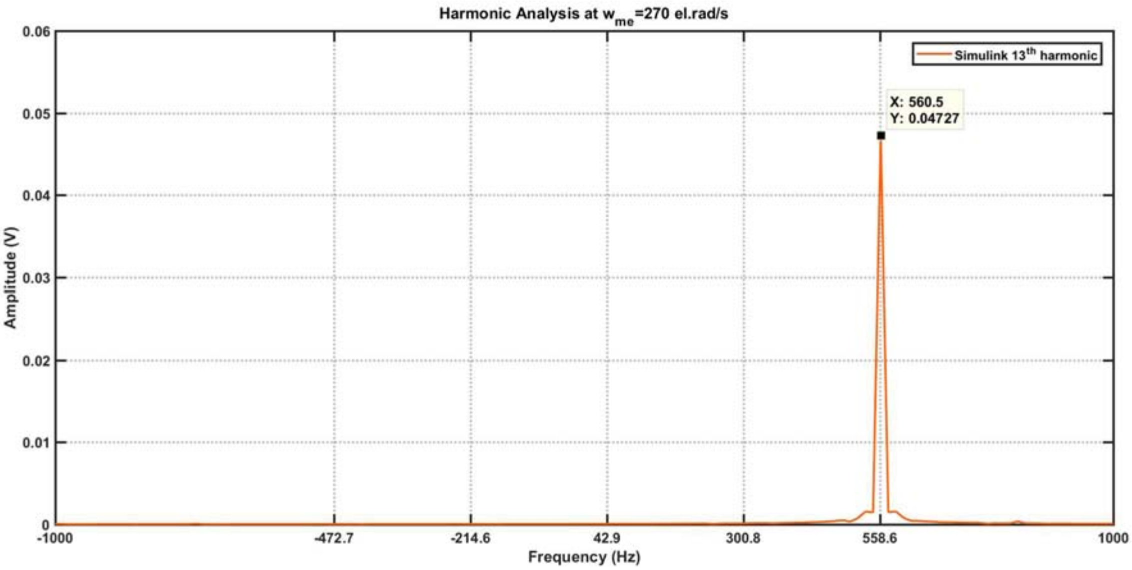

Figure 5.27 *- Harmonic analysis of the* 13^{th} *harmonic component of the back-EMF from the Simulink simulation.*

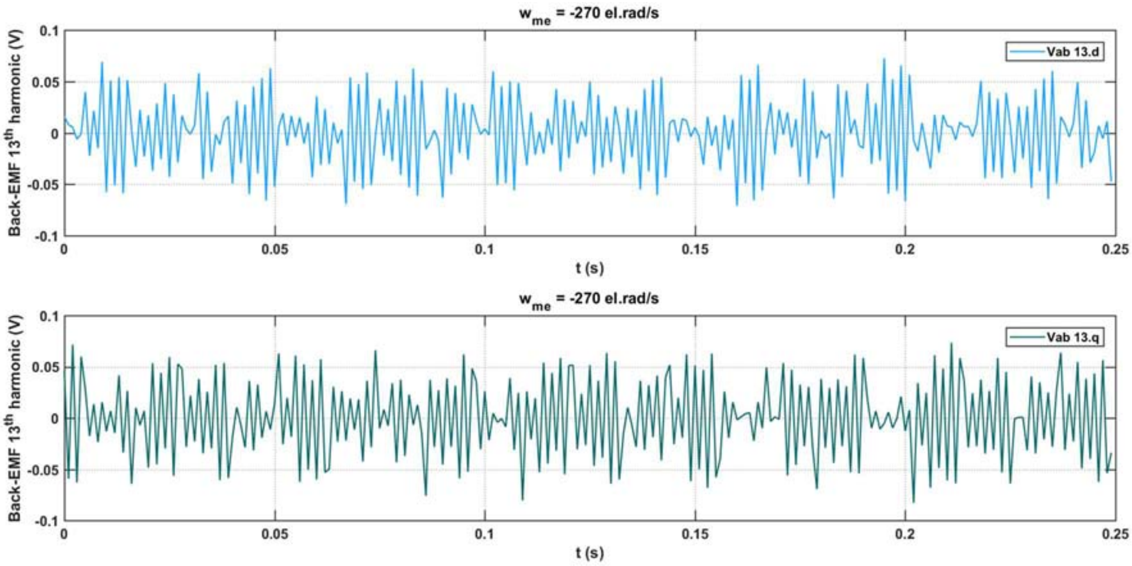

Figure 5.28 *-* 13^{th} *harmonic representations (alpha and beta) of the CCS back-EMF signal.*

CHAPTER 6

CONCLUSIONS

The aim of this thesis work was to find and test a system able to extract accurate frequency and position information of an IPMSM utilizing the Hall-effect sensors. It has been chosen to use these sensors because of their really low price, some cents of euro, compared to the most used encoder, that costs around 300 € typically. For this purpose it has been utilized a Multi-Complex Coefficient-Filter SRF-PLL, usually used in harmonic filtering in electric greed.

The Hall-effect sensors provide a discrete absolute-position information with $\pm 30^{el.\circ}$ resolution, with consequently a low resolution rotor angle feedback. Despite of this not really accurate information, it has been demonstrate in the §3.9 and §4.4, dedicated to the simulation and practical results, how the whole system work properly yielding a proper estimation of both speed and angle position of the IPM motor in a distorted environment robustly and quickly, and produces decoupled reference signals for the harmonic control, with an angular error lower than $\pm 10^{\mathrm{el.}\circ}$.

The good results obtained shown that the system here developed is a working method, even if, at the moment, there are some limitations on the pure application like:

- the start of the machine, that is affected by the low resolution of the Hall-effect sensors which does not allow to correctly estimate the back-EMF;

- the make use on real precise application, in which is required an angular error of zero value and that does not change with the change of speed.

6.1 Future Work

After this thesis work, more should be done to make this method all speed range applicable and close to the perfect working. To this purpose the following list suggest some points of work and some improvements needed.

- Increase data storage on the electronic control board interfacing the PC with the machines and the different converters. This can allow to save more data, and to not use the data decimation leading to more information available and better graphical results.
- Even if the magnitude of the Hall signals is not dependent from the speed of the motor, it has to be taken in consideration that speed control of the Induction Machine, that is coupled with the IPMSM, has been intentionally tuned with a low bandwidth in order to avoid the stress of the mechanical coupling. Thus, the speed control at low speeds makes that the speed oscillates affecting the speed estimation. Moreover, the Hall-effect sensors resolution does not allow to have enough information for start up the machine. The next target could be study a method to overtake this limitations and increase the range of the estimated speed.
- Another improvement can be done on the writing of the *BP_CCF_Vod/Voq* function of the CCS code. Since the DSPs utilized have not a floating-point unit, to represent the real numbers is used Q number format, that is a fixed point number format. This kind of representation is subject to some calculation errors due to approximations of numbers or mathematical operations, absorption, cancellation, overflow and so on. It has been discovered, reproducing with a MATLAB script the *BP_CCF_Vod/Voq* functions, that with the change of speed, the values of the coefficient present in them are not always correctly calculated. Even if the deviation is really low, and maybe negligible, it can affect the precision of the method and some deep examinations should be done.

APPENDIX

Discretization

When it is necessary to operate with a digital system, as in the case of the CCS code, is crucial to have a correct discrete time realization that allows to have the performance desired from the analog device in question (controllers, filters for example). The target of the discretization is determinate this discrete time realization and consists of a process of transforming mathematical models based on continuous equations in mathematical models based on discrete equations. The discretization methods are finite differences methods for the solution of differential equations derived from many methods for approximate integral calculations.

In this case is used the Tustin Method (Bilinear) that yields the best frequency-domain match between the continuous-time and discretized systems. Is usually used when is desired a good matching in the frequency domain between the continuous-time and discrete-time models and when the model has important dynamics at some particular frequency.

This method relates the *s*-domain(continous) and *z*-domain(discrete) transfer functions using the approximation (in first-order):

$$z = e^{sT_s} \approx \frac{1 + \frac{sT_s}{2}}{1 - \frac{sT_s}{2}} \qquad (A.1)$$

T_s is the sample time. For example, a continuous time linear controller is described by the transfer function

$$H(s) = \frac{U(s)}{E(s)} = \frac{b_m s^m + b_{m-1} s^{m-1} + \cdots b_0}{s^n + a_{n-1} s^{n-1} + \cdots a_0} \qquad (A.2)$$

which is equivalent to the input-output relationship

$$s^n U(s) + a_{n-1} s^{n-1} U(s) + \cdots a_0 U(s) = b_m s^m E(s) + b_{m-1} s^{m-1} E(s) + \cdots b_0 E(s) \qquad (A.3)$$

Replacing the operator s with its discrete approximate and the continuous quantities with the corresponding discrete, you get an approximate relationship between discrete quantities, which can be expressed in the form of a transfer function:

$$H_d(z) = \frac{\beta_m z^n + \beta_{m-1} z^{n-1} + \cdots \beta_0}{z^n + \alpha_{n-1} z^{n-1} + \cdots \alpha_0} \qquad (A.4)$$

which corresponds to the equation by finite differences

$$\bar{u}_{k+n} + \alpha_{n-1}\bar{u}_{k+n-1} + \cdots \alpha_0 \bar{u}_k = \beta_n e_{k+n} + \beta_{n-1} e_{k+n-1} + \cdots \beta_0 e_k \qquad (A.5)$$

The solution $\bar{u}_k$must approximate the sampling u_k of the solution $u(t)$ of the (A.5) being $e_k = e(kT_s)$.

In conclusion, in continuous to discrete conversions, the discretization $H_d(z)$ of a continuous transfer function H(s) is:

$$H_d(z) = H(s') \qquad (A.6)$$

where

$$s' = \frac{2\,(z-1)}{T_s(z+1)} = \frac{2\,(1-z^{-1})}{T_s(1+z^{-1})} \qquad (A.7)$$

Instead, the discrete to continous conversion relies on the inverse correspondence

$$H(s) = H_d(z') \qquad (A.8)$$

where

$$z' = \frac{1 + \frac{sT_s}{2}}{1 - \frac{sT_s}{2}} \qquad (A.9)$$

Some of the digital components used in the CCS are shown below.

Integrator:

```
        INT(in,out) →
                        out[N]=out[N1]+_IQmpy(DTDIV2,(in[N]+in[N1]))
```

Where `_IQmpy` is the multiplication operator, and $DTDIV2 = T/2$, were T is the sample time of the inverter.

A generic low-pas filter code:

```
        FILTER_LPF(in,out,B0_LPF,A1_LPF)      →
                   out[N]=_IQmpy(B0_LPF,(in[N]+in[N1]))+_IQmpy(A1_LPF,out[N1])
```

Where `B0_LPF` and `A1_LPF` are the parameter calculated with the following MATLAB code:

```
        B0_LPF = ((pi*bw*Ts)/(1.0+pi*bw*Ts))
        A1_LPF = ((1.0-pi*bw*Ts)/(1.0+pi*bw*Ts))
```

Where $pi = \pi$, `bw` is the bandwidth of the low-pass filter and `Ts` is the sample time of the inverter. The two values obtained are then transformed in IQ(19) values to fit the CCS code.

The following definition are the CCS applications of the matrix (3.10) to pass from the stationary reference frame $\alpha\beta\gamma$ to the rotor speed rotating reference frame DQZ, and vice versa respectively.

```
ROTATE_POS(in,out,t)           →
            out.q[N]=_IQmpy(in.q[N],_IQcos(t))-
                        _IQmpy(in.d[N],_IQsin(t));
            out.d[N]=_IQmpy(in.q[N],_IQsin(t))+
                        _IQmpy(in.d[N],_IQcos(t));
ROTATE_NEG(in,out,t)     →
            out.q[N]=_IQmpy (in.q[N],_IQcos(t))+
                        _IQmpy(in.d[N],_IQsin(t));
            out.d[N]=-_IQmpy (in.q[N],_IQsin(t))+
                        _IQmpy(in.d[N],_IQcos(t));
```

Where `_IQcos(t)` and `_IQsin(t)` execute the cos and sin function on the variable `t`.

Bibliography

[1] Engeneeing Department (2009). *Notes for lectures of* Azionamenti Elettrici, Univeristy of Ferrara.

[2] Giorgio Pellizzaro (2011/2012). “Confronto delle prestazioni di motori SPM con diversi magneti permanenti”. *Master Thesis in Electrical Engineering*, DIE, University of Padova.

[3] Silverio Bolognani (a.a. 2004-05). *Notes for lectures* of Electric Drives, DII, Univeristy of Padova.

[4] Mario Gruda (2009/2010). “Progetto di un motore a magneti permanenti per trazione ferroviaria”. *Master Thesis in Electrical Engineering*, DIE, University of Padova.

[5] José Carlos Gamazo-Real, Ernesto Vázquez-Sánchez and Jaime Gómez-Gil (2010). “Position and Speed Control of Brushless DC Motors Using Sensorless Techniques and Application Trends”. *Communications and Telematic Engineering*, Department of Signal Theory, University of Valladolid

[6] Younggi Lee, Yong-Cheol Kwon, and Seung-Ki Sul (2015).“Comparison of Rotor Position Estimation Performance in Fundamental-Model-Based Sensorless Control of PMSM” *Energy Conversion Congress and Exposition* (ECCE), IEEE, 20-24 Sept. 2015, DOI: 10.1109/ECCE.2015.7310451. Department of Electrical and Computer Engineering, Seoul National University.

[7] Giorgio Valente (2013/2014). “Sensorless Control of an Interior Permanent Magnet Synchronous Motor in all the Speed Range, Including Position Control”. *Master Thesis in Electrical Engineering*, DIE, University of Padova.

[8] Fabio Baro (2011/2012). “Studio ed implementazione di tecniche di controllo sensorless di una macchina sincrona trifase brushless per applicazioni starter-alternator in veicoli ibridi”. *Master Thesis in Automation Engineering*, University of Padova.

[9] Roberto Pertella (2008/2009). *Notes for lectures of* Azionamenti Elettrici. Polytechnic Department of Elerctic, Management and Mechanical Engineering, University of Udine.

[10] Infineon Technology AG (2010). "Position Feedback for Motor Control Using Magnetic Sensors". *Application None Sense & Control*.

[11] David Rapos, Chris Mechefske; Markus Timusk Bharti. "Dynamic Sensor Calibration: A Comparative Study of a Hall Effect Sensor and an Incremental Encoder for Measuring Shaft Rotational Position", *Prognostics and Health Management* (ICPHM), IEEE, 20-22 June 2016, DOI: 10.1109/ICPHM.2016.7542858. Department of Mechanical Engineering Queen's University Kingston; School of Engineering Laurentian University Sudbury.

[12] Driss Yousfi, Abdellah Ait Ouahman (2010) . "VI-Model Based estimator versus Hall sensor based estimator in Brushless AC Sensorless Drives", *Control & Automation* (MED), IEEE, 23-25 June 2010, DOI: 10.1109/MED.2010.5547642. MSESYP Laboratory, Control Systems, Power Electronics and Electric Dives Group, Cadi Ayyad University, Ecole Nationale des Sciences Appliquées – Marrakech.

[13] Michael C. Harke; Giulio De Donato, Fabio Giulii Capponi; Tod R. Tesch, Robert D. Lorenz (2008). "Implementation Issues and Performance Evaluation of Sinusoidal, Surface-Mounted PM Machine Drives With Hall-Effect Position Sensors and a Vector-Tracking Observe", *IEEE Transactions on Industry Applications*, Volume: 44, Issue: 1, Jan.-feb. 2008, DOI: 10.1109/TIA.2007.912729. Applied Research Department, Hamilton Sundstrand, Rockford; Department of Electrical Engineering, University of Rome "La Sapienza".

[14] Sam-Young Kim; Chinchul Choi, Kyeongjin Lee, Wootaik Lee (2010). "An Improved Rotor Position Estimation With Vector-Tracking Observer in PMSM Drives With Low-Resolution Hall-Effect Sensors", *IEEE Transactions on Industrial Electronics* (Volume: 58, Issue: 9, Sept. 2011), DOI: 10.1109/TIE.2010.2098367. Industrial-Academic Cooperation, Changwon National University; Department of Control and Instrumentation Engineering, Changwon National University.

[15] K.A. Corzine, S.D. Sudhoff (1996). "A hybrid observer for high performance brushless DC motor drives", *IEEE Transactions on Energy Conversion* (Volume: 11, Issue: 2, Jun 1996), DOI: 10.1109/60.507184. Dept. of Electr. Eng., Missouri University.

[16] Saeed Golestan; Mohammad Monfared; Francisco D. Freijedo (2012). "Design-Oriented Study of Advanced Synchronous Reference Frame Phase-Locked Loops", *IEEE Transactions on Power Electronics* (Volume: 28, Issue: 2, Feb. 2013), DOI: 10.1109/TPEL.2012.2204276. Department of Electrical Engineering, Abadan Branch, Islamic Azad University; Department of Electrical Engineering, Faculty of Engineering, Ferdowsi University of Mashhad; Gamesa Innovation and Technology, Madrid.

[17] Xiaoqiang Guo, Weiyang Wu; Zhe Chen (2010). "Multiple-Complex Coefficient-Filter-Based Phase-Locked Loop and Synchronization Technique for Three-Phase Grid-

Interfaced Converters in Distributed Utility Networks”, *IEEE Transactions on Industrial Electronics* (Volume: 58, Issue: 4, April 2011), DOI: 10.1109/TIE.2010.2041738. Key Lab of Power Electronics for Energy Conservation and Motor Drive of Hebei Province, Department of Electrical Engineering, Yanshan University; Institute of Energy Technology, Aalborg University.